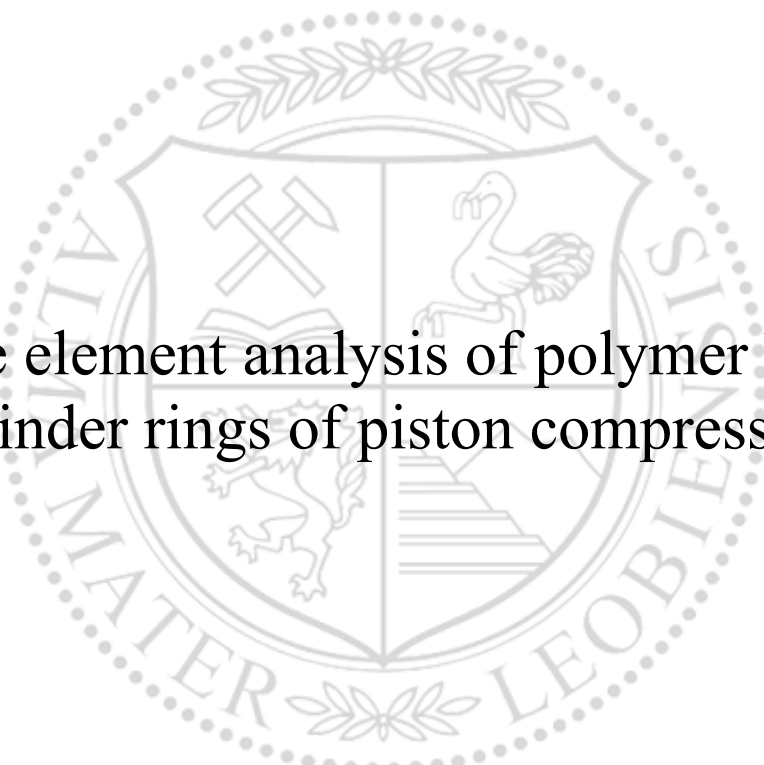




Chair of Mechanics

Master's Thesis

The background features a large, faint watermark of the University of Leoben seal. The seal is circular and contains a shield with four quadrants: top-left shows crossed hammers, top-right shows a stork, bottom-left shows a rampant lion, and bottom-right shows a staircase. The text 'UNIVERSITAS MONTANA LEOBENSIS' is written around the perimeter of the seal.

Finite element analysis of polymer based
cylinder rings of piston compressors

Marcel Ruetz, BSc

August 2022



MONTANUNIVERSITÄT LEOBEN

www.unileoben.ac.at

EIDESSTÄTLICHE ERKLÄRUNG

Ich erkläre an Eides statt, dass ich diese Arbeit selbständig verfasst, andere als die angegebenen Quellen und Hilfsmittel nicht benutzt, und mich auch sonst keiner unerlaubten Hilfsmittel bedient habe.

Ich erkläre, dass ich die Richtlinien des Senats der Montanuniversität Leoben zu "Gute wissenschaftliche Praxis" gelesen, verstanden und befolgt habe.

Weiters erkläre ich, dass die elektronische und gedruckte Version der eingereichten wissenschaftlichen Abschlussarbeit formal und inhaltlich identisch sind.

Datum 29.08.2022

Unterschrift Verfasser/in
Marcel Ruetz

Acknowledgement

I hereby want to thank my supervisors Univ.-Prof. Dipl.-Ing. Dr.mont. Thomas Antretter, Institute of Mechanics, University of Leoben as well as Dipl.-Ing. Dr.mont. Andreas Kaufmann of HOERBIGER Wien GmbH.

Furthermore my continued gratitude goes to Univ.-Prof. Dipl.-Ing. Dr.techn. Clara Schuecker from the chair of designing plastics and composite materials for the opportunity to write this thesis on the Institute of Mechanics.

Additionally I want to thank Dipl.-Ing. Dr.mont. Manuel Schemmel for his useful advice in working with ABAQUS CAE and Dipl.-Ing. Dr.-mont. Martin Pletz for offering the lecture "FE-Modelling using Python and ABAQUS", which also assisted me greatly in writing this thesis. Additionally I want to thank Assoz.-Prof. Dipl.-Ing. Ernst Gamsjäger for checking the abstract.

For checking and correcting grammar and spelling, I want to give great thanks to Miss Bianca Neumair.

Abstract

This master thesis is written in an act of cooperation between the Institute of Mechanics from the Montanuniversität Leoben and HOERBIGER Wien GmbH. The aim of this master thesis is to create a finite element model using a python script to determine the maximum possible size of cylinder ring protrusion for double acting piston compressors. A large cylinder ring protrusion leads to less potential wear between piston and the cylinder, but result in an increase of stresses, strains and deformations in the cylinder ring.

This thesis uses a linear elastic material model to check how well the results of an axisymmetric model match those of a three dimensional model. Since all results are in a comparable range, only the axisymmetric model is included in the following sections.

Using the material data of HOERBIGER Wien GmbH a viscoelastic material model, which accounts for time, temperature, load and load rate dependency is developed. For achieving higher accuracy, a viscoelastic material model serves as a basis. Linear viscoelastic parameters are functions of temperature and time. Non-linear viscoelasticity also takes the influence of the non-linear relationship between stresses and strains at higher stress values into account. This is not considered in linear viscoelastic- or elastic material models. However, since polymeric materials have a very small linear elastic range or linear viscoelastic range, a non-linear viscoelastic model appears to be the best choice for further investigations.

In the third part of this master thesis, a parameter study is carried out to determine the influence of temperature, time, pressure, load rate and geometry on the deformation behaviour of the cylinder rings. It also includes the creep behaviour of the material.

The final section deals with finding a suitable criterion to determine the maximum possible cylinder ring protrusion. The creep strains that occur are small and therefore not decisive for failure. In the case of the cylinder rings, a classic fatigue strength problem is to be dealt with. The permissible cylinder ring protrusion is assessed in an analogy to the FKM guideline with the help of the degree of utilisation. The stresses are evaluated at the critical point. The maximum mean stress and stress amplitude that occur during a load cycle are taken from the FE results. The cylinder ring protrusion is varied until the maximum degree of utilisation is reached. This is repeated for other load levels. Since no fatigue strength data is available for the material used, the fatigue strength data and the fatigue strength curves are approximated using estimation formulas. This also includes the further evaluations. The results show that the permissible cylinder ring protrusion can be significantly increased depending on the pressure difference without reaching the maximum allowable degree of utilisation.

Zusammenfassung

Die vorliegende Masterarbeit wurde in Kooperation zwischen dem Institut für Mechanik der Montanuniversität Leoben und der HOERBIGER Wien GmbH geschrieben. Ziel dieser Arbeit ist der Aufbau eines geeigneten Finite Elemente Modells zur Bestimmung des maximal möglichen Zylinderringüberstands für doppelwirkende Kolbenkompressoren. Zunehmende Zylinderringüberstände führen zu einer Abnahme des Verschleisses zwischen Zylinderwand und Kolben, gleichzeitig erhöhen sich die auftretenden Spannungen, Verzerrungen und Deformationen im Zylinderring.

Zur Erstellung des FE-Modelle werden automatisierte Python-Scripts herangezogen. Zur Validierung der Simulationsresultate eines axialsymmetrischen Modells wird ein Vergleich mit verschiedenen 3D-Geometrien durchgeführt. Dazu wird zunächst ein linear-elastisches Materialmodell verwendet. Da die Ergebnisse des axialsymmetrischen Modells eine gute Übereinstimmung mit den Ergebnisse der 3D-Modelle zeigt, wird in weiterer Folge nur noch das axialsymmetrische Modell verwendet.

Aus den Materialdaten der HOERBIGER Wien GmbH. werden die Parameter eines nicht-linear viskoelastischen Materialmodells bestimmt. Dieses Modell berücksichtigt neben der Abhängigkeit von Zeit und Temperatur auch die Abhängigkeit von der Deformation bei höheren Belastungen. Kunststoffe weisen nur einen kleinen linear-elastischen und linear-viskoelastischen Deformationsbereich auf, deshalb erweist sich ein nichtlinear viskoelastische Materialmodell als beste Beschreibung.

Schließlich wird der Einfluss der unterschiedlichen Parameter (Zeit, Druck, Temperatur, Zylinderringüberstand sowie Lastrate) auf das Deformationsverhalten des Zylinderrings untersucht. Auch der Einfluss der Abmessungen der Zylinderringe ist von Interesse. Die Ergebnisse zeigen, dass sich die Parameter unterschiedlich stark auf das Kriechverhalten des Materials auswirken.

Mittels eines geeigneten Kriteriums wird der maximal mögliche Zylinderringüberstand bestimmt. Da die auftretenden Kriechdehnungen sehr klein sind, sind diese nicht versagensentscheidend. Es liegt ein klassisches Ermüdungsfestigkeitsproblem vor. Die maximal möglichen Zylinderringüberstände werden in Analogie zur FKM-Richtlinie bestimmt. Der Zylinderringüberstand wird dabei in einer Simulationsstudie bei unterschiedlichen Druckniveaus solange erhöht, bis der maximale Auslastungsgrad erreicht ist. Da für das verwendete Material keine Ermüdungsfestigkeitsdaten verfügbar sind, werden diese Daten mithilfe von Abschätzformeln bestimmt. Die Ergebnisse zeigen, dass der zulässige Zylinderringüberstand in Abhängigkeit von der Druckdifferenz zum Teil deutlich vergrößert werden kann, bevor der maximale Auslastungsgrad erreicht wird.

Personal motivation

As a student of the two disciplines, polymer science and mechanical engineering, I am especially interested in the overlaps of these two disciplines. So, I enthusiastically greeted the opportunity to conduct research in the field of "Finite element analysis of polymer based cylinder rings of piston compressors". While researching, I found myself captivated by the interdisciplinary nature of this topic. The range of this project included topics such as classical mechanical engineering, thermodynamics, finite element analysis, operational strength but also topics like polymer science, physics of solid polymers or material models of polymers.

Material parameters and material data

At the request of the company partner, all material data and calibrated material parameters are removed in the official version of this Master thesis.

Auf Wunsch des Firmenpartners wurden alle Materialdaten und kalibrierten Materialparameter aus der offiziellen Version dieser Masterarbeit entfernt.

Contents

1	Introduction	1
1.1	Nomenclature	2
1.1.1	Continuum mechanics of small strains	2
1.1.2	Basic material models	2
1.1.3	Constitutive equation for viscoelasticity	2
1.1.4	Hyperelasticity	3
1.1.5	Heat conduction	3
1.1.6	Parameter study	3
1.1.7	Criterion for maximum clearance	3
1.1.8	Discussion	4
1.2	Compressors	5
1.2.1	Piston compressors	5
1.2.2	Cylinder rings	6
1.3	State of the art	6
2	Theoretical Fundamentals	7
2.1	Continuum mechanics of small deformations	8
2.1.1	Stress state	8
2.1.2	Deformation state	10
2.2	Introduction to basic material models	13
2.2.1	Linear elastic deformation behaviour	13
2.2.2	Viscous deformation behaviour	14
2.2.3	Ideal plastic deformation behaviour	15
2.2.4	Viscoelastic deformation behaviour	16
2.3	Viscoelasticity	17
2.3.1	Relaxation and creep test	17
2.3.2	Constitutive equation for relaxation behaviour	18
2.3.3	Generalised constitutive equation for viscoelasticity	19
2.3.4	Linear and non-linear viscoelasticity	20
2.3.5	Prony series	21
2.3.6	Periodic loads	22
2.3.7	Heat conduction in solids	24
2.3.8	Creep behaviour of polymers	26
2.3.9	Calibration of the material data	27
2.3.10	Calibration using MCalibration	28
2.3.11	Time-temperature superposition	28
2.4	Viscoplasticity	30

2.4.1	Parallel Rheological Framework (PRF-Model)	30
2.5	Hyperelasticity	31
2.5.1	Yeoh model	31
3	Modelling	32
3.1	Mechanical model of the problem	33
3.1.1	Submodel	35
3.2	Mathematical model for the load signal	36
3.2.1	Load signal crank end (CE)	37
3.2.2	Load signal head end (HE)	38
3.3	Thermal model	39
4	Results	41
4.1	Comparison of axisymmetric and 3D model	42
4.1.1	Stress field in the cylinder ring	43
4.1.2	Stress field in the axisymmetric model	44
4.1.3	Stress field in the uncut 3D ring	45
4.1.4	Stress field in the cut 3D ring	46
4.1.5	Results of the comparison	47
4.2	Convergence study	48
4.2.1	Principle of Saint Venant	49
4.3	Calibration of the material model	50
4.3.1	Linear or nonlinear viscoelasticity	51
4.3.2	Stability of the hyperelastic model	51
4.3.3	Evaluation of the material model	52
4.4	Parameter study	53
4.4.1	Creep strain magnitude	53
4.4.2	Influence of the ring protrusion on the creep behaviour	55
4.4.3	Influence of the temperature on the creep behaviour	56
4.4.4	Influence of the load rate on the creep behaviour	57
4.4.5	Influence of the heating process through hysteresis losses	58
4.4.6	Influence of the load level on the creep behaviour	59
4.4.7	Influence of the dimensions of the cylinder rings on creep	60
4.4.8	Influence of the material model	62
4.4.9	Fluctuation of the creep curves	63
4.4.10	Conclusion of the parameter study	65
4.5	Criterion for the maximum possible ring protrusion	66
4.5.1	Dimensioning criterion	66
4.5.2	High cycle fatigue	67
4.5.3	Synthetic material fatigue curves	68
4.5.4	Synthetic component fatigue curve	70
4.5.5	Degree of utilisation	74
4.6	Simulation results	75
4.6.1	Utilisation curve	79
4.6.2	Consideration of plasticity for the highest load level	81
4.6.3	Fracture mechanics	82
4.7	Discussion	84

4.7.1	Cylinder ring protrusion	84
4.7.2	Plausibility of the interpolation function	84
4.7.3	Single acting compressors	84
4.7.4	Consideration of the temperature distribution	85
4.7.5	Fracture mechanics approach for synthetic fatigue curves	86
4.7.6	Mises criterion for polymers	87
5	Conclusion and Outlook	88
5.1	Conclusion	89
5.2	Outlook	91

Chapter 1

Introduction

1.1 Nomenclature

In these section, all symbols which can be found in further chapters and sections of this thesis, are listed in the order they appear.

1.1.1 Continuum mechanics of small strains

σ_r ...radial stress [MPa]
 σ_φ ...tangential stress [MPa]
 σ_z ...axial stress [MPa]
 \underline{k} ...volume force [N/m³]
 \underline{a} ...acceleration [m/s²]
 \underline{r}_S ...location vector [m]
 \underline{I} ...unity tensor [-]
 u_r ...radial displacement [m]
 u_φ ...tangential displacement [m]
 u_z ...axial displacement [m]
 ε_r ...radial strain [-]
 ε_φ ...tangential strain [-]
 ε_z ...axial strain [-]

1.1.2 Basic material models

σ ... normal stress [MPa]
 ε ...strain [-]
 E ...Young's modulus [MPa]
 η ...dynamic viscosity [Pa·s]
 σ_F ...Yield stress [MPa]

1.1.3 Constitutive equation for viscoelasticity

σ_{ij} ...stress tensor [MPa]
 G ...shear modulus [MPa]
 $\dot{\varepsilon}_{ij}^{(dev)}$...deviatoric deformation rate tensor [1/s]
 K ...volumetric modulus [MPa]
 $\dot{\varepsilon}_{ij}^{(vol)}$...volumetric deformation rate tensor [1/s]
 τ_i ...relaxation time constant [s]
 G_0 ...spontaneous shear modulus [MPa]
 E^* ...dynamic (complex) modulus [MPa]
 E' ...storage modulus [MPa]
 E'' ...loss modulus [MPa]
 δ ...phase angle between $\varepsilon(t)$ and $\sigma(t)$ [-]
 a_T ...temperature shifting function [-]
 T ...temperature [K]
 T_{ref} ...reference temperature [K]
 C_1 ...time shifting parameter 1 [-]
 C_2 ...time shifting parameter 2 [-]

1.1.4 Hyperelasticity

ψ ...Helmholtz free Energy [J]
 I_1^* ...distortion part of the first invariant [-]
 I_3 ...third invariant of Green's strain tensor [-]
 C_{10}, C_{20}, C_{30} ...Material parameter for Yeoh model
 b_{ij} ...left hand Green strain tensor [-]
 F ...Gradient of distortion [-]

1.1.5 Heat conduction

dU ...differential internal energy [J]
 dQ ...differential thermal energy [J]
 dW ...differential mechanical energy [J]
 m ...mass [kg]
 c_v ...specific heat capacity [J/(kg K)]
 V ...volume [m³]
 \dot{q} ...heat flux [W/m²]
 \underline{n} ...normal vector [-]
 ∇ ...Nabla operator [1/m]
 λ ...heat conduction coefficient [W/(m K)]

1.1.6 Parameter study

$\varepsilon_{mag}^{(creep)}$...creep strain magnitude [-]
 $\varepsilon_{ij}^{(creep)}$...creep strain tensor [-]

1.1.7 Criterion for maximum clearance

k ...slope of the fatigue curve [1/MPa]
 N_A ...break point of the fatigue curve [-]
 N_i ... load changes [-]
 σ_A ...fatigue strength [MPa]
 σ_a ...stress amplitude [MPa]
 σ_w ...alternating strength [MPa]
 R_{p1} ... 1% yield point [MPa]
 M ...stress sensitivity [-]
 K_M ...correction factor for medium stress sensitivity [-]
 R ...stress ratio [-]
 σ_{min} ...minimum stress amplitude [MPa]
 σ_{max} ...maximum stress amplitude [MPa]
 χ ...related stress gradient [1/m]
 $\frac{d\sigma}{dx}$...stress gradient [MPa/m]
 σ_{dw} ...alternating compression strength [MPa]
 σ_{bw} ...alternating bending strength [MPa]
 σ_{zw} ...alternating tension strength [MPa]
 b ...dimension of a specimen for fatigue testing [m]

K_D ...correction exponent [-]
 $a^{(stat)}$...static degree of utilisation [-]
 σ_{lim} ...permissible stress [MPa]
 $a^{(dyn)}$...cyclic degree of utilisation [-]
 m_Y ...yield point ratio [-]
 σ_V ...comparison stress [MPa]
 σ_1 ...maximum principal stress [MPa]
 σ_2 ...middle principal stress [MPa]
 σ_3 ...minimum principal stress [MPa]
 ΔK ...oscillation width of the cyclic stress intensity [MPa \sqrt{m}]
 $\Delta\sigma$...oscillation width of the cyclic nominal stress [MPa]
 a ...crack length [mm]
 ΔK_{th} ...threshold value of stress intensity [MPa \sqrt{m}]
 Y ...geometry factor for crack length [-]

1.1.8 Discussion

$R_{p,tensile}$...tensile yielding point [MPa]
 $R_{p,compression}$...compression yielding point [MPa]

1.2 Compressors

There is a wide range of compressor designs from piston compressors to rotary compressors in a variety of designs including special designs such as the roots blower. Their main task is to compress a gaseous medium. Compressors operate according to the laws of thermodynamics. Rotary compressors are designed for large volume flows but small pressure differences, while piston compressors are designed for large pressure differences but smaller volume flows.

1.2.1 Piston compressors

Piston compressors are used in a wide range of applications. Smaller designs of piston compressors are used in the private sector whereas for industrial applications larger designs are commonly encountered e.g.. Compressors ensure the supply of compressed air. Figure 1.1 shows the basic structure of a piston compressor. Its most important components are the piston, the piston rod, the cylinder rings and the rider rings. The working space is defined by the cylinder and the piston.

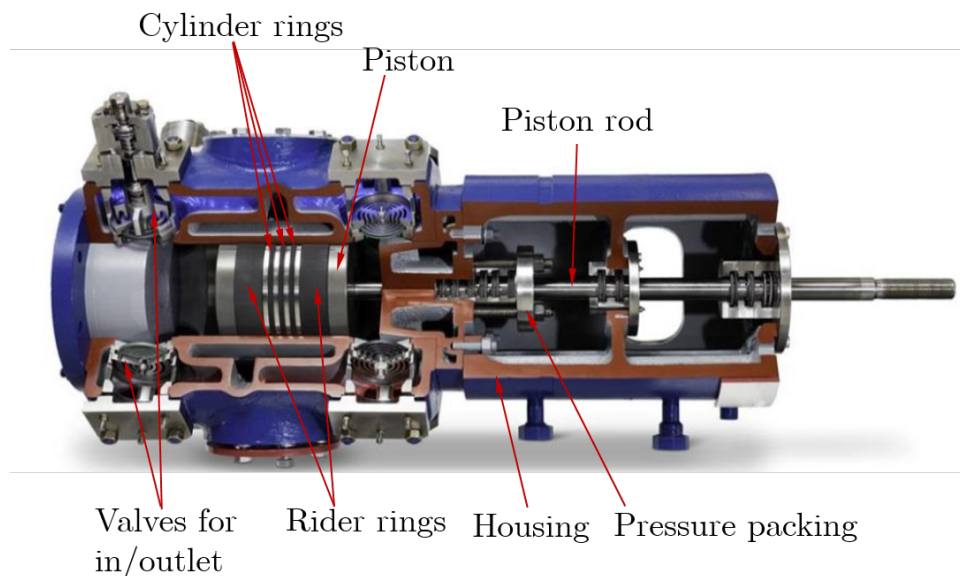


Figure 1.1: Piston compressor [10]

When the piston moves towards crank end dead centre, a negative pressure is generated inside the working chamber. When the inlet valve is open, this causes the working medium to be sucked in. Then the inlet valve closes. If the piston now moves towards head end dead centre, the working fluid is compressed. The real circular process is idealised as a Joule process. The Joule process consists of two isentropic and two isobaric changes of state. In the isentropic change of state, the entropy remains constant, whereas in the isobaric change of state, the pressure remains constant.

1.2.2 Cylinder rings

This master thesis focuses on the cylinder rings. They have the task of sealing the compression chamber. A high sealing effect is essential for the efficient operation of the compressor. In contrast to the rider rings the cylinder rings do not carry the load of the piston.

The cylinder rings are made of polymer based materials, most often highly filled compounds comprising PTFE (polytetrafluoroethylene). This high-temperature resistant, semi-crystalline thermoplastic material also has good tribological properties (sliding properties, wear properties). For this reason, PTFE is often used as a sliding bearing material because bearings with graphite filling have self-lubricating properties.

However, the cylinder rings are stressed by the cyclic pressure changes that occur during operation. In addition, various heat flows act on the cylinder ring.

1.3 State of the art

Although cylinder rings have been used for sealing purposes for a long time, the design criteria are rather rigid. It was not possible to do these calculations, thus simpler approaches had to be taken. In earlier times, practical tests were used to determine the dimensions of the cylinder rings or the cylinder ring protrusion. Nowadays the use of modern numerical solution methods such as the finite element method allows optimising the design of the cylinder rings. Numerical methods further allow determining the influence of the geometry as well as the material under realistic conditions, which are hardly possible or impossible to determine experimentally.

The central research question of this master thesis is to determine the maximum possible cylinder ring protrusion for double-acting piston compressors. Furthermore, the influence of the geometry of the cylinder ring and the material used is to be investigated in more detail.

In this Master thesis, the two terms clearance and protrusion are used for the clearance between the cylinder ring and the piston.

Chapter 2

Theoretical Fundamentals

2.1 Continuum mechanics of small deformations

2.1.1 Stress state

Due to the geometry of the cylinder ring the stress state is described by using cylindrical coordinates. The stress state in a three-dimensional continuum is described by a symmetric 3x3 stress tensor. In the Cauchy formulation of the stress tensor, the stresses are applied to the undeformed body (reference configuration).

$$\underline{\underline{\sigma}} = \begin{pmatrix} \sigma_r & \sigma_{r\varphi} & \sigma_{rz} \\ \sigma_{\varphi r} & \sigma_\varphi & \sigma_{\varphi z} \\ \sigma_{zr} & \sigma_{z\varphi} & \sigma_z \end{pmatrix} \quad (2.1)$$

Figure 2.1 shows the free body diagram of an infinite mass element.

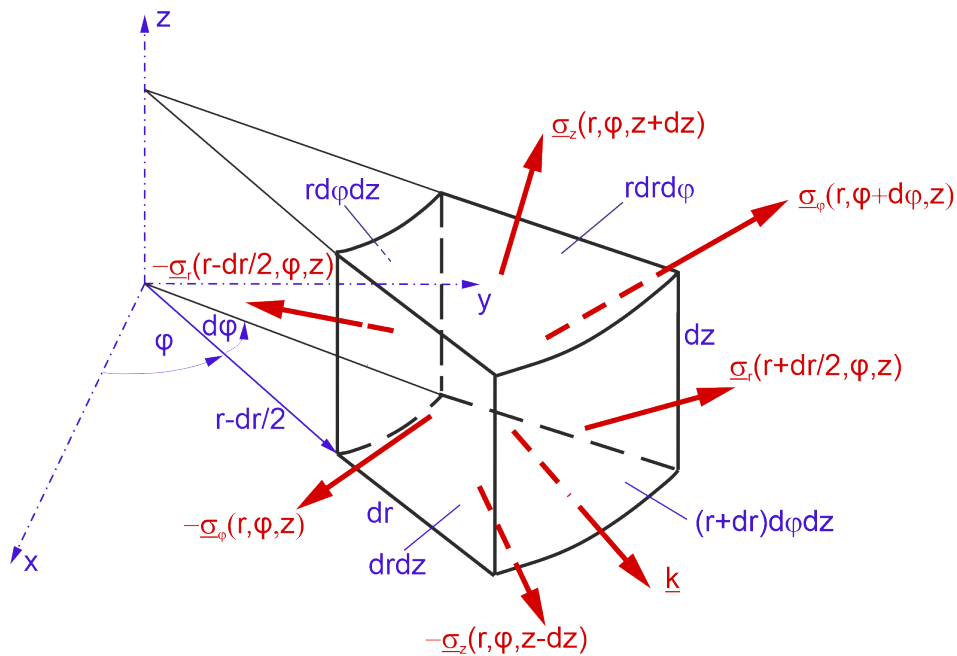


Figure 2.1: Free-body-diagram of an infinite mass element

The stress state can be expanded by the Taylor series.

$$\sigma_r(r + dr/2, \varphi, z) = \sigma_r + \frac{\partial \sigma_r}{\partial r} \frac{dr}{2} + \dots \quad (2.2)$$

$$\sigma_r(r - dr/2, \varphi, z) = \sigma_r - \frac{\partial \sigma_r}{\partial r} \frac{dr}{2} + \dots \quad (2.3)$$

$$\sigma_\varphi(r, \varphi + d\varphi, z) = \sigma_\varphi + \frac{\partial \sigma_\varphi}{\partial \varphi} d\varphi + \dots \quad (2.4)$$

$$\sigma_z(r, \varphi, z + dz) = \sigma_z + \frac{\partial \sigma_z}{\partial z} dz + \dots \quad (2.5)$$

The resulting force vector for the infinitesimal mass element is

$$\left(\underline{\sigma}_r + \frac{\partial \underline{\sigma}_r}{\partial r} \frac{dr}{2}\right) \left(r + \frac{dr}{2}\right) d\varphi dz - \underline{\sigma}_r \left(r - \frac{dr}{2}\right) d\varphi dz + \left(\underline{\sigma}_z + \frac{\partial \underline{\sigma}_z}{\partial z} dz\right) r dr d\varphi - \underline{\sigma}_z r dr d\varphi + \left(\underline{\sigma}_\varphi + \frac{\partial \underline{\sigma}_\varphi}{\partial \varphi} d\varphi\right) dr dz - \underline{\sigma}_\varphi dr dz + \underline{k} r dr d\varphi dz = \underline{F} \quad (2.6)$$

$$\frac{\partial \underline{\sigma}_r}{\partial r} r dr d\varphi dz + \underline{\sigma}_r dr d\varphi dz + \frac{\partial \underline{\sigma}_\varphi}{\partial \varphi} dr dz + \frac{\partial \underline{\sigma}_z}{\partial z} r dr d\varphi dz + \underline{k} r dr d\varphi dz = \underline{f} r dr d\varphi dz \quad (2.7)$$

where \underline{k} is the volume force density. Further dividing this term by the element volume delivers the force density \underline{f} .

$$\underline{f} = \frac{\partial \underline{\sigma}_r}{\partial r} + \frac{1}{r} \underline{\sigma}_r + \frac{1}{r} \frac{\partial \underline{\sigma}_\varphi}{\partial \varphi} + \frac{\partial \underline{\sigma}_z}{\partial z} + \underline{k} \quad (2.8)$$

Newton's second law states that the sum of all forces \underline{F} which apply on the body are equal to the product of mass m and the acceleration of the mass center \underline{a} .

$$\underline{F} = m \underline{a} \quad (2.9)$$

Dividing by the volume and further inserting the force density delivers the basic law of motion for the infinitesimal mass element in cylindrical coordinates,

$$\frac{\partial \underline{\sigma}_r}{\partial r} + \frac{1}{r} \underline{\sigma}_r + \frac{1}{r} \frac{\partial \underline{\sigma}_\varphi}{\partial \varphi} + \frac{\partial \underline{\sigma}_z}{\partial z} + \underline{k} = \rho \underline{a} \quad (2.10)$$

where ρ is the mass density and \underline{a} is the acceleration. For the static case this equation reduces to the equilibrium condition of an infinitesimal mass element.

$$\frac{\partial \underline{\sigma}_r}{\partial r} + \frac{1}{r} \underline{\sigma}_r + \frac{1}{r} \frac{\partial \underline{\sigma}_\varphi}{\partial \varphi} + \frac{\partial \underline{\sigma}_z}{\partial z} + \underline{k} = \underline{0} \quad (2.11)$$

This system of coupled partial differential equations describes the resulting stress state in the continuum due to volume forces and surface tractions. Because of the symmetry of the stress tensor this system has six independent and unknown stress components. But there are only three equations. Thus this system is three times statically undetermined. To solve this system further equations are required. Kinematics and constitutive equations deliver additional equations.

The symmetry of the Cauchy stress tensor follows from the moment equilibrium.

2.1.2 Deformation state

For small deformations the deformation state is formulated in the linearised form. A kinematic observation of the continuum and the principles of Taylor series expansion describe the deformation state.

Figure 2.2 shows the kinematics of an infinitesimal element in cylindrical coordinates.

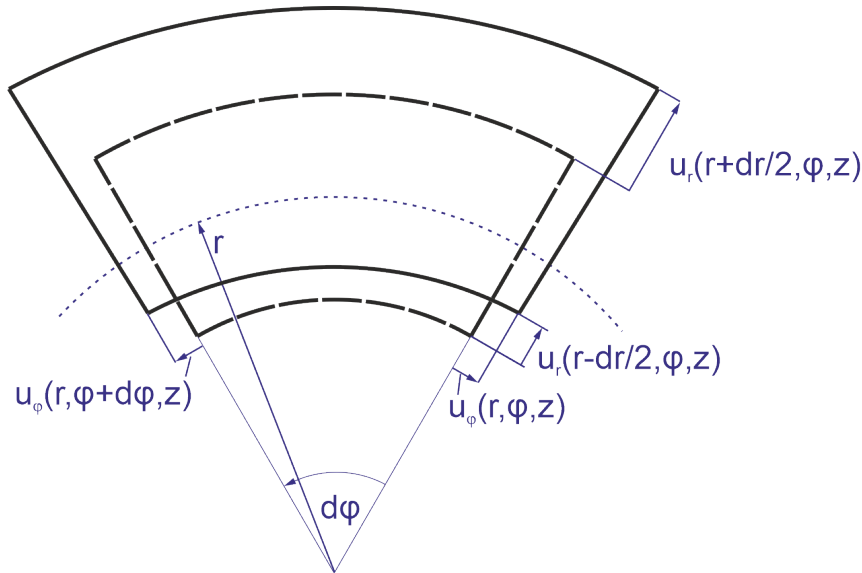


Figure 2.2: Kinematics of a mass element in cylindrical coordinates

where u_r is the displacement in radial direction and u_φ is the displacement in tangential direction.

$$u_r\left(r + \frac{dr}{2}, \varphi, z\right) = u_r(r) + \frac{\partial u_r}{\partial r} \frac{dr}{2} + \dots \quad (2.12)$$

$$u_r\left(r - \frac{dr}{2}, \varphi, z\right) = u_r(r) - \frac{\partial u_r}{\partial r} \frac{dr}{2} + \dots \quad (2.13)$$

$$u_\varphi(r, \varphi + d\varphi, z) = u_\varphi(\varphi) + \frac{\partial u_\varphi}{\partial \varphi} d\varphi + \dots \quad (2.14)$$

$$u_z(r, \varphi, z + dz) = u_z(z) + \frac{\partial u_z}{\partial z} dz + \dots \quad (2.15)$$

Strain is defined as the change of the displacement based on the starting dimension.

$$\varepsilon_r = \frac{u_r\left(r + \frac{dr}{2}\right) - u_r\left(r - \frac{dr}{2}\right)}{dr} \quad (2.16)$$

$$\varepsilon_r = \frac{\partial u_r}{\partial r} \quad (2.17)$$

In the same way, a correlation is found for the displacement and the strain in φ -direction.

$$\varepsilon_\varphi = \frac{u_\varphi(\varphi + d\varphi) - u_\varphi(\varphi) + u_r d\varphi}{r d\varphi} \quad (2.18)$$

The additional term $u_r d\varphi$ follows from the expansion in circumferential direction.

$$\varepsilon_\varphi = \frac{1}{r} \frac{\partial u_\varphi}{\partial \varphi} + \frac{u_r}{r} \quad (2.19)$$

For the case of axis-symmetry, this is simplified to

$$\varepsilon_\varphi = \frac{u_r}{r} \quad (2.20)$$

By analogy, the strain in the axial direction can also be calculated. The relationship for this follows from Figure 2.3.

$$\varepsilon_z = \frac{u_z(z+dz) - u_z(z)}{dz} \quad (2.21)$$

By inserting the corresponding Taylor series expansion, terminated after the linear term, follows.

$$\varepsilon_z = \frac{\partial u_z}{\partial z} \quad (2.22)$$

To determine the strain-displacement relationships for the shear strains, a correspondingly deformed infinitesimal element comes into consideration.

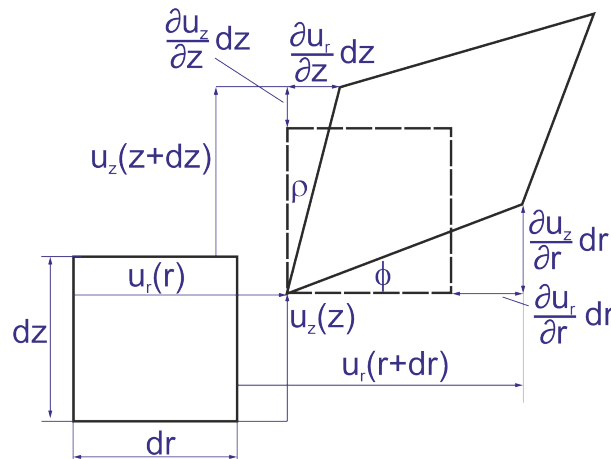


Figure 2.3: Kinematics in cylindrical coordinates for shear deformation

According to figure 2.3, the shear angle is equal to the sum of the two angular changes of the deformed element.

$$\gamma_{rz} = \phi + \rho \quad (2.23)$$

The two angles follow from the definition of the corresponding angle functions. Under the condition of small displacement angles, these relationships can be linearised.

$$\tan(\phi) \approx \phi = \frac{\frac{\partial u_z}{\partial r} dr}{dr + \frac{\partial u_r}{\partial r} dr} = \frac{\frac{\partial u_z}{\partial r}}{1 + \frac{\partial u_r}{\partial r}} \quad (2.24)$$

$$\tan(\rho) \approx \rho = \frac{\frac{\partial u_r}{\partial z} dz}{dz + \frac{\partial u_z}{\partial z} dz} = \frac{\frac{\partial u_r}{\partial z}}{1 + \frac{\partial u_z}{\partial z}} \quad (2.25)$$

The shear strains follows by inserting these angles into the definition equation for the shear angle.

$$\gamma_{rz} = \frac{\frac{\partial u_r}{\partial z}}{1 + \frac{\partial u_z}{\partial z}} + \frac{\frac{\partial u_z}{\partial r}}{1 + \frac{\partial u_r}{\partial r}} \quad (2.26)$$

Due to the fact that the linearised stain-displacement relationship is only valid for small distortions, the following simpler relationship holds true:

$$\gamma_{rz} = \frac{\partial u_r}{\partial z} + \frac{\partial u_z}{\partial r} \quad (2.27)$$

The other two shear angles follow by analogy.

$$\gamma_{r\varphi} = \frac{1}{r} \frac{\partial u_r}{\partial \varphi} + \frac{\partial u_\varphi}{\partial r} \quad (2.28)$$

$$\gamma_{z\varphi} = \frac{1}{r} \frac{\partial u_z}{\partial \varphi} + \frac{\partial u_\varphi}{\partial z} \quad (2.29)$$

The pre-factor $1/r$ follows from the derivation of the corresponding unit vectors, which move with the coordinate system in cylindrical coordinates.

2.2 Introduction to basic material models

The deformation behaviour of polymer materials consists of three different components: a spontaneous elastic part, in the range of very small loads, secondly a time dependent viscoelastic part in the range of higher loads and a plastic part. In general, so-called rheological models are used to symbolize the one dimensional material behaviour. These one-dimensional surrogate models can be generalised for general stress and distortion states.

2.2.1 Linear elastic deformation behaviour

The elastic deformation is time independent. This means that materials delay spontaneously to an applied load shown in Figure 2.4. The linear elastic deformation behaviour is represented by the Hookean element. This is graphically symbolised with the help of a spring. The spring represents the Young's modulus [3] (p289-290). Hooke's law describes the connection between the stress σ and the strain state ε ,

$$\sigma = E\varepsilon \quad (2.30)$$

where E is the Young's modulus.

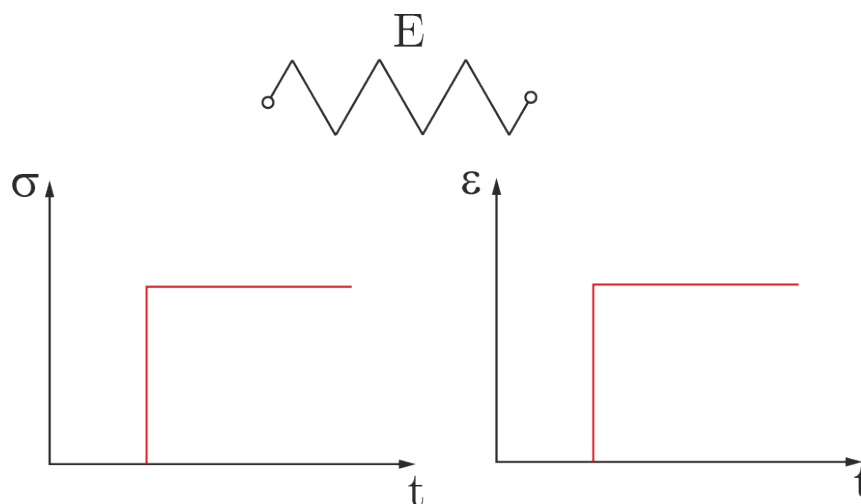


Figure 2.4: Linear elastic material behaviour

The linear elastic behaviour of polymeric materials results from the change of the atomic bond distances and the change of the valence angles. The linear elastic material behaviour is only relevant for polymers in the range of very small stresses and strains. The subsequent linear and non-linear viscoelastic range is reversible but time-dependent, or in the case of the non-linear viscoelastic range dependent on the load level.

2.2.2 Viscous deformation behaviour

The viscous deformation is time dependent. The materials reaction to an applied load occurs not spontaneously shown in Figure 2.5. This means that there is a time displacement between the stress and the resulting deformation. The viscous deformation behaviour, modelled by a so called Newton element, is described by the dynamic viscosity η . The time dependent behaviour of Newton elements is often sketched by a damper and Newton's law describes the connection between the stress and the strain rate $\frac{d\varepsilon}{dt}$ [3] (p290),

$$\sigma = \eta \frac{d\varepsilon}{dt} \quad (2.31)$$

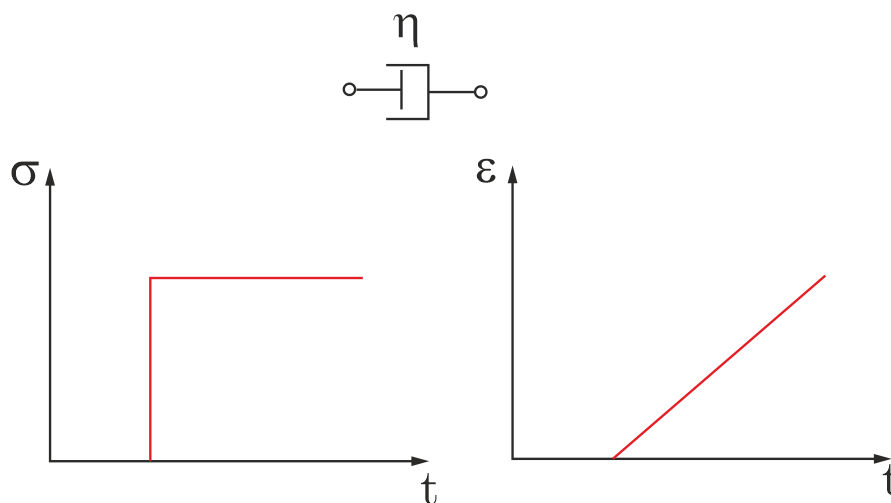


Figure 2.5: Viscous material behaviour

The viscous deformation behaviour is particularly suitable for describing the mechanical behaviour of fluids. More complex fluids, such as Bingham fluids, for example, are modelled by connecting a Hooke and a Newton element in series. In general, η is also a function of the strain rate. If the viscosity decreases with increasing strain rate, a structural viscous behaviour is present. If, on the other hand, the viscosity increases, dilatant behaviour will be observed.

2.2.3 Ideal plastic deformation behaviour

The ideal plastic deformation behaviour is also time independent as shown in Figure 2.6. When the applied stress reaches the yield stress the stress stops increasing further. A so called Saint-Venant element models the ideal plastic material behaviour. Saint-Venant elements are often sketched as a friction contact between a solid and a layer [3]. More realistic plasticity models include hardening effects, such as isotropic or kinematic hardening. Details are found in various literature about hardening effects.

$$\varepsilon = \begin{cases} 0, & \text{if } \sigma < \sigma_F \\ \infty, & \text{if } \sigma = \sigma_F \end{cases} \quad (2.32)$$

Where σ_F is the yield stress.

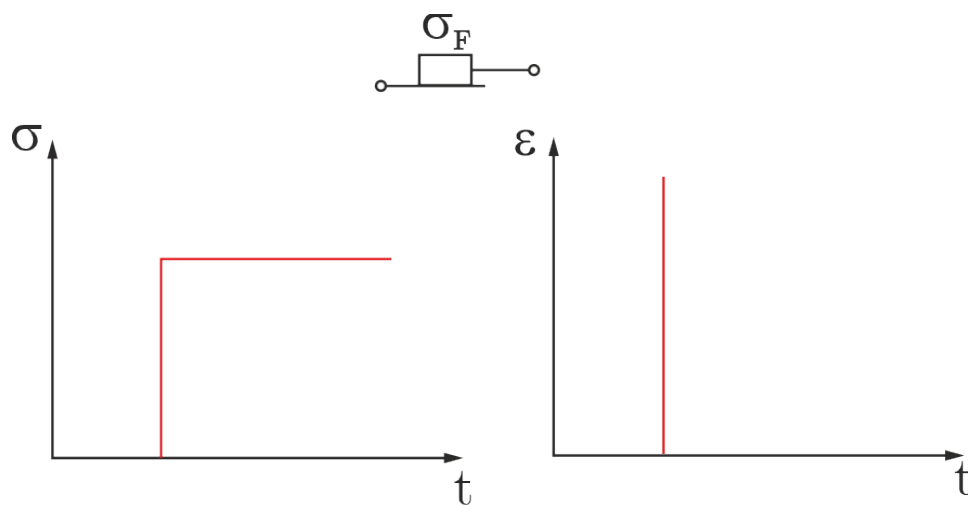


Figure 2.6: Ideal plastic material behaviour

Numerous models found in the literature describe the plastic deformation behaviour of solid materials. An extensive discussion exceeds the scope of this thesis. The plastic deformation behaviour is treated in detail in [1],[3], [4] for example.

2.2.4 Viscoelastic deformation behaviour

Other more complex material models, such as viscoelasticity, are designed from these three basic building blocks described in 2.2.1-2.2.3 by serial and parallel combinations. Polymers show a time dependent deformation behaviour shown in Figure 2.7. Thus the material behaviour can be modelled by a parallel arrangement of linear elasticity and viscous behaviour. The hookean element symbolizes the spontaneous response of the material and the Newton element describes the time dependence response. The deformation for both parts needs to be equal,

$$\varepsilon = \varepsilon_H = \varepsilon_N \quad (2.33)$$

where ε_H is the strain on the Hooke element and ε_N is the strain on the Newton element. The applied stress requires equivalence of the sum of the stresses throughout the model

$$\sigma = \sigma_H + \sigma_N \quad (2.34)$$

where σ_H is the stress in the Hooke element and σ_N is the stress in the Newton element. Inserting the equation of the basic models delivers the following inhomogeneous differential equation, which describes the time dependent material answer to an applied load signal.

$$\eta \frac{d\varepsilon}{dt} + E\varepsilon = \sigma \quad (2.35)$$

The solution of this differential equation comprises the description of the time dependent deformation behaviour of the viscoelastic material by using two variables. It includes the in general temperature and load dependent variables E and η .

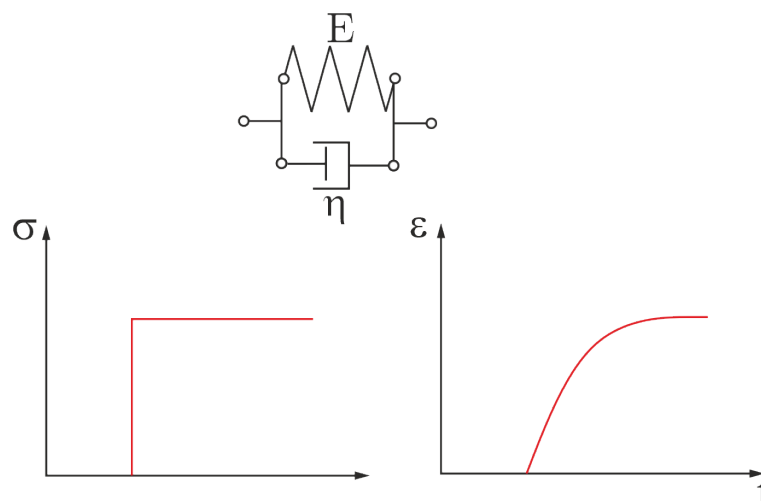


Figure 2.7: Ideal viscoelastic material behaviour

The parallel setup does not properly capture the real viscoelastic material behaviour. Other models, like the multi network Maxwell model provide a better view on the viscoelastic material behaviour. Detailed information about this model can be found in additional literature such as [4].

2.3 Viscoelasticity

Viscoelasticity describes the time and temperature dependent mechanical behaviour of solid continua. It is typically used for thermoplastic polymers. Overall, viscoelasticity includes elastic and viscous deformation parts. The main reasons for the time dependency of the material behaviour is that the material wants to achieve a thermodynamically stable state. Through molecular replacement and reordering processes, so-called relaxation processes, the material tries to achieve this increased stability. For material characterisation and defining the parameters to describe the time dependent behaviour, relaxation and creep tests are essential.

2.3.1 Relaxation and creep test

The principle of relaxation tests is simple (figure 2.8). One loads a specimen with a constant strain ε_0 and a measuring system to measure the change of the tensile stress $\sigma(t)$ over time. The tensile stress decreases during time through the relaxation processes inside the material.

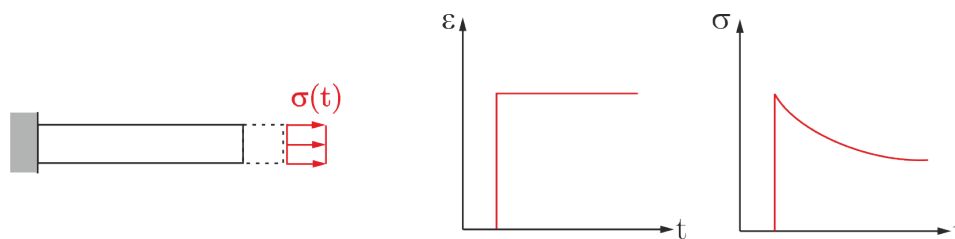


Figure 2.8: Principle of the relaxation test

Hooke's law for a one dimension axial stress state reads

$$\sigma(t) = E(t)\varepsilon_0 \quad (2.36)$$

A reduction of the stress $\sigma(t)$ at constant strain ε_0 is solely possible if Young's modulus $E(t)$ decreases with time. Thus, the relaxation modulus is defined as [4] (p310-311):

$$E(t) = \frac{\sigma(t)}{\varepsilon_0} \quad (2.37)$$

The principle of a creep test works similar to the relaxation test, where only one constant stress is applied. The major disadvantage of the relaxation test is that the testing device is more complex than the one for the creep tests. Due to the stress drop inside the specimen resulting from the relaxation processes the measurement of the previously mentioned process as well as the length change of the test specimen need to be included. This is not necessary for creep tests.

2.3.2 Constitutive equation for relaxation behaviour

The formulation of a constitutive equation for the viscoelastic material behaviour follows from the results of the relaxation test. After the creep test, the temporal reduction of the stress in the test specimen is associated with a temporal change of the Young's modulus. This is generally referred to as the relaxation modulus [4] (p310-311).

$$\sigma(t) = E(t)\varepsilon \quad (2.38)$$

The main problem of the description of viscoelastic behaviour using Hooke's law is that the information about the load history is not considered. To consider the influence of the load history, the strain rate $\dot{\varepsilon}$ is introduced, which is coupled with the strain via the following relationship.

$$d\varepsilon = \frac{d\varepsilon}{d\tau}d\tau = \dot{\varepsilon}d\tau \quad (2.39)$$

In order to properly take the influence of the load history into account for the entire time domain, the relaxation modulus and the instantaneous strain rate are integrated over the relaxation time τ [4] (p310-311).

$$\sigma(t) = \int_0^t E(t-\tau)\dot{\varepsilon}d\tau \quad (2.40)$$

Thus, the constitutive equation for the viscoelastic material behaviour is defined for the uniaxial stress and strain state. However, since multiaxial stress states often occur in real parts and components, this constitutive law requires generalisation for general stress states. The relaxation modulus as a function of the loading history is not known a-priori. It will be introduced at a later point of this thesis.

2.3.3 Generalised constitutive equation for viscoelasticity

The aim of this subsection is to describe the constitutive law for general deformation states. The stress and strain state in equation (2.40) can be decomposed into a volumetric part $\varepsilon_{ij}^{(vol)}$ and a deviatoric part $\varepsilon_{ij}^{(dev)}$ [4] (p312).

$$\varepsilon_{ij} = \varepsilon_{ij}^{(dev)} + \varepsilon_{ij}^{(vol)} \quad (2.41)$$

This equation can be rewritten by using the Kronecker delta δ_{ij} . The Kronecker delta δ_{ij} is a mathematical operator from the field of algebra often used for vector or matrix operations. The Kronecker delta δ enables case distinctions. It is defined as follows.

$$\delta_{ij} = \begin{cases} 1, & \text{if } i = j \\ 0, & \text{if } i \neq j \end{cases} \quad (2.42)$$

Thus the strain tensor decomposition can be written as

$$\varepsilon_{ij} = \varepsilon_{ij}^{(dev)} + \varepsilon^{(vol)} \delta_{ij} \quad (2.43)$$

The volumetric strain equals one third of the trace of the tensor, i.e., one third of the first invariant of the strain tensor, as shown in the equation below,

$$\varepsilon^{(vol)} = \frac{1}{3} \text{tr}(\varepsilon_{ij}) = \frac{1}{3} (\varepsilon_x + \varepsilon_y + \varepsilon_z) \quad (2.44)$$

where ε_x , ε_y and ε_z are the strains in the different directions of space. By using Hooke's law, this equation transforms into

$$\varepsilon^{(vol)} = \frac{3(1-2\nu)}{E} (\sigma_x + \sigma_y + \sigma_z) \frac{1}{3} = \frac{\sigma^{(vol)}}{K} \quad (2.45)$$

where $K = \frac{E}{3(1-2\nu)}$ is the volumetric modulus and $\sigma^{(vol)} = \frac{\sigma_x + \sigma_y + \sigma_z}{3}$ is the hydrostatic pressure or the volumetric stress. Thus, the volumetric stress is connected to the strain state by

$$\sigma_{ij}^{(vol)} = K \varepsilon^{(vol)} \delta_{ij} \quad (2.46)$$

The consideration of the load history delivers the volumetric part of the constitutive equation for viscoelastic behaviour.

$$\sigma_{ij}^{(vol)} = \int_0^t K(t-\tau) \dot{\varepsilon}^{(vol)} \delta_{ij} d\tau \quad (2.47)$$

As a next step, the deviatoric part of the constitutive law is searched. For $i \neq j$ follows

$$\varepsilon_{ij}^{(dev)} = \frac{1}{2} \gamma_{ij} = \frac{1}{2G} \sigma_{ij}^{(dev)} \quad (2.48)$$

where $\gamma_{ij} = \frac{\sigma_{ij}^{(dev)}}{2G}$ is the shear distortion, G is the shear modulus. The entries of the deviatoric stress tensor are computable by:

$$\sigma_{ij}^{(dev)} = \int_0^t 2G(t-\tau) \dot{\varepsilon}_{ij}^{(dev)} d\tau \quad (2.49)$$

The diagonal entries of the stress tensor are obtained by a decomposition of the stress tensor. The simple addition of the volumetric part and the deviatoric part of the constitutive equation delivers the full constitutive equation, for describing the viscoelastic behaviour.

$$\sigma_{ij}(t) = \int_0^t \left[K(t-\tau) \dot{\varepsilon}^{(vol)} \delta_{ij} + 2G(t-\tau) \dot{\varepsilon}_{ij}^{(dev)} \right] d\tau \quad (2.50)$$

This equation shows the time-dependent deformation behaviour for viscoelastic materials such as polymers. For many polymers the volumetric relaxation is smaller than the deviatoric relaxation. For this case, the material behaviour is well described by the following equation [1].

$$\sigma_{ij}(t) \approx \int_0^t 2G(t-\tau) \dot{\varepsilon}_{ij}^{(dev)} d\tau \quad (2.51)$$

The volumetric and the shear modulus are not only functions of time, they are also functions of temperature. To describe the influence of temperature on material parameters time-temperature-superposition laws (shifting functions) are used.

2.3.4 Linear and non-linear viscoelasticity

In the range of linear viscoelasticity, there is a linear relationship between stress and strain. Linear viscoelastic material parameters are functions of temperature and time $E(t, T)$. Linear viscoelasticity occurs in the range of small deformations, whereas non-linear viscoelastic material parameters also depend on the load magnitude $E(t, T, \sigma)$. Here, the linear relationship between stress and strain no longer exists. Non-linear viscoelasticity occurs in the range of larger deformations. Thus it is also referred to as large strain viscoelasticity. For this case no generally applicable mechanical equation of state can be formulated to describe the material behaviour.

In Abaqus, linear viscoelastic material behavior is modeled by a combination of a linear elastic material model and viscoelasticity. The viscoelastic material parameters describe the time dependence of the parameters of the linear elastic material model.

Nonlinear viscoelastic material behavior can be modeled by a combination of a hyperelastic material model and viscoelasticity. The hyperelastic material parameters describe the nonlinear relationship between stress and strain at higher stresses.

2.3.5 Prony series

The time dependent behaviour of the volumetric, or bulk modulus K , and the shear modulus G are described by using the Prony series [1]. That the time dependent relaxation of the elastic material constants is described by an exponential series follows from the solution of the inhomogeneous differential equation (2.35), more precisely, from the homogeneous solution. The particulate solution of the differential equation yields the steady state, i.e. $E(t = \infty)$.

$$G(t) = \sum_{i=1}^N G_i e^{-\frac{t}{\tau_i}} \quad (2.52)$$

$$K(t) = \sum_{i=1}^N K_i e^{-\frac{t}{\tau_i}} \quad (2.53)$$

The Prony series approximate the influence of the relaxation processes in accordance to the material stiffness by a finite series of values. In reality the relaxation processes in a material cannot be determined by a finite number of discrete values. The exact determination of the relaxation processes needs a broad relaxation spectrum.

Finite element software packages like ABAQUS or ANSYS use the Prony series to describe the viscoelastic behaviour. These programs work with the normalised Prony series parameters as input parameters [1]. The Prony parameters are normalised with the initial shear G_0 or bulk modulus K_0 .

$$g(t) = \frac{G(t)}{G_0} = \frac{1}{G_0} \left(\sum_{i=1}^N G_i e^{-\frac{t}{\tau_i}} \right) \quad (2.54)$$

The Prony series parameters g_i and τ_i only partially describe the material behaviour. In addition to the time dependent viscoelastic behaviour, a material model for the spontaneous elastic behaviour is needed. A linear elastic material model for spontaneous material response is used for small deformations and displacements, whereas larger deformations require using a hyperelastic material model for the spontaneous material reaction.

2.3.6 Periodic loads

Due to the mechanical behaviour of a viscoelastic material showing a time dependent viscous part, the material response to a periodic load results in an output signal that shows a phase shift to the input signal (Figure 2.9).

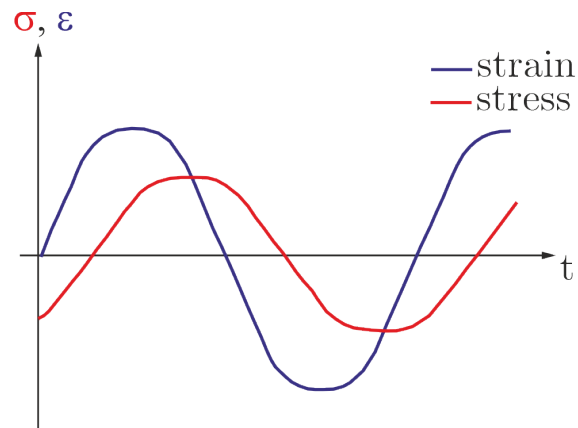


Figure 2.9: Effects of periodic loads to stress and strain for viscoelastic materials

Therefore, if a sinusoidal strain signal $\varepsilon(t)$ is applied to the material according to 2.55,

$$\varepsilon(t) = \varepsilon_0 \sin(\omega t) \quad (2.55)$$

where ε_0 is the strain amplitude and ω is the circular frequency of the oscillation, the following stress function $\sigma(t)$ will follow,

$$\sigma(t) = \sigma_0 \sin(\omega t + \delta) \quad (2.56)$$

where σ_0 is the resulting stress amplitude and δ is the phase shift. The phase shift is usually expressed for periodic loads in terms of a Young's modulus defined as a variable in a complex space (Figure 2.10).

$$E^* = |E| = E' + iE'' \quad (2.57)$$

where the storage modulus E' describes the energy, which is stored during every load cycle and then released at the end of the load cycle. The loss modulus E'' describes the energy, that is dissipated during every load cycle due to the internal friction of the material.

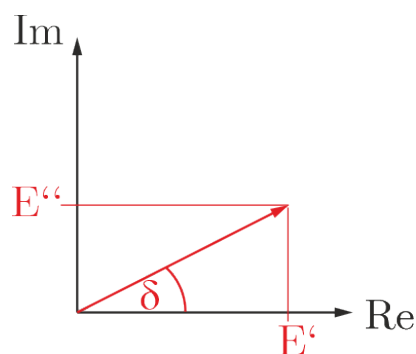


Figure 2.10: Complex Young's modulus in Gaussian plane

Storage and loss moduli are functions of the temperature, but they are also influenced by the frequency of the load signal. The ratio of the loss and the storage modulus defines the phase angle δ between the stress and the strain history.

$$\tan \delta = \frac{E''}{E'} \quad (2.58)$$

A small phase angle means that the elastic behaviour prevails over the viscous behaviour. For $\delta = 0^\circ$ the material behaves like an ideal elastic solid and for the $\delta = 90^\circ$ like an ideal viscous fluid. Further, the loss energy is converted into thermal energy. If the stress and the strain are combined into a $\sigma - \varepsilon$ -diagram the result is a closed curve (hysteresis) as shown in Figure 2.10.

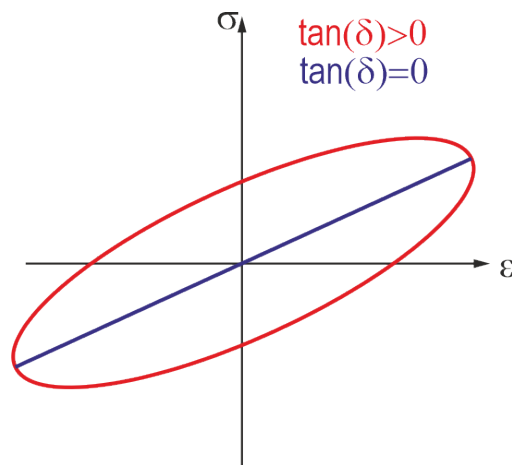


Figure 2.11: Hysteresis curve in the stress-strain diagram

The shape of the hysteresis curve is influenced by the storage and the loss modulus. In case the loss modulus approaches 0, the hysteresis curve becomes a straight line through the origin of the coordinate system. For an increasing loss modulus, the area of the hysteresis also increases. The complete energy lost $q^{(diss)}$ per load cycle equals the area of the hysteresis.

$$q^{(diss)} = \oint \sigma d\varepsilon \quad (2.59)$$

Using the definition for the strain rate equation (2.48), this equation leads to

$$q^{(diss)} = \int_t \sigma \dot{\varepsilon} dt \quad (2.60)$$

For general multi-axial stress states, the equation is formulated by introducing the corresponding tensors.

$$q^{(diss)}(\underline{x}, t) = \int_t \sigma_{ij} \dot{\varepsilon}_{ij} dt \quad (2.61)$$

The internal heating $\dot{q}^{(diss)}$ of the body stems from the rate of specific energy input.

$$\dot{q}^{(diss)}(\underline{x}, t) = \sigma_{ij} \dot{\varepsilon}_{ij} \quad (2.62)$$

whereby the following summation convention applies:

$$A_{ij} A_{ij} = \underline{\underline{A}} : \underline{\underline{A}} = A_{11} A_{11} + A_{12} A_{12} + \dots + A_{21} A_{21} + A_{22} A_{22} + \dots \quad (2.63)$$

2.3.7 Heat conduction in solids

The energy balance for a closed system follows in accordance to the first law of thermodynamics.

$$dU = dQ - dW \quad (2.64)$$

Where U is the internal energy, Q is the thermal energy and W is the mechanical energy. The power balance for the closed system then reads

$$\frac{dU}{dt} = \frac{dQ}{dt} - \frac{dW}{dt} \quad (2.65)$$

The change in the internal energy of the body is proportional to the mass m of the body and the change in temperature T , with c_V being the specific heat capacity for constant volume.

$$dU = mc_V dT \quad (2.66)$$

With $m = \int \rho dV$ the derivative with respect to time delivers.

$$\frac{dU}{dt} = \int_V \rho c_V \frac{dT}{dt} dV \quad (2.67)$$

where ρ is the mass-density of the solid. The heat flow penetrating the surface of the body via an infinitesimal area element dA is shown in Figure 2.12 with \underline{n} being the normal vector from a surface.

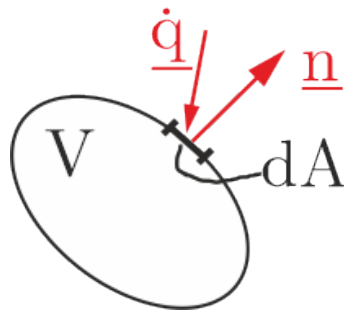


Figure 2.12: Heat Flux through the surface of a solid

$$\frac{dQ}{dt} = - \oint_A \underline{\dot{q}} \cdot \underline{n} dA \quad (2.68)$$

The surface integral converted into a volume integral using the divergence theorem yields equation (2.69).

$$\oint_A \underline{\dot{q}} \cdot \underline{n} dA = \int_V \nabla \cdot \underline{\dot{q}} dV \quad (2.69)$$

Fourier's law states that the heat flow is proportional to the local temperature gradient. This further leads to

$$\underline{\dot{q}} = -\lambda \nabla T \quad (2.70)$$

where λ represents the heat conduction coefficient. Thus the change of the thermal energy is defined by following equation.

$$\frac{dQ}{dt} = \int_V \underline{\nabla} \cdot [\lambda \underline{\nabla} T] dV \quad (2.71)$$

Power generally consists of the time derivative of volume changing work and a part representing dissipative processes inside the body. The volume dilation changing part is negligible in solids, thus

$$\frac{dW}{dt} = \int_V \dot{q}^{(diss)} dV \quad (2.72)$$

where $\dot{q}^{(diss)}$ is the dissipated power, which in the case of a viscoelastic material, is a function of the strain rate tensor $\dot{\epsilon}_{ij}$. Differentiating with respect to the volume yields the partial differential equation, which governs the temperature field in a solid.

$$\rho c_V \frac{\partial T}{\partial t} = \underline{\nabla} \cdot [\lambda \underline{\nabla} T] + \dot{q}^{(diss)}(\dot{\epsilon}_{ij}) \quad (2.73)$$

2.3.8 Creep behaviour of polymers

The deformation of a viscoelastic material consists of three major stages. (i) a spontaneous elastic response, (ii) a time dependent reversible relaxation (creep) deformation and (iii) a time dependent irreversible plastic (yield) deformation. The creep behaviour in polymers is initiated by sliding between the macromolecular chains, so-called shear yielding. The creep behaviour is often partitioned into three parts.

In the first stage (the primary creep stage) the creep behaviour is characterised by a predominance of hardening mechanisms compared to softening mechanisms inside the material. The secondary creep stage is identified by an equilibrium state between hardening and softening mechanisms. The third stage occurs when the softening mechanisms prevail. The development of these stages depends on the material, environmental and load conditions. According to the conditions and the material itself, there is also the possibility of omitting or skipping a stage [3] (p273-283).

The creep behaviour is a function of the stress state σ_{ij} , the time t and the temperature T . A constitutive equation for creep is often formulated implicitly [3] (p273-283).

$$f(\dot{\varepsilon}_{ij}^{(creep)}, \sigma_{ij}, T, t) = 0 \quad (2.74)$$

In explicit form, the creep law, therefore is formulated as

$$\dot{\varepsilon}_{ij}^{(creep)} = \dot{\varepsilon}_{ij}^{(creep)}(\sigma_{ij}, T, t) \quad (2.75)$$

2.3.9 Calibration of the material data

The description of the material behaviour requires a material model and the material parameters which are found through a calibration using experimental data. To calibrate the material parameters one or multiple sets of experimental data are required. On the one hand, experimental tests always include experimental errors, on the other hand, the calibration of the material parameters requires solving a mathematically over-constrained set of equations. Calibration of the material data typically uses an optimisation algorithm which must ensure it finds the global minimum. Bergstroem describes some optimisation algorithms for material modelling in [4] (p437-446). It is advisable to choose a slow optimisation algorithm which is more likely to find a global minimum of the target function.

Calibration of the Prony parameters

Although for calibrating the Prony series parameters MCalibration is used, the principles of the data fitting is explained (Figure 2.13). For fitting the Prony series parameters relaxation- or creep- test data are necessary. Using these data allows to compute the relaxation modulus $E(t)$ or creep compliance $J(t)$, the spontaneous modulus E_0 and the Poisson ratio ν . The shear modulus $G(t)$ and the volumetric modulus $K(t)$ are then detected for isotropic materials. If relaxation test data are available, the Prony parameters are calibrated directly. Whereas, if creep test data are available the creep compliance has to be converted into a relaxation modulus using a nonlinear system of equations described in [3]. Several measurement data sets are used to calibrate the material parameters. An optimisation algorithm calibrates the material parameters, using equation (2.54), so that the experimental data are described as accurately as possible by the material model.

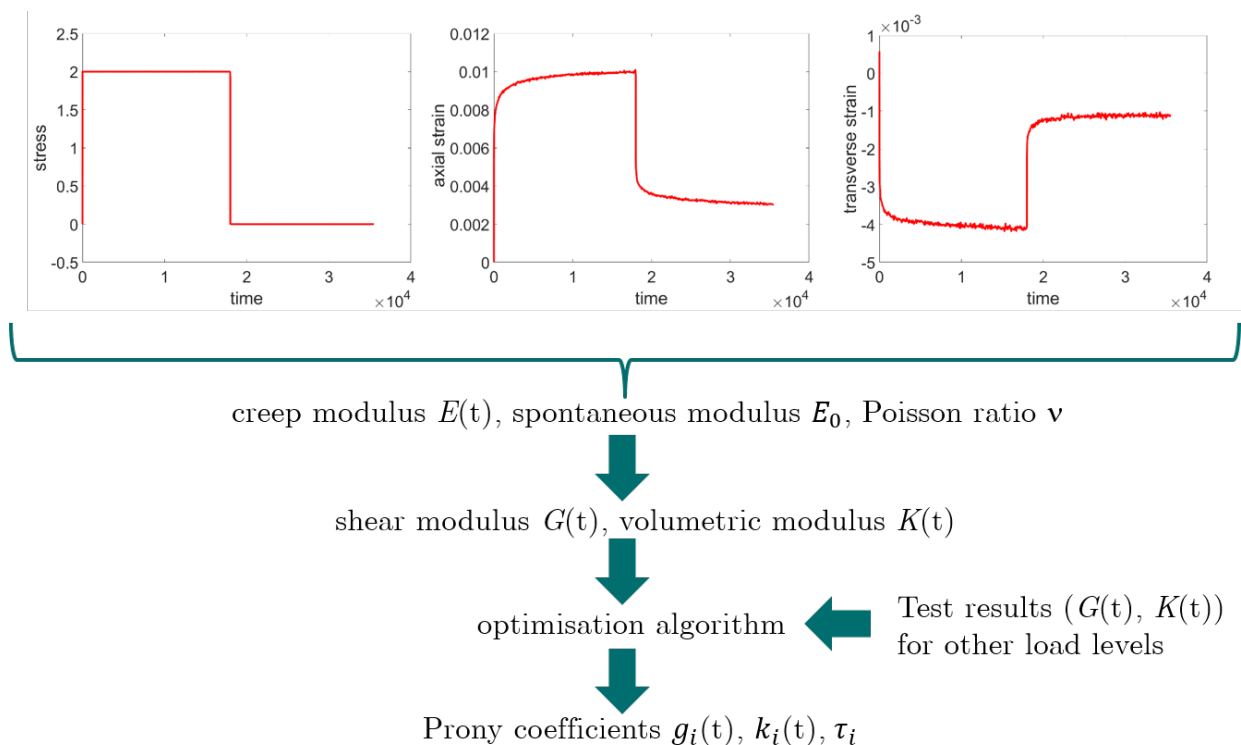


Figure 2.13: Principle of calibrating the Prony series parameters

According to Bergstroem [4] (p345-346) the result of a creep test or a relaxation test is in principle sufficient to fit the parameters of the Prony series. Data from creep tests are used to calibrate the viscoelastic material parameters (Prony series parameters). In the creep test, standardized specimens are subjected to a constant load $\sigma = \text{const}$. As a result of relaxation processes inside the material, there is a reduction in material stiffness or an increase in material compliance. This increase in compliance results in a change in strain over time at constant test load. The change in the length of the test specimen is measured during the test. In addition, the change in length in the transverse direction is also measured. The specified test parameters (stress σ) as well as the quantities resulting from the measurements of the changes in length (axial strain and transverse strain) allow the material parameters to be fitted, according to Figure 2.13.

2.3.10 Calibration using MCalibration

In this thesis the material parameters were calibrated using the software MCalibration. It includes various material models for solid polymers, from linear viscoelastic, over hyperelastic to different material models specified for single materials like PE-HD. In MCalibration also different optimisation algorithms for data calibration are implemented. The results of material data calibration are found in chapter 4-Results.

To calibrate the material parameters on the basis of the test results, it is recommended to extend the measurement curves piece by piece. This means that the entire curve should not be calibrated at once, but piece by piece. As soon as a piece of the curve is well calibrated, one should use a larger measuring range and calibrate the data again. In this way, a much better approximation of the measured values is achieved by means of the material model used. In combination with an efficient optimisation algorithm, which actually searches for the global minimum, a parameter set is found that describes the material behaviour well.

2.3.11 Time-temperature superposition

Polymers show a strongly temperature dependent material behaviour even at low temperatures. To describe the temperature dependency of the mechanical parameters, so called temperature shifting functions are used. Various temperature shifting functions exist. Typically the William-Landel-Ferry-Equation (WLF) or the Arrhenius equation are used. The WLF-Equation delivers a good approximation of the temperature dependency of the mechanical behaviour in the temperature range of $T_G - 50\text{K}$ up to $T_G + 50\text{K}$ [4] (p341-345).

$$\log(a_T) = -\frac{C_1(T - T_{ref})}{C_2 + T - T_{ref}} \quad (2.76)$$

Where a_T is the shifting factor, T_G is the glass transition temperature of the material, T_{ref} is the reference temperature and C_1 and C_2 are material dependent parameters.

The shifting function is defined using the $\log(G)$ - $\log(t)$ -characteristics (Figure 2.14).

$$\log(a_T) = \log(t_0) - \log(t_1) = \log\left(\frac{t_0}{t_1}\right) \quad (2.77)$$

Thus, the time-temperature-shifting factor is defined.

$$a_T = \frac{t_0}{t_1} \quad (2.78)$$

For a shift from a lower temperature to a higher temperature, the shifting coefficient $a_T > 1$, while for a shift from a higher temperature to a lower temperature $a_T < 1$. If the material parameters at a certain temperature (reference temperature) are known and if the parameters of the chosen shift approach are known, the material parameters for a different temperature can be determined using the principle of time-temperature superposition.

Calibration of the shifting parameters

The principle of calibration of the WLF parameters is shown in figure 2.14. The calibration of the coefficients of the WLF equation is based on the data of creep tests, which were measured at different temperatures. From these creep curves, the creep modulus $E(t)$ is determined as a function of time. The creep moduli are plotted over time in a double logarithmic diagram. The shift factors a_T are then determined from the $\log(E)$ - $\log(t)$ diagram. The temperature shift factor is defined by equations (2.77) or (2.78), respectively. This works because the temperature influences the speed of the relaxation processes in the material. Higher temperatures cause the relaxation processes to take place more quickly. This leads to the curve being shifted in the direction of shorter times. While lower temperatures slow down the relaxation processes and thus shift the curve towards higher relaxation times. It is important to note that the relaxation processes in the material have the same causes, so the calculation approaches are limited to certain temperature levels. An optimisation algorithm then calibrates the WLF parameters C_1 and C_2 according to equation (2.76).

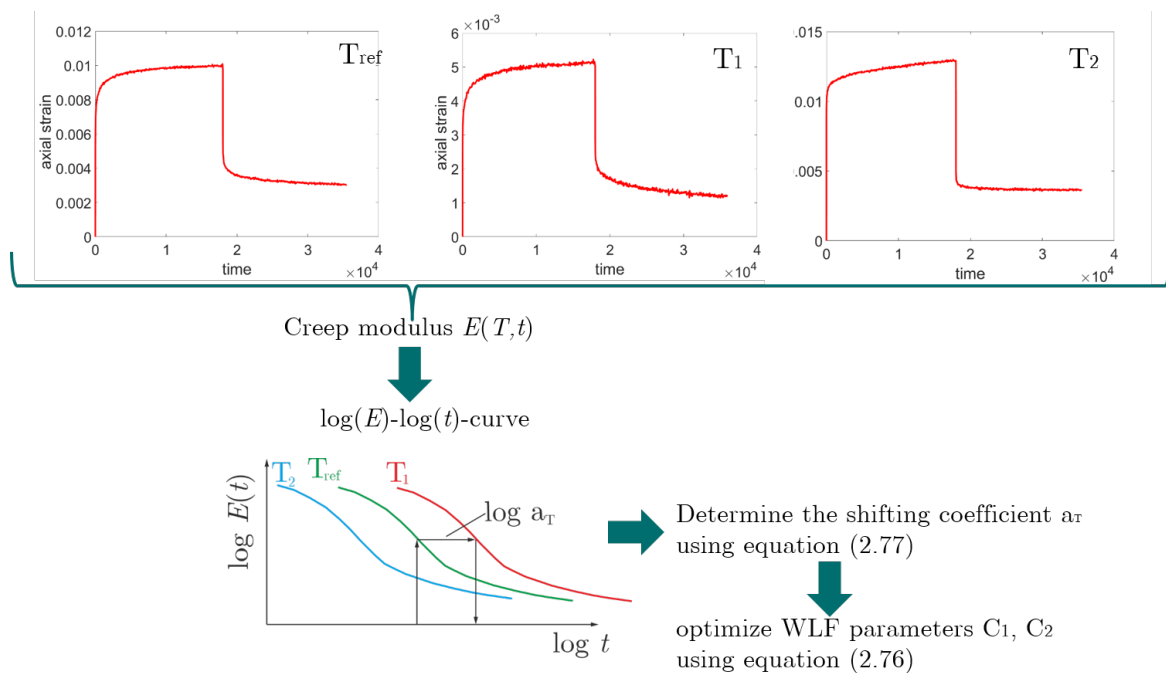


Figure 2.14: Principle of calibrating temperature shifting parameters

2.4 Viscoplasticity

The corresponding models have been developed on the basis of experimental values. Some of those models exhibit a fairly high prediction accuracy. In principle, a large number of viscoplastic material models exist. However, many of these models are only of limited use for polymer materials (for example the Johnson Cook model), as they cannot represent the unloading step well under cyclic loading [4] (p365-366). On the other hand, these models have often been developed for a specific material (for example unfilled PE-HD), which is very common in practical applications. In general, the Parallel Rheological Framework (PRF) model shows good agreement with practical experimental results.

2.4.1 Parallel Rheological Framework (PRF-Model)

The parallel rheological framework (PRF-Model) was specifically developed to predict the viscoplastic behaviour of thermoplastics (Figure 2.15). The structure of the model essentially corresponds to that of the generalised Maxwell model. In contrast to the Maxwell model, the spring element describing the long-term equilibrium behaviour, is not based on linear-elastic material behaviour but on a hyperelastic material model (Yeoh-model). The friction contact element is based on a plasticity model. Bergstroem [4] recommends a power law for polymer based materials. More detailed information about this material model is found in the literature, e.g. [4] (p417-431).

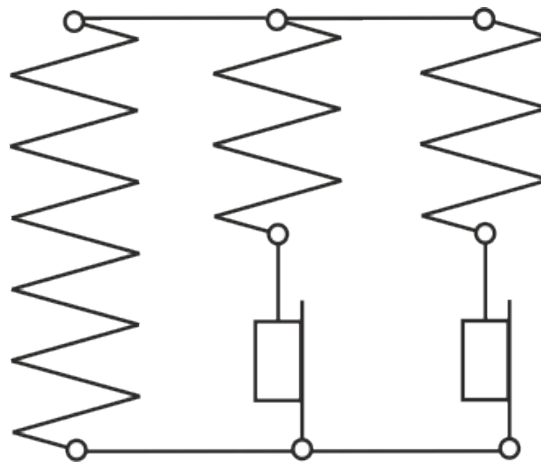


Figure 2.15: Three network model

2.5 Hyperelasticity

Hyperelastic material models are applied to predict non-linear elastic material behaviour at larger strains. A variety of hyperelastic material models are available for this purpose. They are based on the Helmholtz free energy (strain energy) and can be used not only for elastomeric materials, but also to describe the non-linear elastic behaviour of thermoplastics. A hyperelastic material behaviour describes the spontaneous elastic material behaviour. The advantages are the availability without the need to program subroutines, the simple calibration and the efficiency with regard to the calculation. The disadvantage is that hyperelastic material models do not take into account heating by cyclic loading [4] (p298-299). From the large number of available material models, the Yeoh model is used due to its good prediction accuracy.

2.5.1 Yeoh model

Like other hyperelastic material models, the Yeoh model is based on the Helmholtz free energy. The strain energy of this material model is formulated as a third order degree polynomial of the first invariant of the strain tensor. In principle, however, higher order polynomials are also possible. More detailed information about this material model are found in additional literature, e.g. [4] (p245-250).

According to the Yeoh model, the Helmholtz free energy for a compressible continuum is defined as a third degree polynomial of the first invariant of Green's strain tensor, see equation (2.87). The second invariant is not considered, as many materials have a much stronger dependence on the first invariant [4] (p245-250). The influence of the third invariant of Green's strain tensor is only considered for compressible continua.

$$\psi(I_1^{(dev)}, I_3) = C_{10}(I_1^{(dev)} - 3) + C_{20}(I_1^{(dev)} - 3)^2 + C_{30}(I_1^{(dev)} - 3)^3 + \frac{K}{2}(\sqrt{I_3} - 1)^2 \quad (2.79)$$

Where ψ is the Helmholtz free energy and C_{10} , C_{20} , C_{30} , K are the required material parameters for the Yeoh model. I_1^* is the distortion (deviatoric) part of the first invariant and I_3 is the third invariant of Green's strain tensor. If there is no dependence of the Helmholtz free energy on the second invariant of Green's strain tensor, the Cauchy stress tensor follows from [4] (p245-250)

$$\sigma_{ij} = \frac{2}{\sqrt{I_3}} \frac{\partial \psi}{\partial I_1^{(dev)}} b_{ij}^{(dev)} + \frac{\partial \psi}{\partial \sqrt{I_3}} \frac{\partial I_1}{\partial E_{ij}} \quad (2.80)$$

Where E_{ij} is Green's strain tensor, I_1 is the first invariant of this tensor and $b_{ij}^{(dev)}$ is the deviatoric part of the left hand Green strain tensor

$$b_{ij} = F_{ij} F_{ij}^T \quad (2.81)$$

where F_{ij} is the deformation gradient. Equation (2.80) can also be written as follows

$$\sigma_{ij} = \frac{2}{\sqrt{I_3}} F_{ij} \frac{\partial \psi}{\partial E_{ij}} F_{ij}^T \quad (2.82)$$

Chapter 3

Modelling

3.1 Mechanical model of the problem

Due to the symmetry in geometry and loading of the cylinder ring, an axi-symmetric model is used. Because of the high elastic contrast, of steel and the polymer used for the cylinder ring, it is possible to model the piston and the cylinder wall as rigid bodies. This simplification reduces the computation time but also guarantees a high degree of accuracy. Figure 3.1 shows a sketch of the axisymmetric model, a cut is made through the cylinder ring in the r - z -plane. p_1 and p_2 are the pressures from the head- and crankshaft-side.

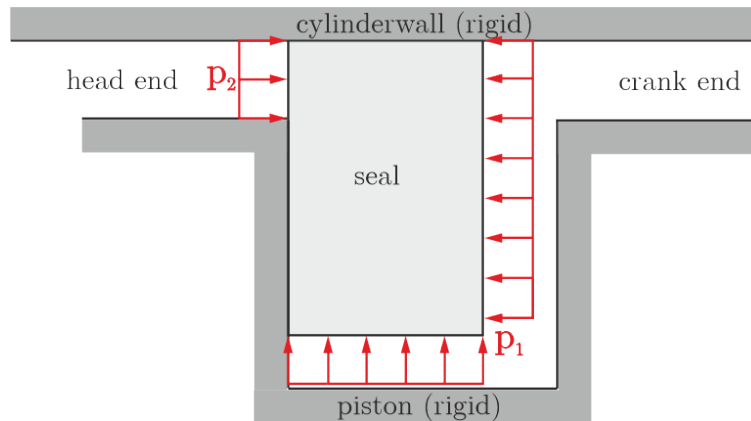


Figure 3.1: Sketch of the cylinder ring model

Figure 3.2 shows the parametrisation of the geometry of the axi-symmetric finite element model. The parametrisation of the model is used in the Python script and the same naming convention for the parameters is used (see appendix).

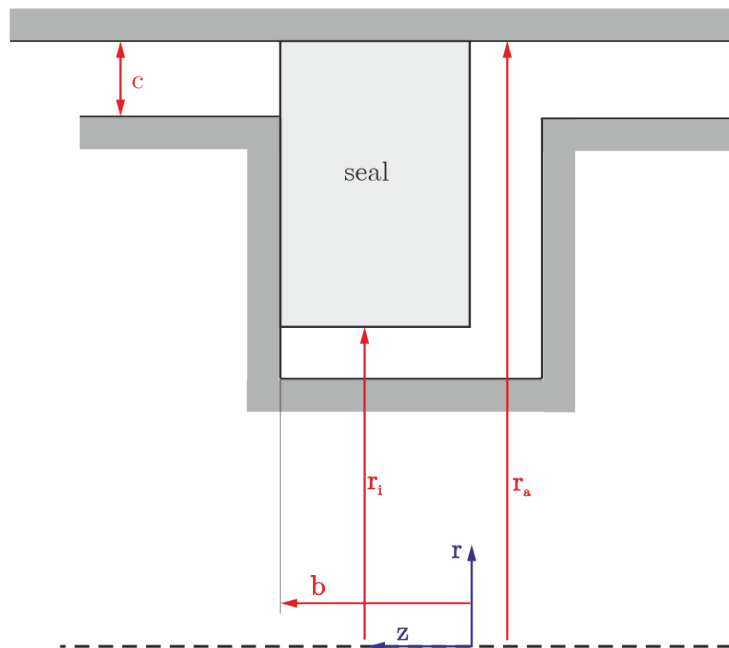


Figure 3.2: Parametrisation of the FE-model used in the Python script

The parameters are the inner radius r_i , the outer radius r_a , the axial thickness b and the cylinder ring protrusion c .

Figure 3.3 shows the FEM model in Abaqus CAE. The cylindrical ring is modelled as a deformable body. The piston, on the other hand, is modelled as a rigid body, whereas the cylinder wall is represented by the mechanical boundary condition XSYMM. This constraint locks the degree of freedom ($U_1 = 0$), i.e. the displacement in radial direction. However, the displacement in axial direction is not constrained. The piston is fixed at the reference point with the boundary condition ENCASTRE, which locks all degrees of freedom ($U_1 = U_2 = U_3 = UR_1 = UR_2 = UR_3 = 0$). For a more precise resolution of the critical area, marked by a rectangle in the upper left corner, it is partitioned and meshed more finely.

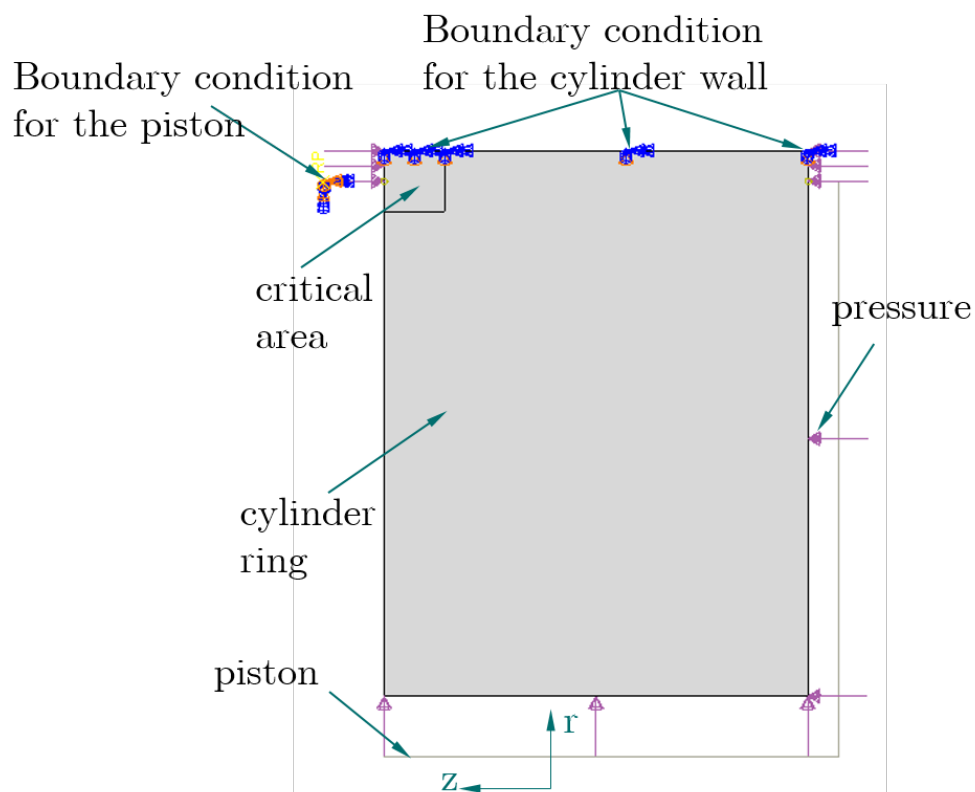


Figure 3.3: FE-model in Abaqus CAE

The applied pressures follow the time profiles described below in chapter 3.2.

3.1.1 Submodel

Since the maximum stress values occur in a very small area below the surface and the stress gradient is quite high, a very fine meshing of the critical area, marked in Figure 3.3 by a rectangle, is required. For this area to be resolved with sufficient accuracy, an element size of 0.001mm is required. A convergence study shows that an element size of 0.002mm already underestimates the stress values. For the sake of computational efficiency a submodel representing the critical area was defined, see Figure 3.4.

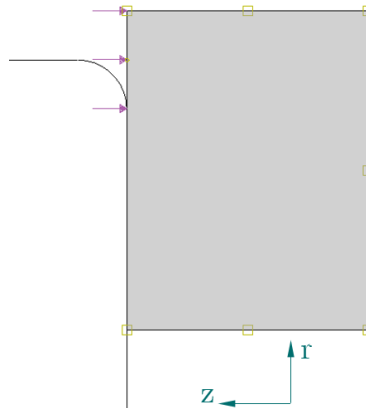


Figure 3.4: Submodel in Abaqus CAE

The Submodel takes advantage of Saint Venant's principle, which states that local stress peaks quickly subside. The displacements are determined by the global model see in Figure 3.3, then prescribed as boundary conditions. The submodel boundaries have to be chosen such that they are sufficiently far away from high stress concentrations so undesirable boundary influences on the results can be prevented.

4-noded axial-symmetric continuum elements (CAX4) are used to mesh the model. These elements have bilinear interpolation functions. In principle, elements with quadratic interpolation functions (CAX8 or CAX8R) are better suited to resolve the searched quantities more precisely. However, these elements are not used because they are not recommended for contact problems. Elements with reduced integration (CAX4R) are not used due to the possible occurrence of hourglassing.

3.2 Mathematical model for the load signal

Periodic signals, such as the pressure-time signal of a double acting piston compressor, can be addressed in terms of a Fourier series:

$$p(t) = \frac{a_0}{2} + \sum_{n=1}^{\infty} [a_n \cos(n\omega t) + b_n \sin(n\omega t)] \quad (3.1)$$

where a_0 and a_n represent the coefficients of the Fourier series and $p(t)$ represents the approximated signal. ω is the angular frequency of the periodic load function. The Fourier coefficients are calculated by using the following integrals

$$a_n = \frac{1}{T} \int_{t_1}^{t_2} f(t) \cos(n\omega t) dt \quad (3.2)$$

$$b_n = \frac{1}{T} \int_{t_1}^{t_2} f(t) \sin(n\omega t) dt \quad (3.3)$$

where $f(t)$ is the periodic load signal. ABAQUS CAE allows to implement the Fourier coefficients a_n and b_n of an approximated function. The great advantage of using Fourier series is that periodic signals can be well approximated. The pressure-time curves supplied by HOERBIGER Wien GmbH. are already well approximated with only a low-order Fourier series. The evaluation of the Fourier series coefficients are carried out with Matlab R2020. The coefficients are saved in a "txt"-file, which is then used in the Python script to describe the periodic course of the load. In principle, the pressure-time curve could also be approximated using piecewise linear functions. Another advantage of using a Taylor series approximation is that directly experimentally determined pressure-time curves can be used. This is particularly practical when the ratio of the pressure levels changes.

3.2.1 Load signal crank end (CE)

Figure 3.5 shows a normalized pressure-time-characteristic of the double acting piston compressor for the crank end and for a crank shaft rotational speed of 430 revolutions per minute. Furthermore, the approximation of the load function with a Fourier series of order 8 is shown, see Figure 3.5.

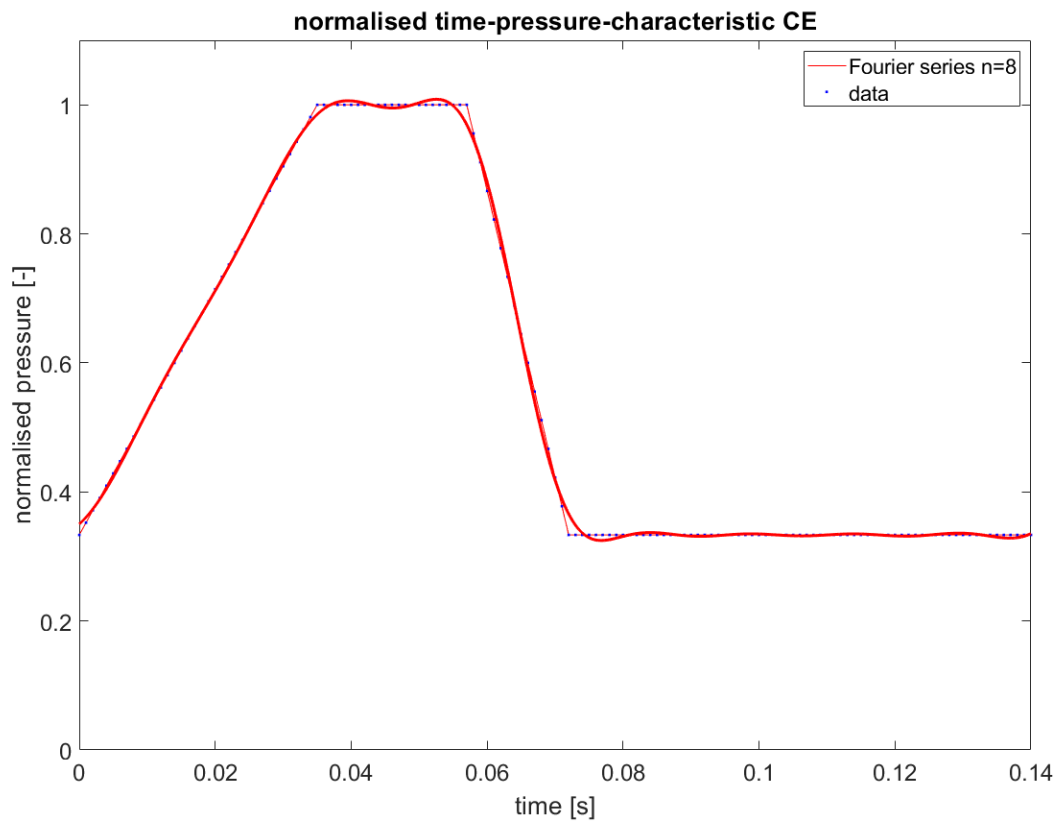


Figure 3.5: Load signal for crank end, Calculated data and Fourier approximation

The reason why the pressure curve is normalised is quite simple. By adjusting the required time for one revolution of the crank shaft, the load profile can be adapted for any desired speed. To change the crankshaft speed, only the time for one load cycle needs to be adjusted. To define the pressure curve, the pressure amplitudes must be defined when the normalized pressure curve is known. The pressure curve can thus be changed at will with the time for one revolution of the crankshaft and the maximum amplitude.

3.2.2 Load signal head end (HE)

Figure 3.6 shows the normalized pressure-time-characteristic for the head end of the double acting piston compressor. As Figure 3.5 and Figure 3.6 show, the pressure changes between 33% and 100% of the normalised pressure in the course of a working cycle.

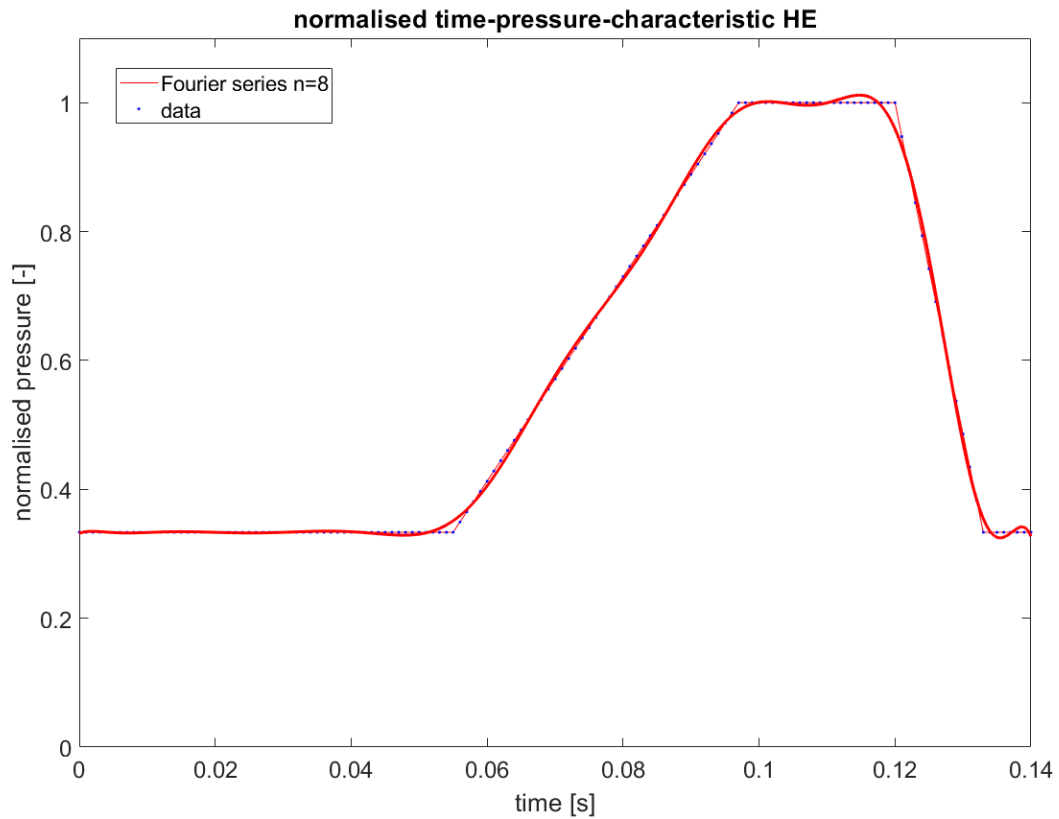


Figure 3.6: Load signal for head end, Calculated data and Fourier approximation

The MATLAB script for calculating the coefficients of the Fourier series is available in the appendix.

3.3 Thermal model

In addition to mechanical loads thermal loads act on the cylinder ring. The temperature field in the cylinder ring reaches a quasi stationary state after a warm-up period, depending on the specific pressure level and the rotational speed of the crank shaft. The thermal simulation is necessary because the stiffness of the material and also the strength values are strongly temperature dependent. Furthermore, an inhomogeneous temperature field leads to additional stresses in the component.

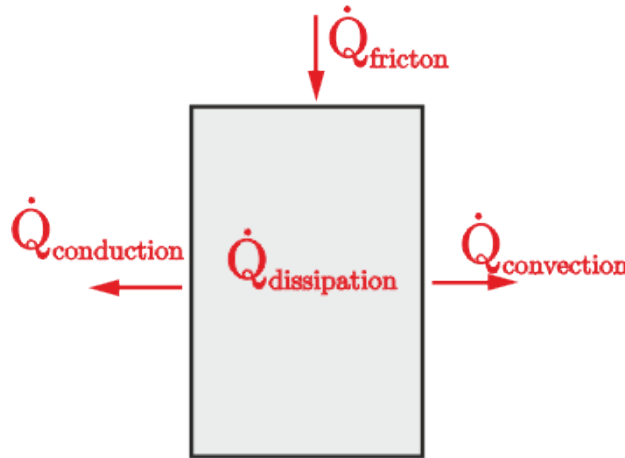


Figure 3.7: Heat flux balance for the cylinder ring

The initial transient heat conduction problem takes into account the heat fluxes from the environment $\dot{Q}_{convection}$ and $\dot{Q}_{conduction}$ and generated from dissipation processes inside the material $\dot{Q}_{dissipation}$ (Figure 3.7). $\dot{Q}_{friction}$ results from the friction between cylinder wall and cylinder ring. $\dot{Q}_{convection}$ arises through convection between cylinder ring and the compression medium. The heat flux $\dot{Q}_{conduction}$ occurs at the contact points with other solids. The heat flux balance for the cylinder ring is thus represented by the following equation

$$\dot{Q}_{dissipation} + \dot{Q}_{friction} + \dot{Q}_{convection} + \dot{Q}_{conduction} = mc_p \frac{\partial T}{\partial t} \quad (3.4)$$

where m is the mass of the cylinder ring and c_p is the specific heat capacity at constant pressure. After a certain time, the system reaches a quasi-stationary state, from which the temperature changes only insignificantly. Then it solely fluctuates around a certain value.

$$\dot{Q}_{dissipation} + \dot{Q}_{friction} + \dot{Q}_{convection} + \dot{Q}_{conduction} \approx 0 \quad (3.5)$$

The thermal problem leads to an inhomogeneous temperature field in the cylinder ring. However, most of the pertaining thermal properties are unknown, e.g. the convection coefficient. Also, data for the flow conditions in the working chamber of the compressor are missing. For precise predictions of the inhomogeneous temperature field inside the cylinder ring additional data and flow simulations are required. Thus, for the sake of simplicity the temperature field inside the cylinder ring is assumed to be homogeneous at $110^\circ C$.

Due to the dissipative material model, a fully coupled thermomechanical analysis is necessary in principle for this task. The thermal and mechanical field equations are coupled because the dissipated power is a function of the stress and the strain rate tensor according to equation (2.62). However, the fully coupled analysis is not carried out because too much material data are lacking. The estimation of the heating due to dissipation in the material is carried out under adiabatic conditions. Although this does not correspond to the actual conditions, it does allow certain estimates to be made. The heat conduction simulation is carried out with DCAX4 elements. The results of the thermal simulation are shown in chapter 4.4.5.

Chapter 4

Results

4.1 Comparison of axisymmetric and 3D model

To investigate the quality of the model predictions it is essential to compare the results of the axisymmetric model with the results of 3D-models. Different types of cylinder rings from HOERBIGER Wien GmbH. are shown in figure 4.1. For the comparison with the axisymmetric model, the cylinder ring designs a) and b) according to Figure 4.1 are used. The results are transferable to most other cylinder ring designs. Only for designs f) and g.) are the results not representative.

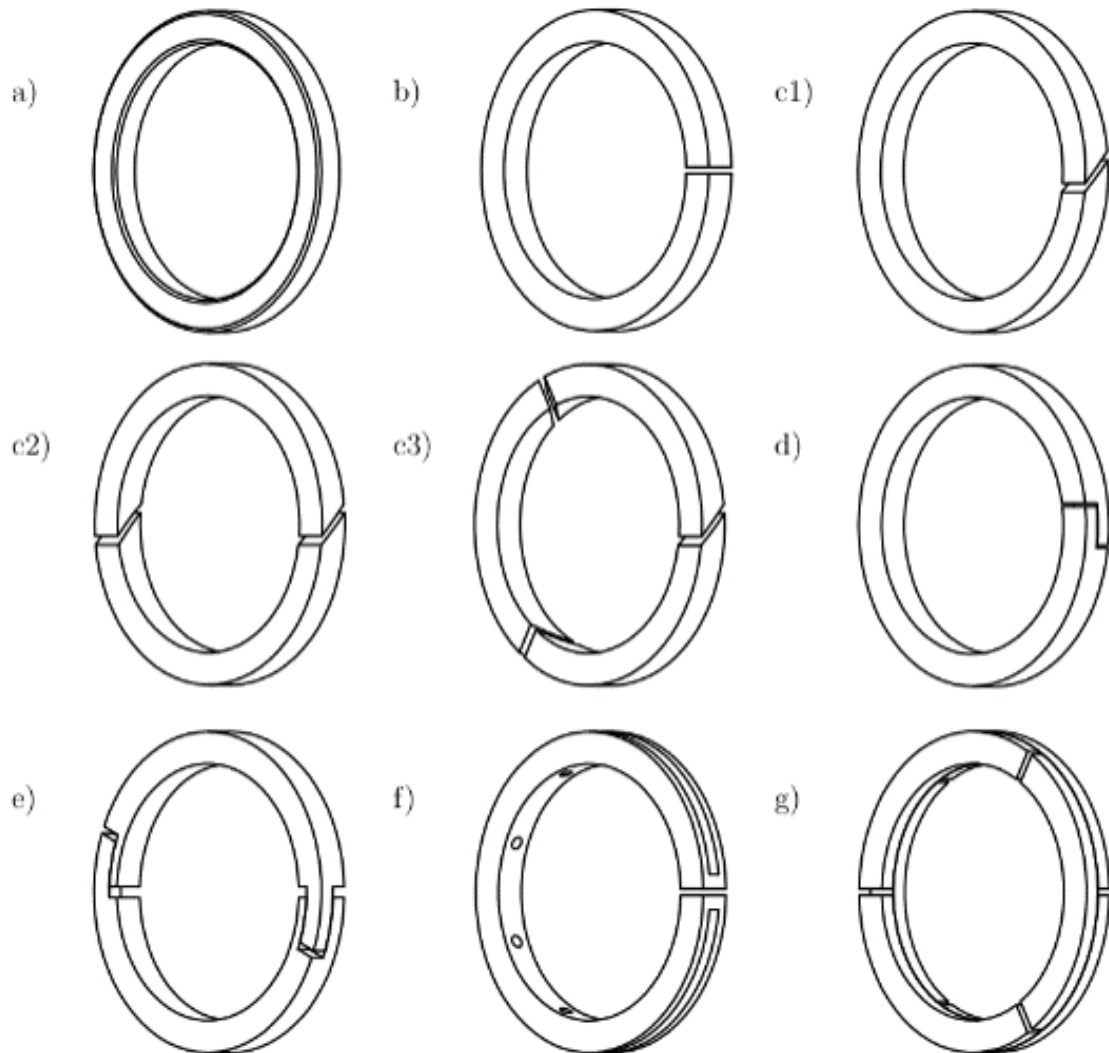


Figure 4.1: Cylinder rings from HOERBIGER Wien GmbH. [10]

4.1.1 Stress field in the cylinder ring

In the large parts of the cylinder ring, the stress field is essentially homogeneous, see Figure 4.2. In the area of the piston edge there are resulting stress concentrations due to the bending of the cylinder ring around the edge. Hence, the stress field in this area exhibits a high stress gradient. For the comparison between the stress states in the computed axisymmetric versus the 3D models, this is the major area of interest.

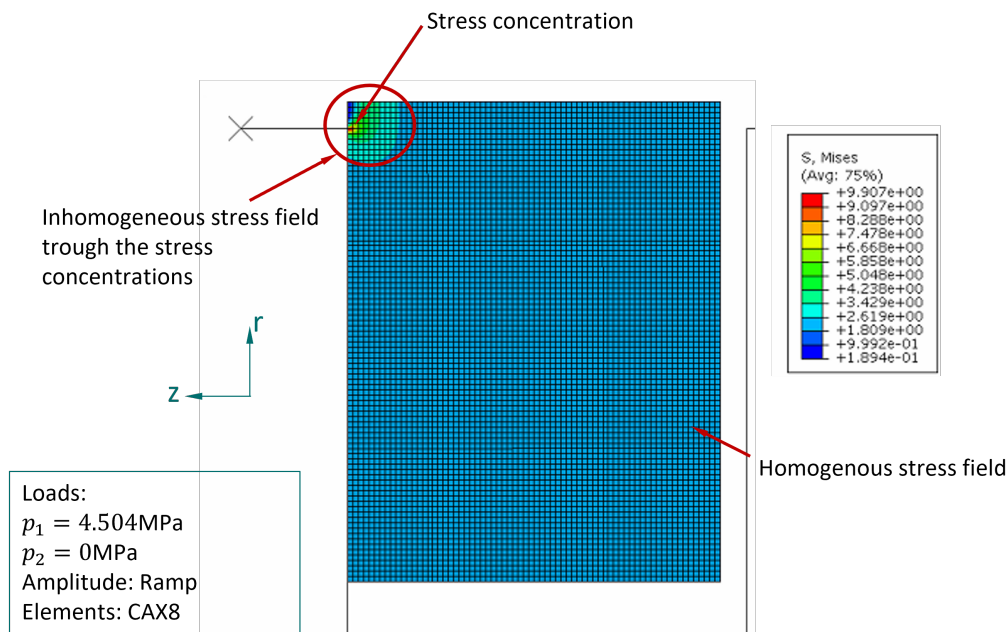


Figure 4.2: Stress field in the cylinder ring

In order to be able to compare the simulation results between the axisymmetric model and the 3D models, elements with the same or very similar dimensions, as well as the same order of the interpolation functions, are chosen. Furthermore, the same loading conditions have to be provided. Since an axisymmetric stress state is present in the uncut cylinder rings, a high agreement of the results is expected.

4.1.2 Stress field in the axisymmetric model

Figure 4.3 shows the stress field of the axisymmetric model in the critical area. Linear interpolation functions are used which are more suitable for modelling contact between the cylinder ring and the piston than quadratic interpolation functions. The maximum stresses occur in a very local area in the region of the contact point between the piston and the cylinder ring. A later analysis, using a submodel also shows that the maximum stresses occur slightly below the surface. This effect becomes more pronounced the higher the load level and subsequently the deformation of the cylinder ring. This analysis using a submodel (see Figure 4.26) also shows that there are considerable stress gradients in the cylinder rings.

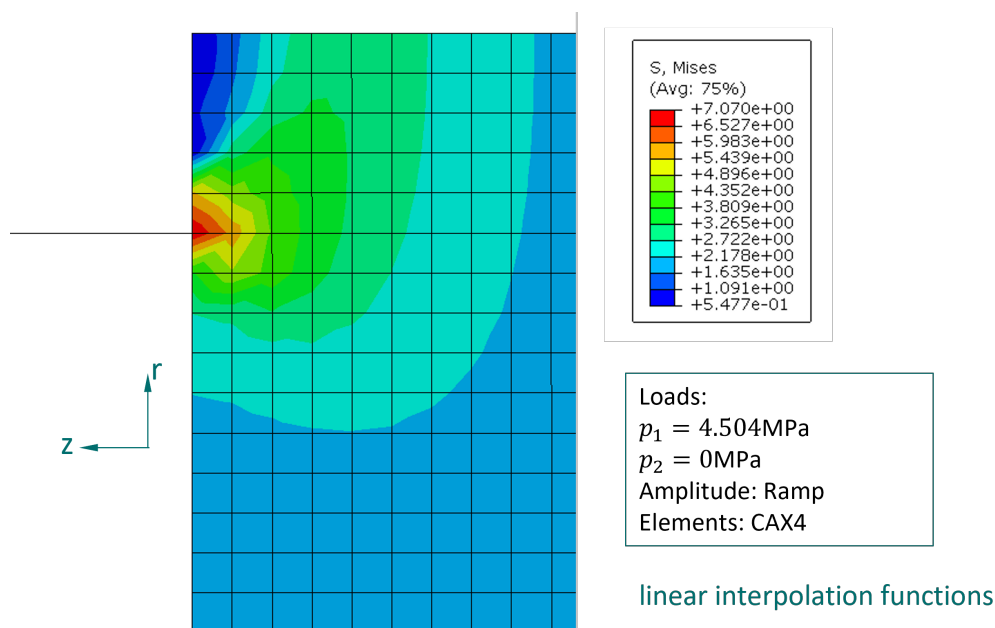


Figure 4.3: Stress field in the cylinder ring of the critical area

For a meaningful comparison of this model with 3D models, the stress fields are compared. The shape of the stress field and the corresponding maximum stress values are used as criteria for assessing the degree of agreement. For the selected element size, maximum von Mises stresses of 7.07MPa occur in the axisymmetric model.

4.1.3 Stress field in the uncut 3D ring

Symmetry is exploited for the 3D model of the cylinder ring, which allows to consider only a quarter of the cylinder ring (4.1 a). The rest is determined by the boundary conditions. The definition of the boundary conditions to take symmetry into account is done as shown in Figure 4.4. The boundary conditions allow radial displacements, but block displacements against areas where material is located. This enables a significant reduction in the number of elements and thus a significant reduction in computation time.

Figure 4.4 depicts the stress state in the uncut ring (see Figure 4.1 a). It is expected that the stress state equals the stress state in the axisymmetric model. The stress field in the area of the edge is qualitatively, but not quantitatively equal. The 3D model shows slightly larger maximum stress values than the axisymmetric model. The maximum Mises stress of the axisymmetric model differs from the uncut 3D-model by 3.5%. The area of the influenced stress field and the values of the stresses strongly depend on the used element size and element type.

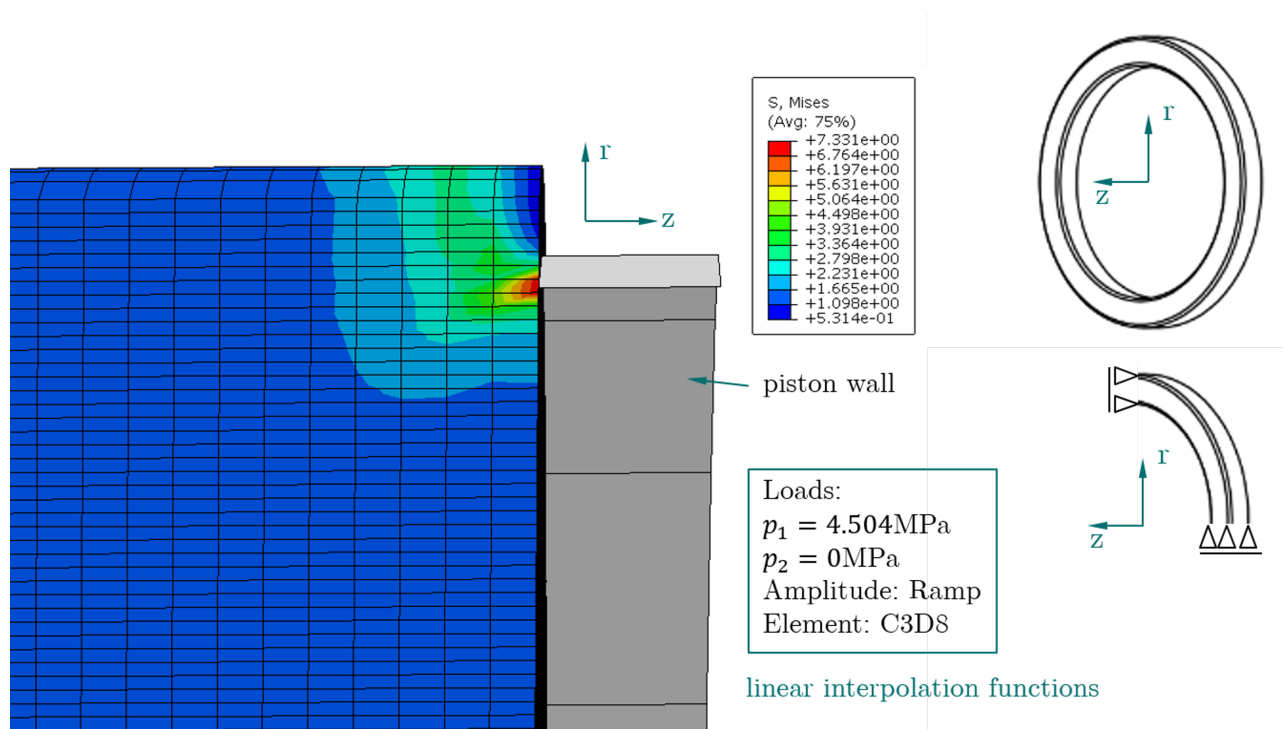


Figure 4.4: Stress field in the uncut 3D cylinder ring

4.1.4 Stress field in the cut 3D ring

Figure 4.5 and 4.6 show the stress states in the cut cylinder ring. Figure 4.5 depicts the stress state at the gap of the cylinder ring and Figure 4.6 shows the stress state of a cross section that is perpendicular to the gap plane. Due to the principle of Saint Venant the irregularities in the stress field due to the influence of the gap changes rapidly into the stress field of the uncut cylinder ring with increasing distance from the gap.

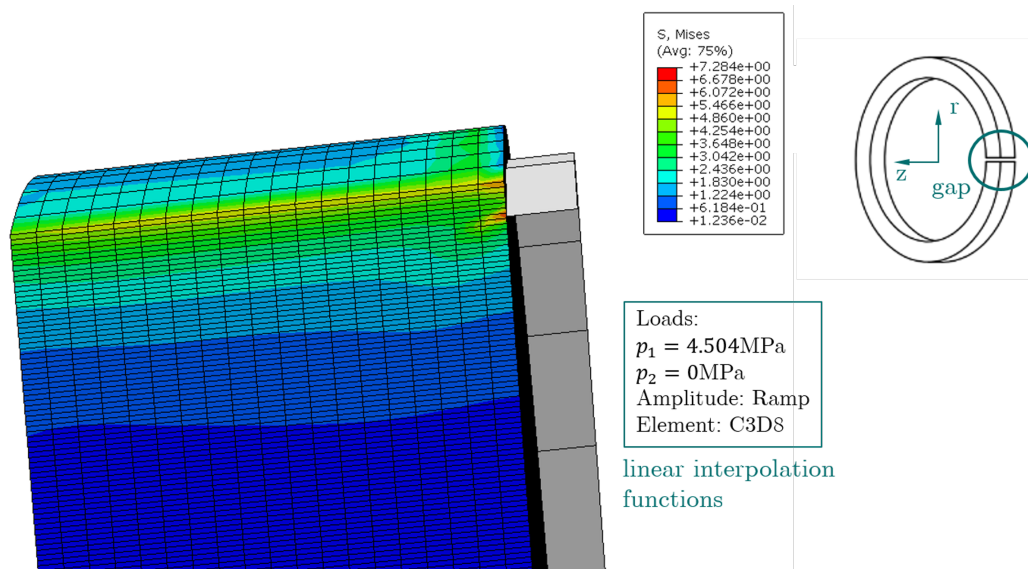


Figure 4.5: Stress field in the cut 3D cylinder ring at the gap

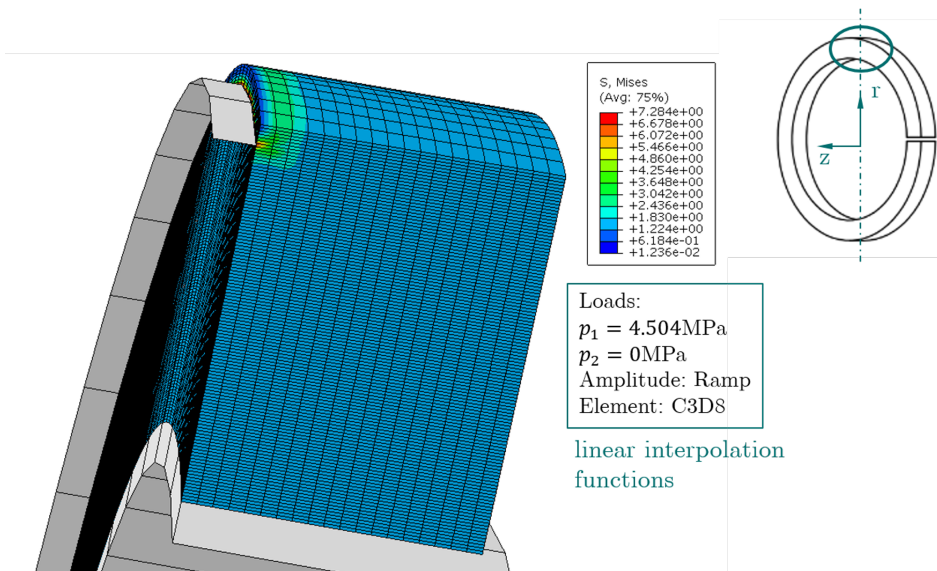


Figure 4.6: Stress field in the cut 3D cylinder ring at the marked cross section

4.1.5 Results of the comparison

The comparison of the stress states in the axially symmetric model and the uncut 3D model provides a great compatibility of the occurring stress values as well as the shape of the stress field. The difference in stress magnitude is around 3.5%. The differences are probably due to the different element dimensions.

The axially symmetrical model also delivers suitable values for the slotted ring. However, in the area of the slot, the stress field shows a different shape and deviating values. But these differences merge into the stress field of the uncut cylinder ring with increasing distance. In addition, the stress values at the slotted end are lower and thus less critical.

Only geometries a) and b) are compared (see Figure 4.1), however, the results are well-transferable to the other shapes of cylinder rings. Only for shape f) there are significant deviations due to the groove and the bores.

The use of an axisymmetric model is, therefore, permissible. Since the axisymmetric model requires significantly fewer elements for the same element dimensions than the spatial model, this also leads to a major reduction in simulation time.

4.2 Convergence study

At the contact point between the edge of the piston and the cylinder ring a stress singularity occurs in the cylinder ring. Due to this singularity, the stress values do not converge with increasing refinement of the mesh. Figure 4.7 shows the results of the convergence study. On the abscissa axis the edge length of the elements and on the ordinate axis the Mises stress is depicted. The stress values strongly increase while the element size decreases. Since the singularity is a non-physical effect, this position cannot be used to detect the creep strains. According to Saint-Venant's principle, however, these singularities of the field variable decay rapidly at some distance. Therefore, a few elements below the singularity a reliable evaluation can be performed.

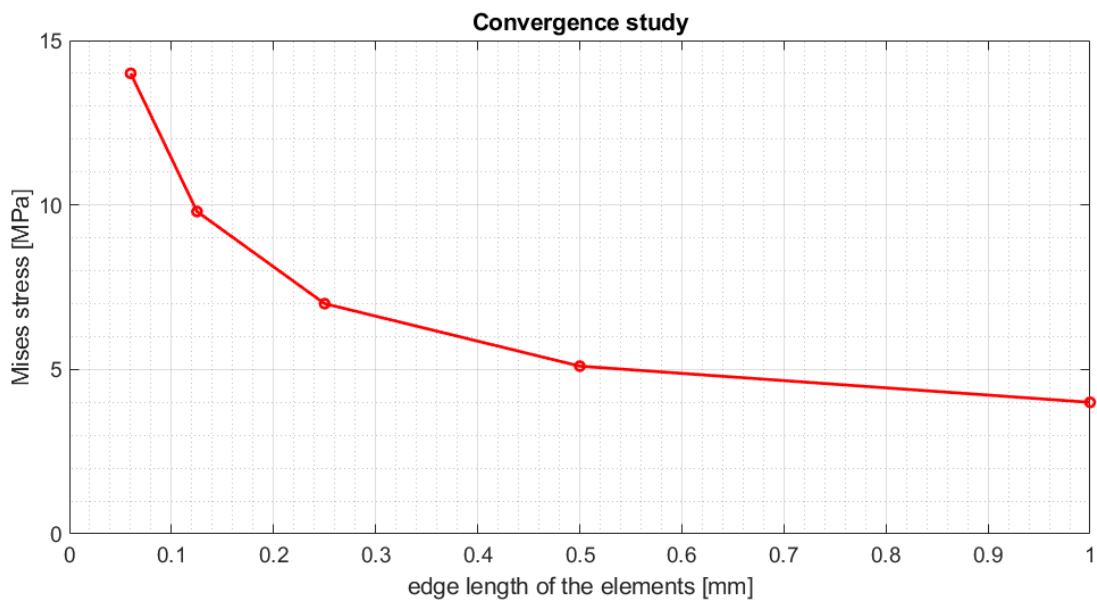


Figure 4.7: Results of the convergence study

To eliminate the undesirable singularity, the corner of the piston must be rounded. In addition, a submodel is created in order to resolve the stress values in the critical area very finely.

4.2.1 Principle of Saint Venant

In its original formulation Saint Venant's principle states that a complicated distribution of surface forces can be replaced by a statically equivalent group of concentrated forces. If they act in an area that is small in relation to the body dimensions, it causes the same stress and strain state as the distributed surface forces at a sufficient distance from the point of application [13] (p105-106).

So, the principle of Saint Venant states that the effects of local disturbances of the stress field remain locally limited. These local disturbances may have real physical causes such as stress concentrations at locations of geometric notches, or material notches such as pores. The local perturbation of the stress field decays rapidly with increasing distance.

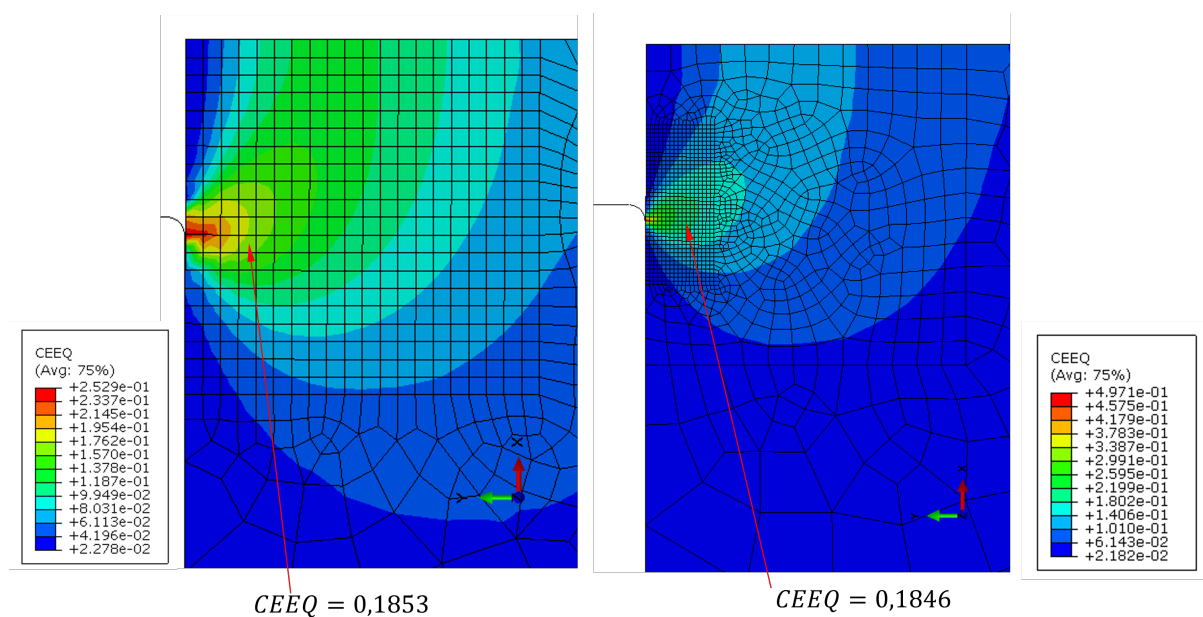


Figure 4.8: Application of Saint Venant's principle

Figure 4.8 shows the application of that principle. At some distance (approx. 0.2mm) from the singularity spot, the evaluation of the equivalent creep strain, and other field quantities yields similar values for two different mesh sizes. In the left simulation, an element size of 0.05mm is used and in the right simulation, an element size of 0.01mm is used. The created submodel for the critical area solves the problem with the occurring maximum of the stresses. The FE mesh is refined until no more changes in the stresses occur. These stresses are resolved by avoiding the singularity and lead to accurate results.

4.3 Calibration of the material model

The quality of a finite element analysis prediction depends on the quality of the input data including those of the material model. Only a well-calibrated material model allows accurate predictions of the resulting displacements and strains. The material parameters for the viscoelastic model (see chapter 2.3.3) used in this work are calibrated using two creep tests (see chapter 2.3.1).

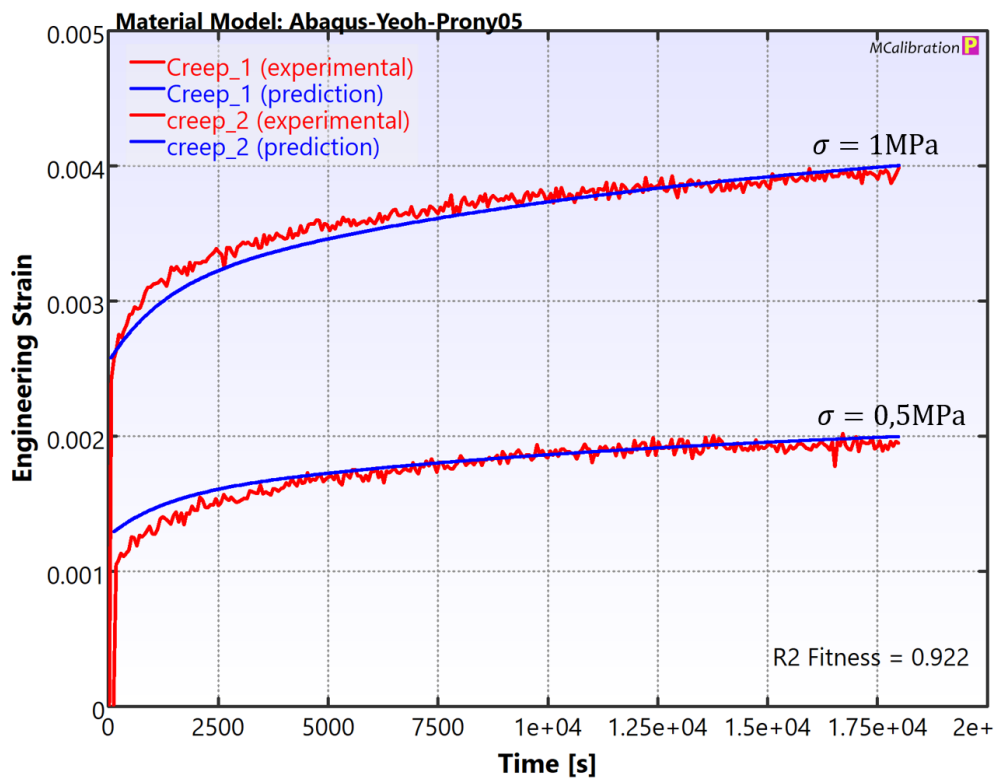


Figure 4.9: Results of material parameter calibration

Figure 4.9 represents the prediction of the material behaviour for the creep test. The calculation of the material parameters becomes difficult and is possible only in approximate form [6]. In the range of non-linear viscoelasticity the representation in closed form is prohibited. But it is possible to approximate this behaviour using a hyperelastic material model for the spontaneous elastic response and viscoelasticity for the time dependent behaviour. For large strains and deformations, a hyperelastic material model is required for the spontaneous elastic part, instead of a linear elastic material model. Thus, the non-linear relationship between stress and strain is taken into account. The calibrated material model shows a good approximation of the test data. For lower loads, the spontaneous elastic deformation is slightly overestimated, but the time-dependent deformation behaviour is well approximated.

4.3.1 Linear or nonlinear viscoelasticity

Isochronous stress-strain diagrams are necessary to precisely define the boundary between linear and non-linear viscoelasticity. These are not available for the cylindrical ring material. However, for some materials there are tabulated values for the stress at which the limit of the linear viscoelastic range is reached. This limit lies between 2.5 and 10MPa. Since the material at hand is rather more compliant, the limit of linear viscoelasticity will tend to be in the smaller stress range [6] (p214-216). Since stresses are expected to be higher, a non-linear viscoelastic material model is used in this thesis.

4.3.2 Stability of the hyperelastic model

Hyperelastic material models are not unconditionally stable. For this reason, the stability limits of the material model should be determined before use. This can be done with the Drucker's stability criterion [4] (p297).

$$\Delta\sigma_{ij}\Delta\varepsilon_{ij} \geq 0 \quad (4.1)$$

Where σ_{ij} is the stress tensor and ε_{ij} is the strain tensor. The reason for this is purely mathematical, as the Helmholtz free energy is always given as a polynomial function of the invariants of the (Green's) strain tensor. The function has to be convex. Every local minimum of a convex function corresponds to a global minimum. Depending on the order of the fitted polynomial, the convex region is left at a certain maximum or minimum strain. This marks the stability limit of the material model. The results of the stability test for the hyperelastic material model are shown in the table below.

Table 4.1: Stability limits of the hyperelastic material model.

Load mode	lower Limit [%]	upper limit [%]
uniaxial tension/compression	-53.09	90.00
biaxial tension/compression	-27.45	46.00
planar tension/compression	-44.75	81.00
simple shear		102.5
volumetric tension/compression	stable	stable

The lower and upper limit values are shown as linearised strains. The values are far from those expected. Thus, the material model is stable in the desired range of use.

4.3.3 Evaluation of the material model

Figure 4.10 shows the evaluation of the viscoelastic behaviour for a simple shear load. It is recognisable that the relaxation modulus and the creep compliance stabilise over time and reach a steady-state value. The normalised relaxation modulus reaches a stabilised equilibrium value of $\frac{E(t=\infty)}{E_0} = 0.555$, where $E(t = \infty)$ is the stabilized relaxation modulus and E_0 is the instantaneous Young's modulus. The normalised creep compliance reaches a stabilised value of $\frac{J(t=\infty)}{J_0} = 1.8$, where $J(t = \infty)$ is the stabilized creep compliance and J_0 is the instantaneous creep compliance. When the equilibrium state is reached, the strain is then greater than the spontaneous elastic strain by a factor of 1.8. The greatest changes in these two quantities occur in the first few seconds after the constant load is applied. Already after 60s, the normalised creep compliance has reached a value of 1.3.

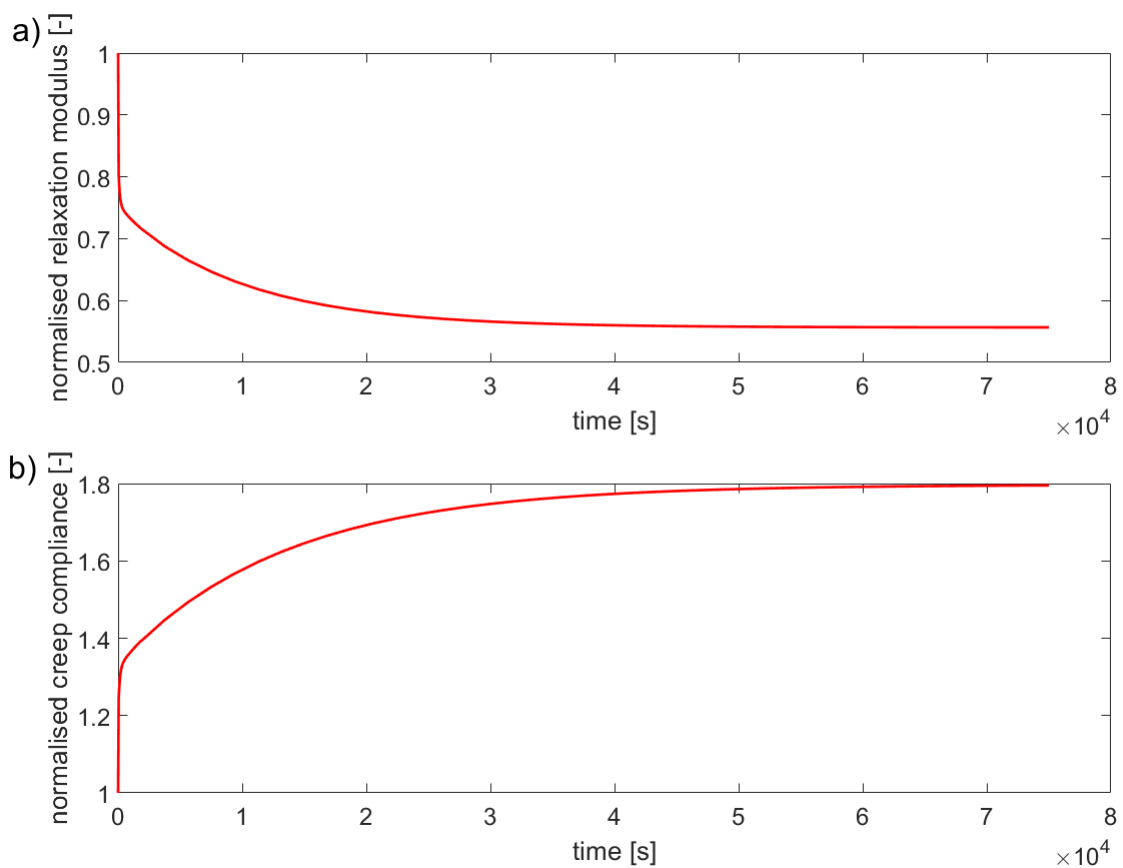


Figure 4.10: Evaluation of the viscoelastic material model for uniaxial load. a) Evolution of the normalised relaxation modulus, b) Evolution of the normalised creep compliance

4.4 Parameter study

The aim of the parameter study is to detect the influence of the different input parameters (Cylinder ring protrusion, temperature, crank shaft rotational speed and pressure difference) on the deformation of the cylinder ring. To evaluate the influence of these different parameters, the element with the element label 684 is used (see Figure 4.11).

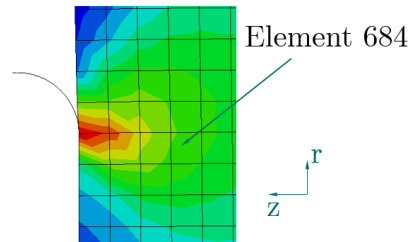


Figure 4.11: Location of element 684

4.4.1 Creep strain magnitude

An axisymmetric stress state applies in the region of interest. Figure 4.12 shows the normal components of the creep strain for the given input parameters as a function of time. All normal components of the creep strain tensor show a rapidly converging behaviour.

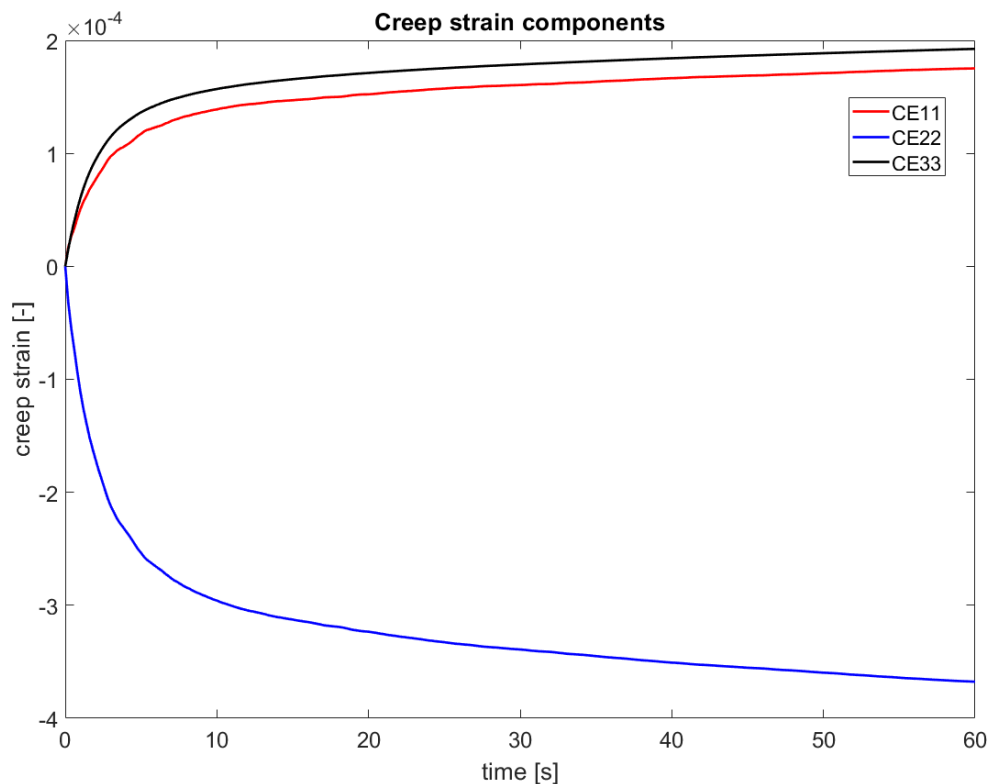


Figure 4.12: Normal components of the creep strain

where $CE11$ is the creep strain in radial direction ε_r , $CE22$ is the creep strain in axial direction ε_z and $CE33$ is the creep strain in tangential direction ε_φ . The figure shows that the first invariant of the strain tensor is zero. The first invariant follows from the trace of the strain tensor. Therefore, no volume dilation takes place.

To compare the creep strain with the (uniaxial) test data an equivalent value is necessary. In this work the creep-strain magnitude (CEMAG) is used as a scalar comparison value.

$$\varepsilon_{mag}^{(creep)} = \sqrt{\frac{2}{3} \varepsilon_{ij}^{(creep)} \varepsilon_{ij}^{(creep)}} \quad (4.2)$$

The following simulation results show a certain fluctuation of the creep strain. For this reason, the curves are smoothed (current average). The causes of this fluctuation are discussed in more detail in chapter 4.4.9.

4.4.2 Influence of the ring protrusion on the creep behaviour

Figure 4.13 shows the influence of the ring protrusion on the creep behaviour of the material. Three different protrusion values $t = 1\text{mm}$, 1.5mm and 2mm are investigated. Increasing the protrusion results in increased stresses, displacements and creep strains in the area of interest. This effect occurs due to increased bending and shear stresses in the cylinder ring. The creep strain increases with larger clearances between the piston and the cylinder wall. The cylinder ring protrusion shows a strong influence on the local creep behaviour of the material.

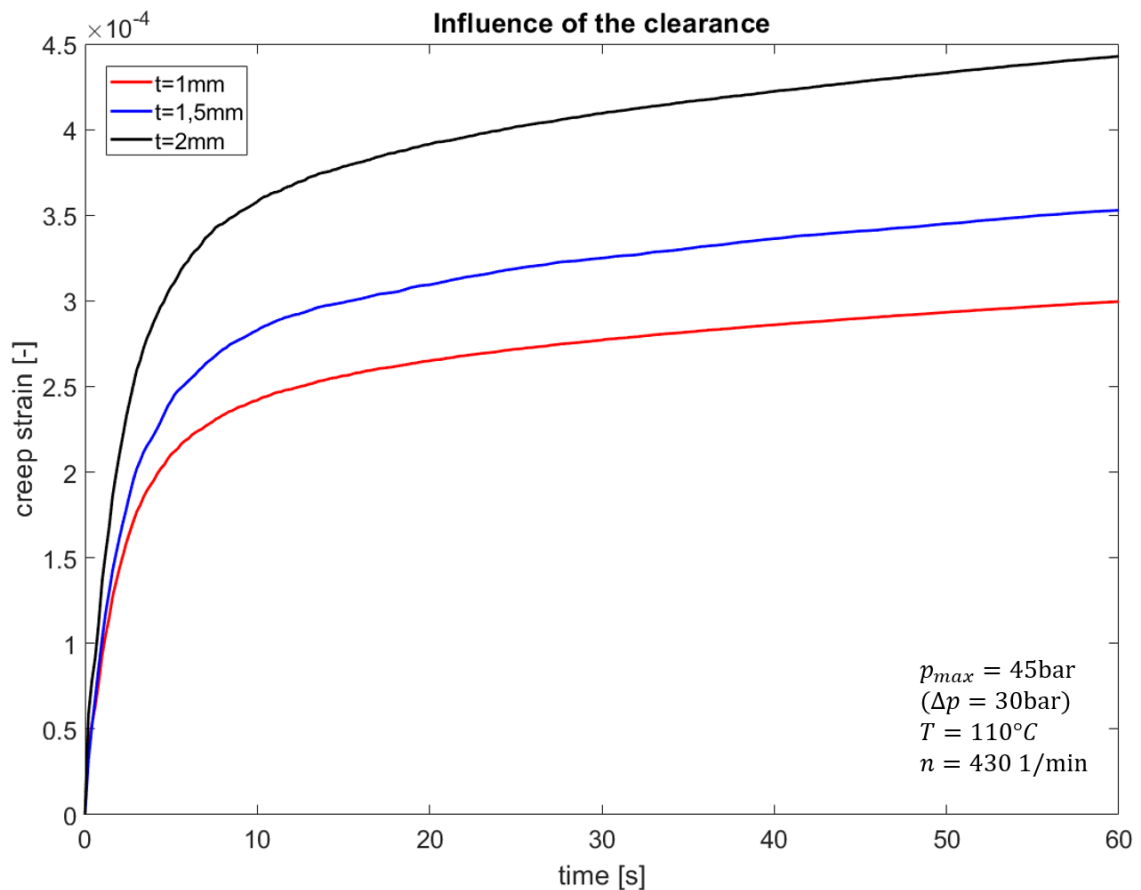


Figure 4.13: Influence of the ring protrusion t on the creep behaviour

The additional bending and shear stresses lead to greater creep of the cylinder ring material in the critical area. In the rest of the cylinder ring, sufficiently far from the bending edge, much smaller creep strains occur. In the rest of the cylinder ring, there is only a multiaxial compressive stress state with much smaller equivalent stresses.

4.4.3 Influence of the temperature on the creep behaviour

The creep behaviour of polymers is strongly temperature dependent. Increasing temperature results in a higher molecular movement of the polymer chains and in a reduction of the material stiffness. Figure 4.14 shows the influence of the temperature on the evolution of the creep strain for three different temperatures. The red curve shows the creep strain for a temperature of 110°C, the blue one for 140°C and the black curve for 80°C. The glass transition temperature of PTFE (Polytetrafluorethylene) lies in the range from 115°C to 130°C. The glass transition temperature of a polymer characterises the starting point of the main chain molecular movement. The molecular movement reduces the binding forces and leads to a reduction of the material stiffness. Thus, Figure 4.14 confirms the expectations that higher temperatures lead to higher creep strains.

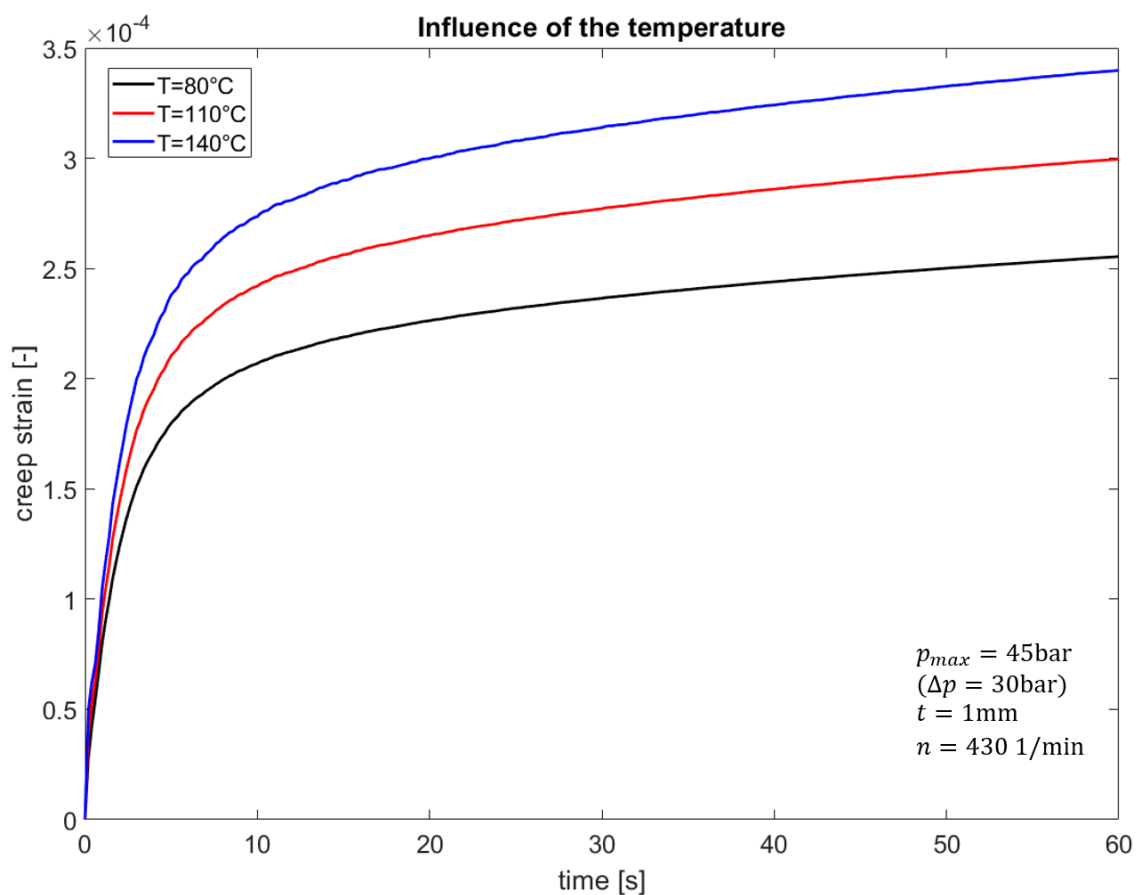


Figure 4.14: Influence of the temperature on creep behaviour

Higher temperatures not only lead to a reduction in material stiffness but also to reduced strength values, like the yield strength or the tensile strength.

4.4.4 Influence of the load rate on the creep behaviour

Below the yield strength, polymeric materials exhibit a time-independent (spontaneously elastic) and a time-dependent (viscoelastic) deformation. Due to the material trying to reach a thermodynamic more stable state, the macromolecular chains restructure. This process is time and temperature dependent. If the load rate is high, the material has no time to restructure the molecular order. Thus, the instantaneous elastic part of the material behaviour is more relevant than the time dependent viscoelastic part. Figure 4.15 depicts the influence of the load rate on the creep behaviour. Compared to pure creep loading, a significantly smaller creep strain occurs at higher speeds. Figure 4.15 also shows that the creep strain changes only slightly at higher speeds. At the same time, higher load rates also result in greater heating due to dissipative losses in the material itself.

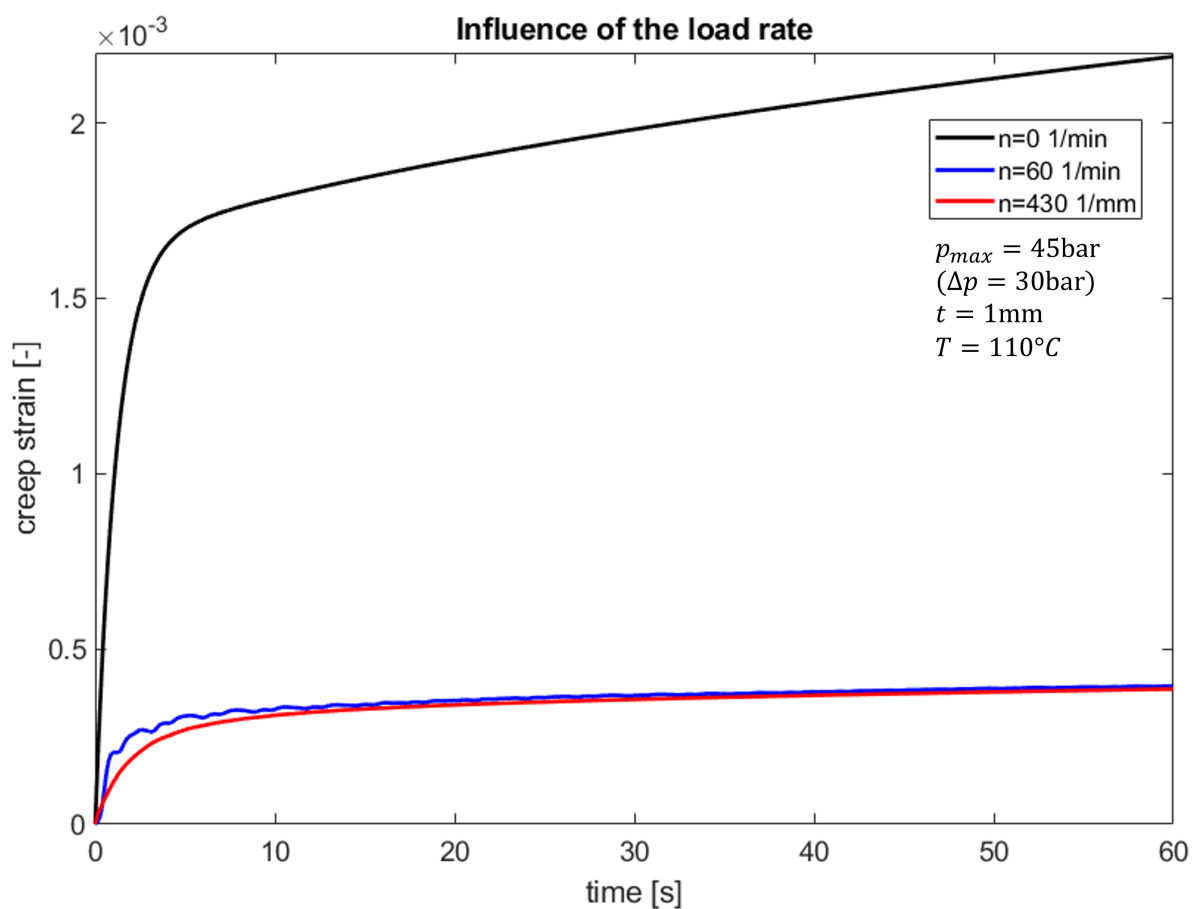


Figure 4.15: Influence of the load rate on the creep behaviour

The influence of heating due to hysteresis losses is not considered here. Its consideration requires the assumption of adiabatic conditions which is far from a corresponding quasi-stationary operating state. At higher load rates the quasi-stationary state occurs at higher temperatures and an increase in creep strain is expected.

4.4.5 Influence of the heating process through hysteresis losses

Figure 4.16 shows the heating of the highest loaded area due to hysteresis losses. It is visible that for a crankshaft speed of 430 revolutions per minute (frequency $f = 7.16\text{Hz}$), a clear heating of the cylinder ring occurs. Increasing the crankshaft speed and thus the frequency of the load rate causes a further increase in heating. The temperature does not saturate because the simulation is carried out under adiabatic conditions due to a lack of data for the convective heat transfer between the cylinder ring and the working fluid, the temperature of the working fluid, the temperatures of the cylinder wall and the piston, and the friction losses between the cylinder wall and the cylinder ring.

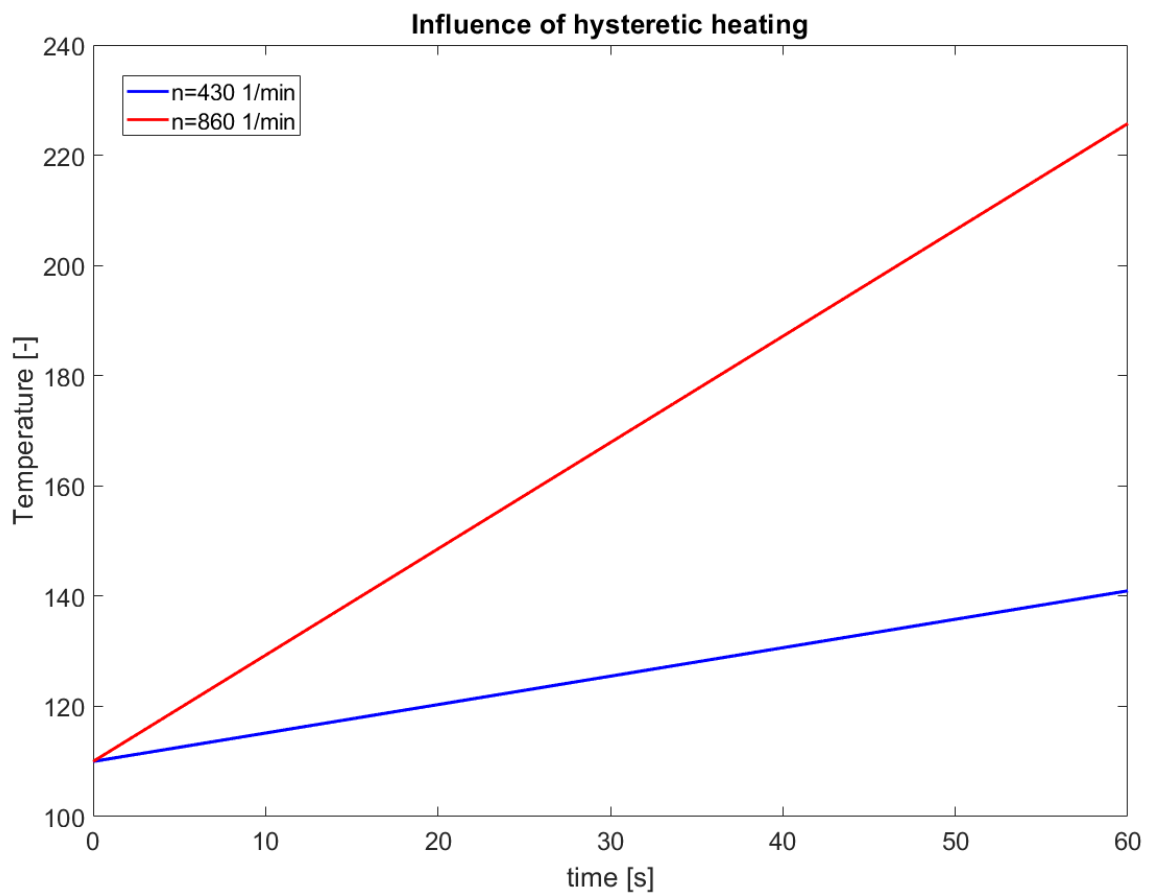


Figure 4.16: Adiabatic heating through hysteresis losses

The internal heat source is derived from the calculation in chapter 2.3.6 equation (2.62).

4.4.6 Influence of the load level on the creep behaviour

The pressure levels used are defined only for this master thesis. For these three load levels, the influence of the load on the creep behaviour of the polymer material is investigated. Figure 4.17 shows the results of these simulations. The occurring pressures have a strong influence on the creep behaviour of the material. An increase of the pressure level results in higher creep strains due to the increased stresses, in analogy to the elastic strain components. A doubling of the pressure level approximately leads to a doubling of the creep strain.

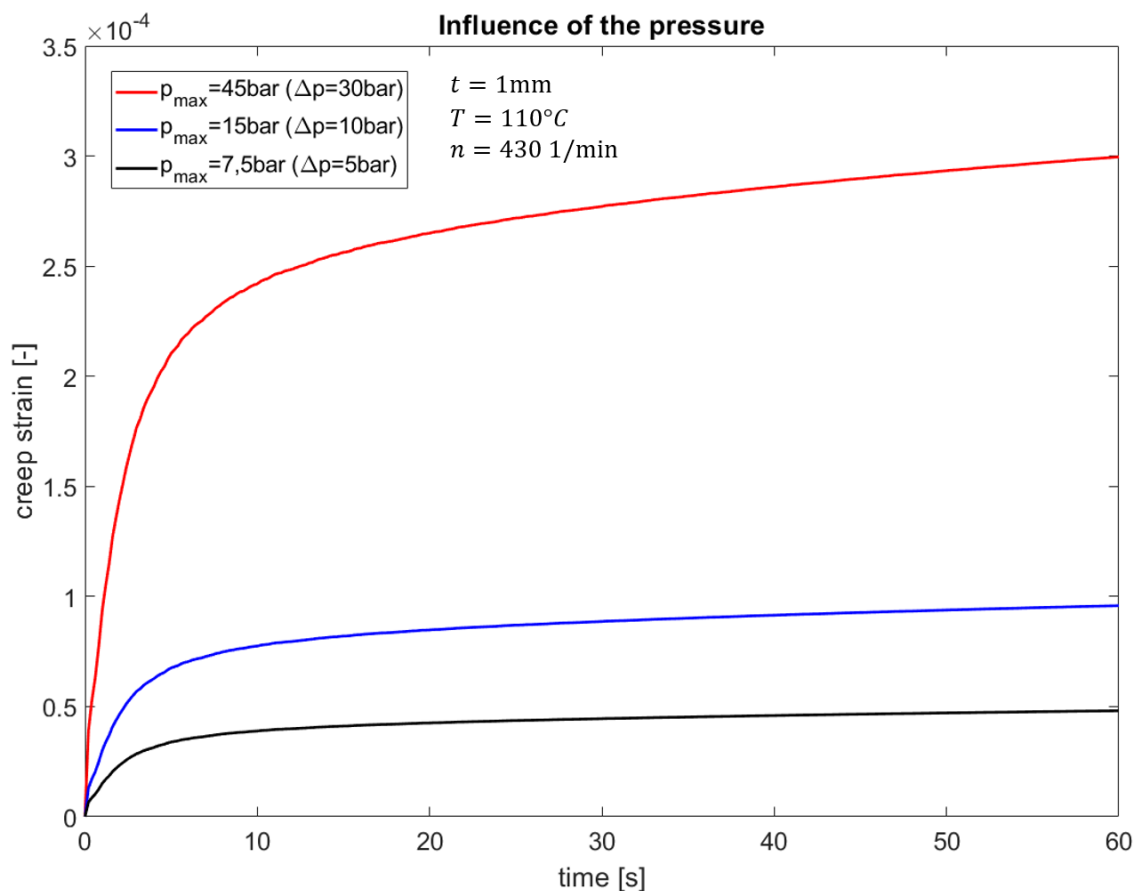


Figure 4.17: Influence of the applied load on the creep behaviour

As Figure 4.17 shows, at the highest load level (red curve), the creep strain converges quickly and increases only very slowly after a few seconds. At the lower pressure levels, the creep strain is significantly smaller. Higher pressure levels lead to a stronger slope of the creep curve.

4.4.7 Influence of the dimensions of the cylinder rings on creep

Since a variety of piston compressors with different sizes exist, the dimensions of the cylinder rings also vary. Therefore, the influence of the size of the cylinder rings on the creep behaviour is also examined within the scope of this work. Figure 4.18 shows that the dimensions of the cylinder ring only have a small impact on the creep behaviour under the same conditions. The smaller sizes ($d=100\text{mm}$ or $d=200\text{mm}$) show marginally larger creep strains than the larger sizes ($d=400\text{mm}$ or $d=800\text{mm}$).

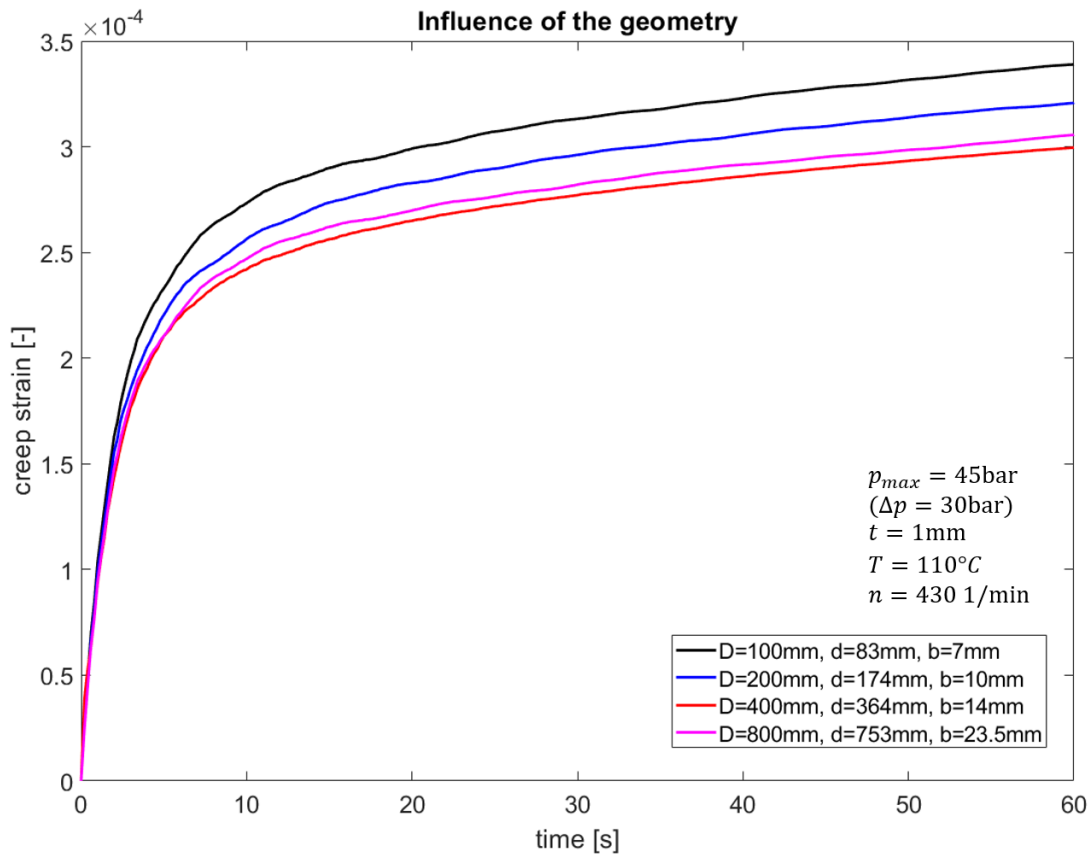


Figure 4.18: Influence of the dimensions of the cylinder rings on the creep behaviour

Larger differences in creep strain occur with the actual cylinder ring protrusions. Figure 4.19 shows the creep curves for the different cylinder ring sizes with the actual cylinder ring protrusions. Here, the creep strains increase with increasing size. This is due to higher stresses resulting from larger protrusions.

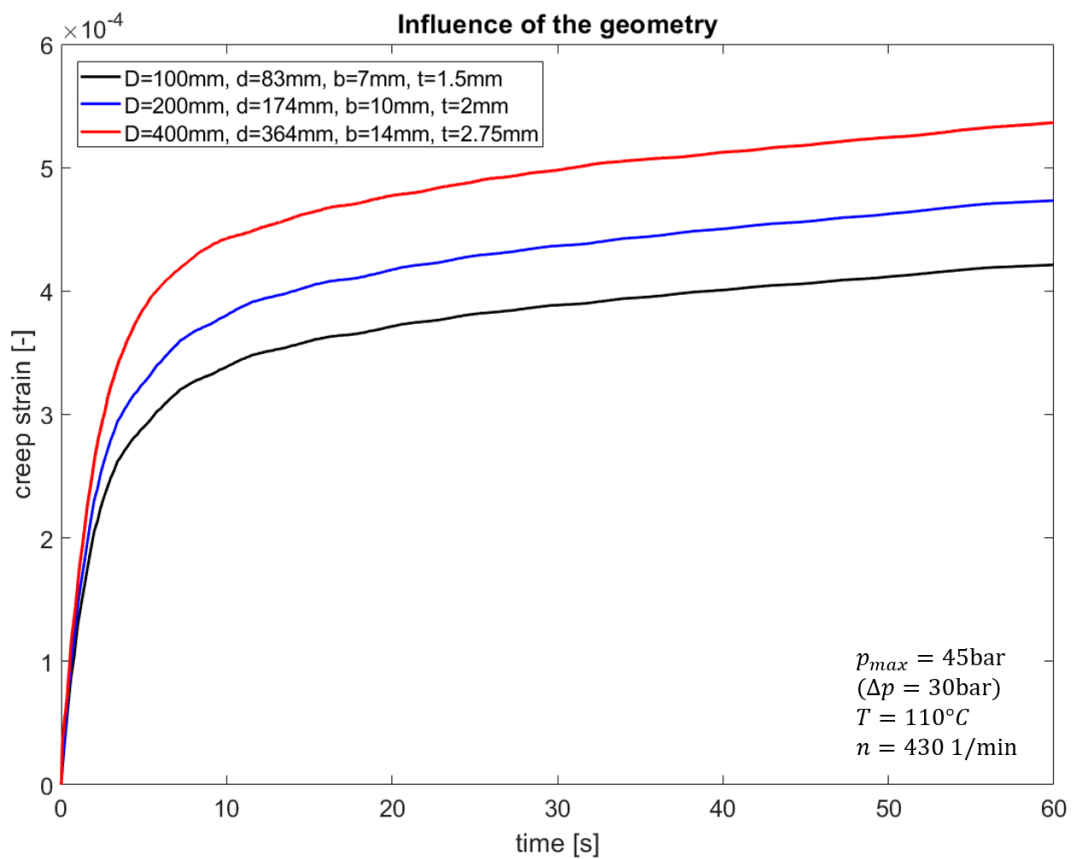


Figure 4.19: Influence of the dimensions with the actual cylinder ring protrusions

An interesting detail, concerning the series of parameter studies, is that the principal stress amplitudes always stay negative in the entire cylinder ring. However, if the dimensions vary towards smaller axial width b , positive stress amplitudes may also occur once the thickness drops below a minimum, i.e. the rings become too thin.

4.4.8 Influence of the material model

In principle, the question arises whether the non-linear viscoelastic material model is necessary, or whether a linear elastic material model would be sufficient to predict the influence of the different influencing variables. Figure 4.20 shows the results of a simulation carried out at the same load situation, first with a non-linear viscoelastic and then with a linear viscoelastic material model. As the results show, the nonlinear viscoelastic material model shows a greater creep strain after the same elapsed time. This is due to the fact that the nonlinear viscoelastic behaviour takes into account the dependence of the elastic constants on the load level $E = E(\sigma)$. The creep strain values differ by about 25%.

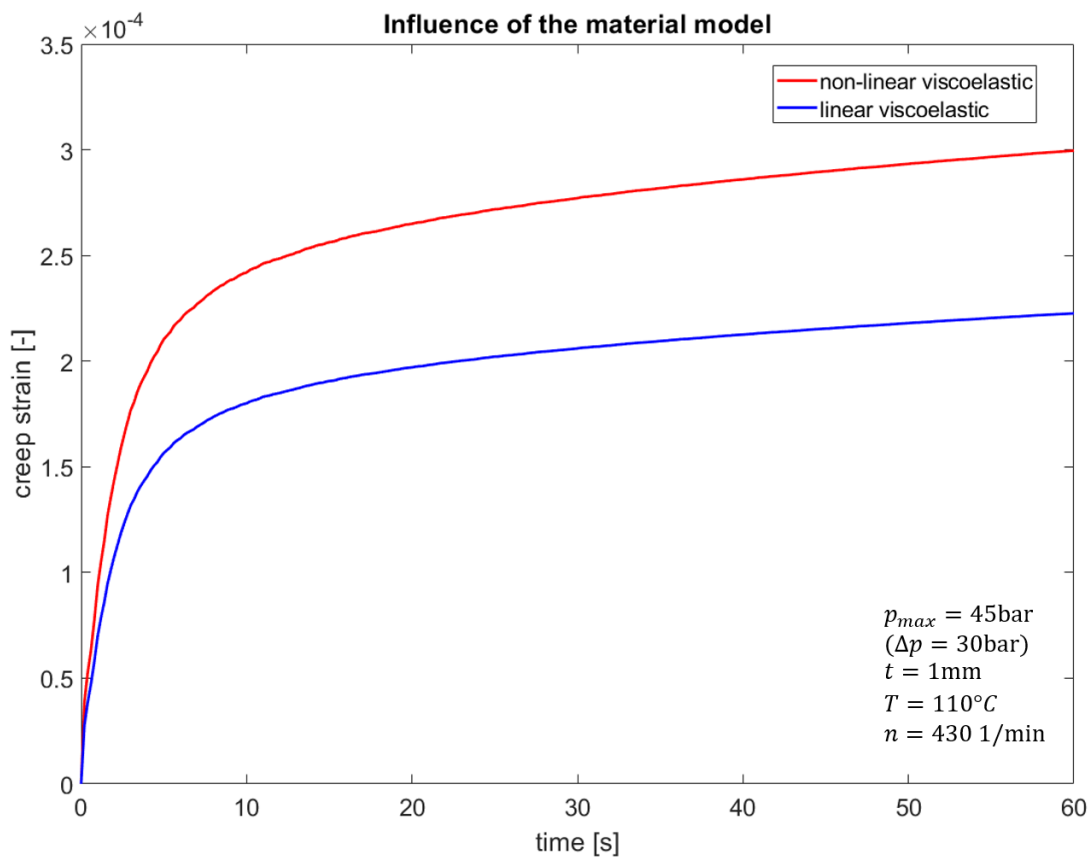


Figure 4.20: Influence of the selected material model

The creep strains that occur are very small for both material models. In principle, it would have been sufficient to carry out the parameter study using the linear viscoelastic material model. The resulting creep strains would be somewhat smaller. But the results of the influence of the different influencing variables would be very similar.

4.4.9 Fluctuation of the creep curves

The aim of this chapter is to determine whether the fluctuations of the creep curve have a numerical origin, or are due to a physical effect. Due to the fluctuation of the load amplitude, the creep strain also fluctuates in a certain range. As a result of creep at a constant stress amplitude, the hysteresis loop opens but moves towards larger strain values with increasing time until the creep behaviour stabilises.

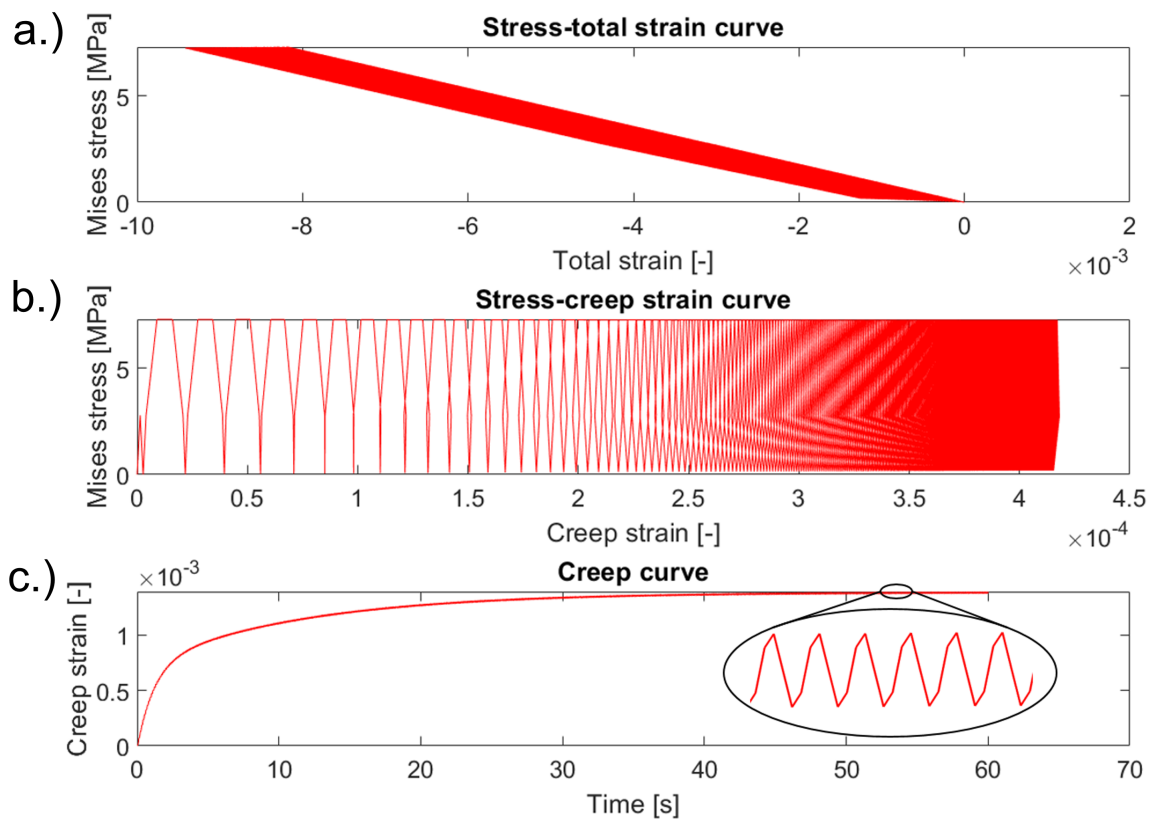


Figure 4.21: Simulation of a uniaxial cyclic creep test. a.) Stress-strain curve of the simulated cyclic creep test, b.) Stress-creep strain curve of the simulated cyclic creep test, c.) Creep curve of the simulated cyclic creep test

Figure 4.21 shows the stress-strain curve, the stress creep-strain curve and the creep curve of the material under cyclic loading by a sinusoidal pressure. In this simulation, a uniaxial stress state is present in the model of a specimen without any contact conditions. The creep strain stabilises quickly and reaches a steady-state value. During a load cycle the creep strain oscillates between a larger and a smaller value due to the constant change of the load level. The amplitude of the fluctuation initially increases but then stabilises. This results from a decrease in material stiffness or an increase in material compliance. The greater the magnitude of the applied pressure, the greater the fluctuation of the creep curve.

Figure 4.22 illustrates the creep curves for two different pressure signals. These simulations, performed directly for the cylinder ring model, take into account the stress state in the critical area (element label 684) and also the contact conditions. The red line represents the results from a pressure signal calculated by HOERBIGER Wien GmbH. By contrast the blue line results from a synthetically generated signal (trapezoidal signal). The amplitude values of the applied pressures are equal for both simulations.

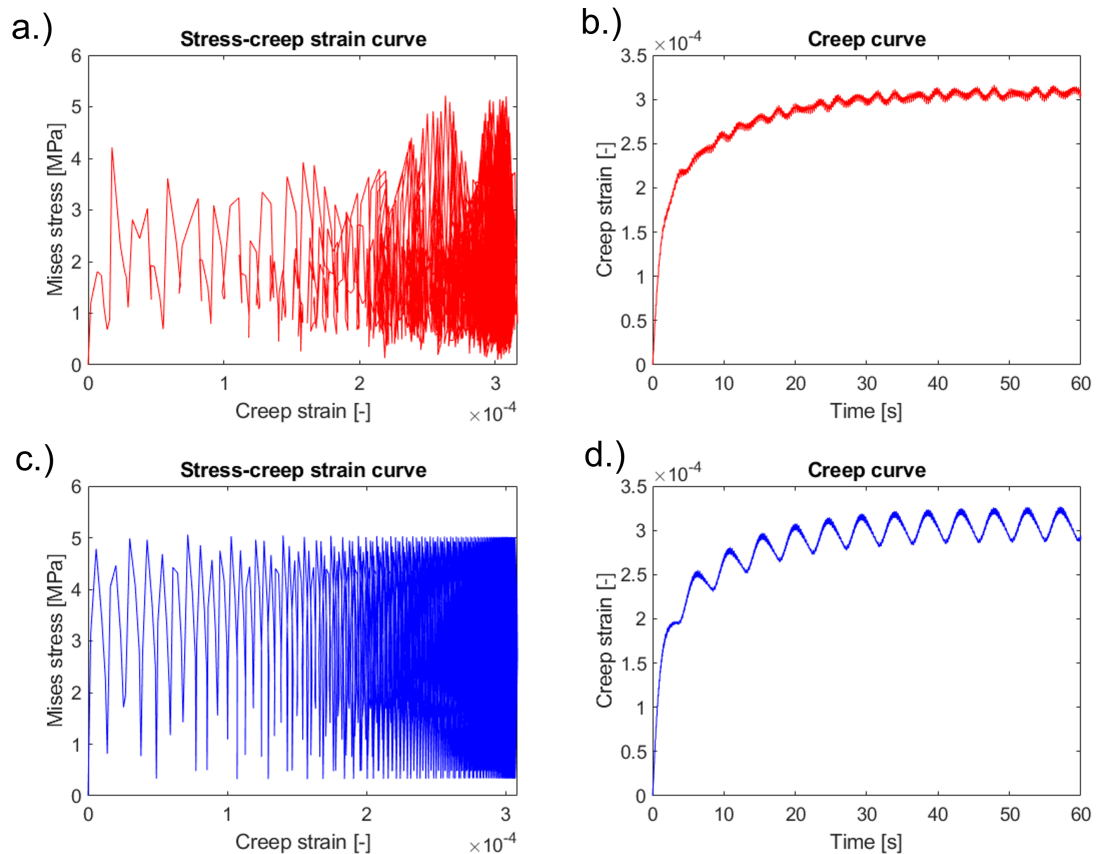


Figure 4.22: Influence of the form of the pressure signal to fluctuation of the base curve
 a.) Stress vs. creep strain for the load signal fitted from the measurement data
 b.) Creep curve for the load signal fitted from the measurement data
 c.) Stress vs. creep strain for the synthetic load signal
 d.) Creep curve for the synthetic load signal

In addition to the fluctuation due to the periodic change in load (Figure 4.21), an additional but significantly stronger fluctuation occurs with these curves. The blue curve shows a stronger fluctuation of the creep curve around the base curve than the red curve. Nevertheless, both curves fluctuate around the same stabilised value. These fluctuations disappear for single-acting compressors. It is not clear whether the fluctuations result from a numerical artefact. A material-physical cause is rather to be excluded since cyclic hardening and softening does occur, but with the frequency of the load and not with a significantly lower frequency than the load frequency (see Fig. 4.21). These fluctuations therefore probably results from the combination of the pressure profile and the contact condition which includes the separation and rejoining of the contact surfaces.

4.4.10 Conclusion of the parameter study

The creep behaviour stabilises rather quickly for all different parameters. This agrees with the experiences of HOERBIGER Wien GmbH. According to HOERBIGER Wien GmbH permanent deformations are not expected even after extensive operating times. The maximum creep strain values do not occur homogeneously in the entire cylinder ring, but only very locally in the highest loaded area. The creep strains that occur in the rest of the cylinder ring are significantly smaller. The failure of the cylinder rings, in practical use, is hence not a result of excessive deformation, but rather a result of the occurring fatigue load. A strong influencing factor on the creep behaviour of the cylinder ring is the load level. An increase in load is associated with a sharp increase in creep strain, see chapter 4.4.6. An increase in the clearance between the cylinder wall and the piston also causes an increase in the creep strain, as the stresses rise with increasing ring protrusion.

The influence of the loading rate on the creep strain is not accurately predictable, due to the lack of data. This requires a precise knowledge of the quasi-stationary temperature field inside the cylinder ring. In principle, a higher load rate leads to a decrease in creep strain, as the material has too little time for creep processes to take place. But at the same time energy is dissipated. Since the dissipated energy increases with an increasing loading rate, the quasi-stationary state will occur at higher temperatures, in turn leading to higher creep strains.

Due to the insignificant creep strain magnitudes in the range of 0.05%, viscoelastic deformation will not be an issue for the long time behaviour and durability of the cylinder ring. By contrast, the life-time will be determined by a classical stress-based fatigue criterion.

Since the creep strain values that occur are negligibly small, it is not necessary to use the viscoelastic material model in further detail and a linear elastic material model can be used instead.

4.5 Criterion for the maximum possible ring protrusion

The primary task of this thesis is to find the maximum possible clearance between the cylinder wall and the piston for double acting piston compressors. An increasing clearance reduces the wear between the metallic components (cylinder wall and piston) but increases the mechanical load on the polymer based cylinder ring. A small clearance reduces the loads on the cylinder ring but results in larger wear of the piston and the cylinder wall. A suitable design criterion is required for finding the optimum cylinder ring protrusion.

4.5.1 Dimensioning criterion

A large variety of size criteria exists for polymer materials. They are split into three main categories [6].

- Energy based criteria (Rainer-Weissenberg criterion,...)
- Strain based criteria (maximum strain criterion,...)
- Stress based criteria (Mises criterion, maximum stress criterion, fatigue,...)

Mascarenhas [14] recommends the maximum stress criterion for ductile polymers under cyclic load and a linear elastic analysis. He furthermore recommends the maximum strain criterion for ductile materials under low strain rates and a non linear elastic analysis. Examples for other criteria and their advantages, as well as disadvantages are summarized in the following papers [2], [5],[16], [9], [17], [12].

According to Mascarenhas [14], a linear elastic material law is used to determine the stress amplitude and the average stress. Many polymeric materials have a higher compressive yield strength than tensile yield strength. The influence of the yield strength ratio is considered in extended failure criteria, such as the conical failure criterion. According to this criterion, a multiaxial compressive stress is significantly better tolerated than a multiaxial tensile stress [6].

4.5.2 High cycle fatigue

Materials may fail under cyclic loading due to fatigue. During fatigue loading, cracks appear in the component as the number of load cycles increases. They grow over time until a residual fracture occurs. The shape of the fatigue strength curve (SN-curve) in the operational strength area is similar for all material groups. While metals with a cubic space-centred ferrite lattice show a pronounced fatigue strength in the region above $N_A = 2 \cdot 10^6$ load cycles, the fatigue strength line keeps declining for polymer materials below $N_A = 2 \cdot 10^6$. Figure 4.23 shows a representation of a fatigue curve for a polymer material.

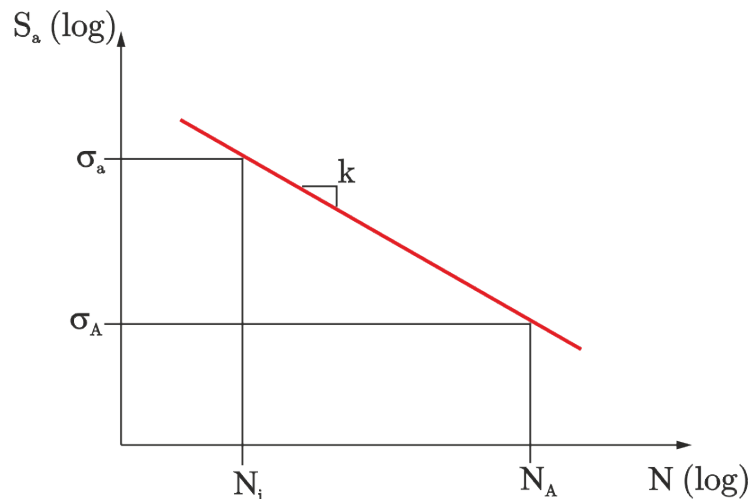


Figure 4.23: Fatigue strength curve for a polymer material

The number of sustained load cycles at a given stress amplitude level is determined using the fatigue curve (Figure 4.23)

$$k = \frac{\log(N_A) - \log(N_i)}{\log(\sigma_a) - \log(\sigma_A)} \quad (4.3)$$

where k is the slope of the fatigue strength curve, N_A is the number of cycles at fatigue strength σ_A , σ_a is the permissible stress amplitude at a number of cycles N_i . Using the laws of logarithms, this term can be rewritten as

$$\left(\frac{\sigma_a}{\sigma_A}\right)^k = \frac{N_A}{N_i} \quad (4.4)$$

All stress-related fatigue criteria require the fatigue strength curve. They are determined based on standardised test rods and under standardised test conditions. Local concepts, on the other hand, require the component's fatigue strength curve, which is calculated with the help of further input variables such as the mean stress sensitivity and the local geometry by means of FEM. Due to a complex stress state in the critical area of the cylinder ring, a local concept is recommended for the problem at hand. The following formula represents the stress ratio R

$$R = \frac{\sigma_{min}}{\sigma_{max}} \quad (4.5)$$

where σ_{min} corresponds to the minimum stress and σ_{max} to the maximum stress during a load cycle.

4.5.3 Synthetic material fatigue curves

Since no fatigue strength data exist for the cylinder ring material, they are estimated according to [19]. Which states that, the stress at a total non-linear strain of 1% is used as yield point. Since no data is available for the fatigue strength, it is set for a stress ratio $R = -1$ according to an approximation which is typically used for metallic materials. In contrast to metallic materials, however, the yield strength, not the tensile strength is used to ensure a greater safety factor.

$$\sigma_w = 0,35R_{p1} \quad (4.6)$$

where σ_w is the alternating strength and R_{p1} is the stress value at 1% non-linear strain. The consideration of the mean stress sensitivity follows from the analogy to the FKM guideline. The FKM guideline recommends different slopes of the curve in the Haigh diagram for metallic materials depending on the medium stress ratio. However, different slopes are not considered for polymeric materials. Solely the Goodman line (red line shown in Figure 4.24), is used for the entire range. The Goodman line represents the dependence of the tolerable stress amplitude on the mean stress. As shown in figure 4.24, the tolerable stress amplitude increases with decreasing mean stress. Furthermore, medium stresses in the compression range allow higher stress amplitudes than in the tension range. Hence, the mean stress sensitivity M is

$$M = \frac{\sigma_w}{R_{p1}} = 0.35 \quad (4.7)$$

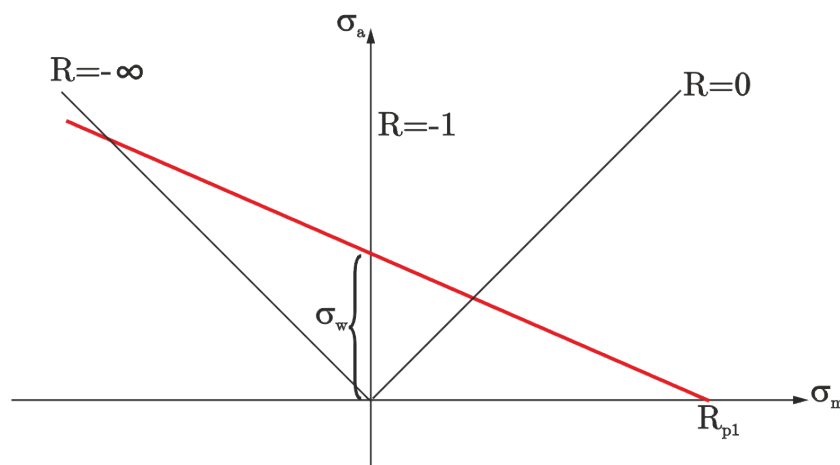


Figure 4.24: Influence of the mean stress to permissible stress amplitude

Using the stress sensitivity M a corresponding influence factor K_M can be calculated [19]:

$$K_M = \frac{1}{1 + M \frac{\sigma_m}{\sigma_a}} \quad (4.8)$$

The fatigue strength σ_A follows from the multiplicative connection of the alternating strength σ_w with the influence factor for the mean stress sensitivity K_M [19].

$$\sigma_A = \sigma_w K_M \quad (4.9)$$

The average stress as well as the stress amplitude result from the FE simulation. The slope of the fatigue curve is calculated by setting $\sigma_A = R_{p1}$, $N_i = 1$ and $\sigma_A = \sigma_w$.

$$k = \log(N_A) \frac{\sigma_w}{R_{p1}} \quad (4.10)$$

Figure 4.25 shows the synthetically generated material fatigue curves for three different stress ratios. The blue curve represents the fatigue strength under purely alternating stress. The red curve shows the fatigue strength under compressive pulsating stress, whereas the black one shows the fatigue strength under pure tensile pulsating stress.

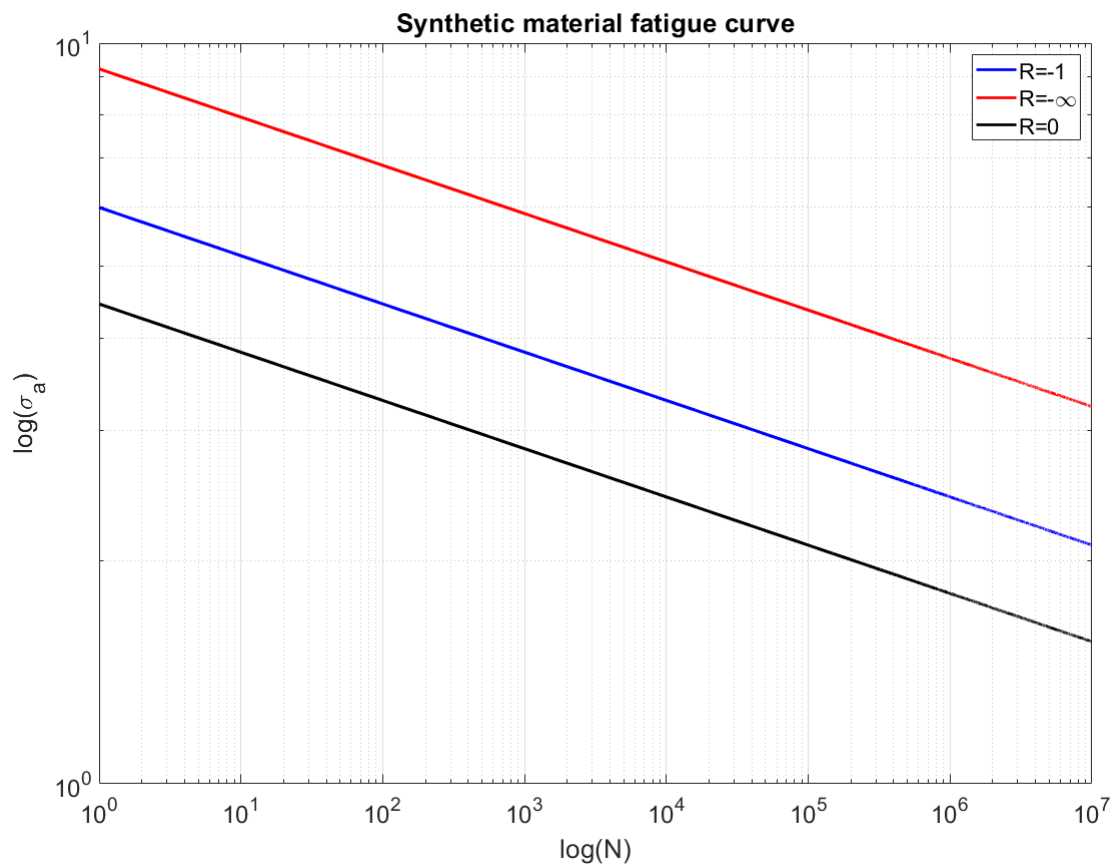


Figure 4.25: Synthetically generated material fatigue curve for three stress ratios

As Figure 4.25 shows, a compressive pulsating load is more favourable in terms of fatigue strength behaviour than a tensile pulsating load, because cracks grow much faster under tensile load.

4.5.4 Synthetic component fatigue curve

For local stress concepts, the use of the material fatigue curve is not advisable. Instead, here the component fatigue curve will be used to assess the fatigue behaviour. By means of the finite element method, influencing factors such as the strength-increasing influence due to the local stress gradient can be taken into account. Figure 4.26 shows the determination of the component fatigue line as performed in this master thesis. The approximation formulas (4.6) to (4.12) are used to determine the material fatigue line. The local stresses are determined with the help of the FE simulation. The stress gradients are determined in post-processing. Equations (4.12) and (4.14) as well as the material fatigue curve are then used to calculate the component fatigue lines.

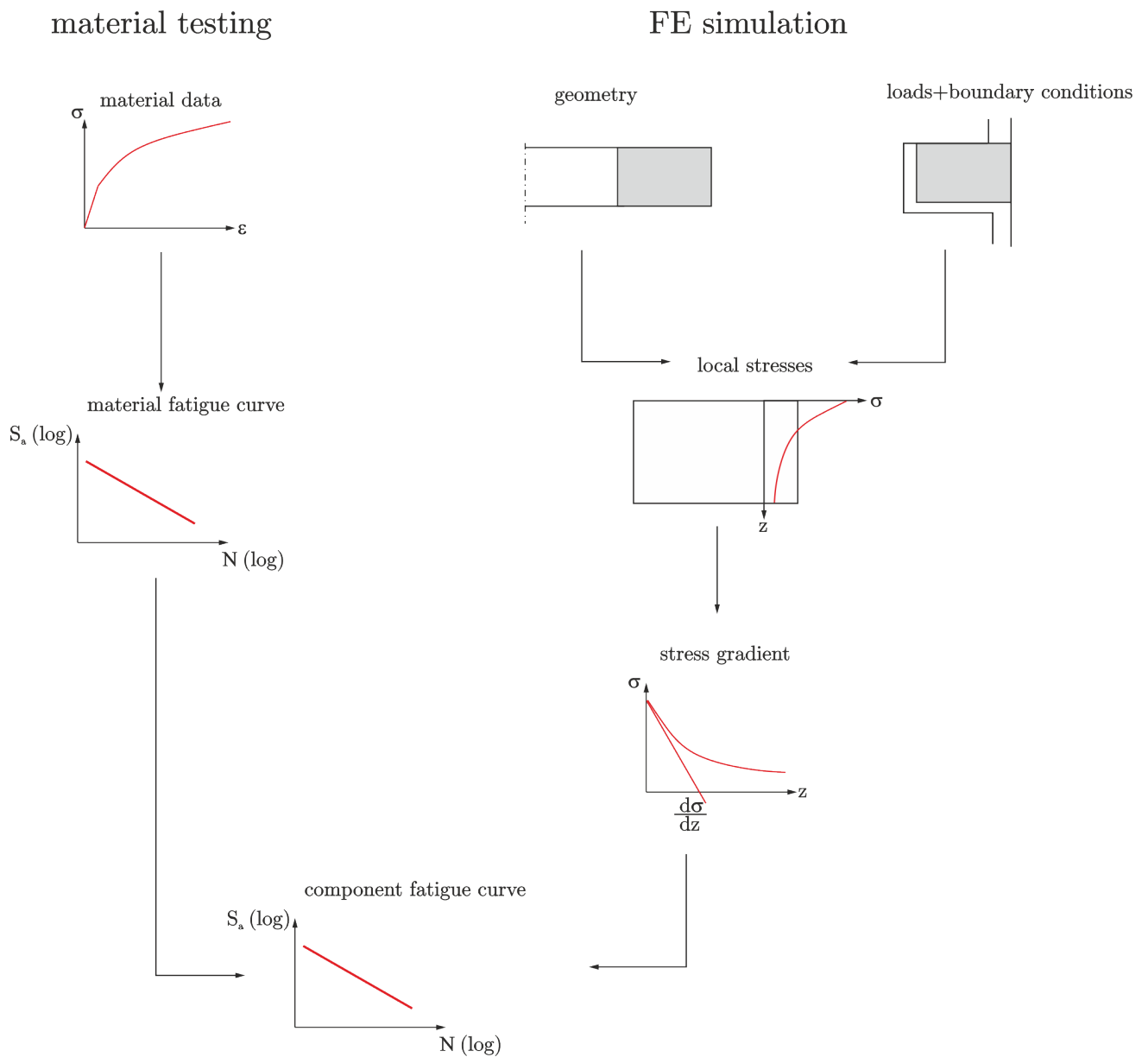


Figure 4.26: Determination of the component fatigue curve by using local concepts

Various other factors influence the component fatigue curve, such as the distribution of the filler or statistical effects. However, these factors are not accounted for in this work out of scope. The relative stress gradient χ is

$$\chi = \frac{1}{\sigma_{max}} \frac{d\sigma}{dx} \quad (4.11)$$

where $\frac{d\sigma}{dx}$ is the stress gradient. The fatigue strength increasing influence of the stress gradient is then estimated with the relative stress gradient according to Eichlseder [7].

$$\sigma_A = \sigma_{zdw} \left[1 + \left(\frac{\sigma_{bw}}{\sigma_{zw}} - 1 \right) \left(\frac{\chi}{2/b} \right)^{K_D} \right] \quad (4.12)$$

The ratio of the fatigue strength in bending to the fatigue strength in tension σ_{bw}/σ_{zw} is estimated using the values for metallic materials. For steels, this ratio is in the range between 1.06 and 1.15. For cast iron, it lies in the range of 1.4 to 1.45. As a conservative estimate a small value of 1.115 is chosen. The width b of the test specimen is taken from the corresponding standard (10mm). For the exponent K_D the value is estimated as 0.3, i.e the same as for steels. Figure 4.27 shows the synthetic component fatigue curve for the highest loaded area of the cylinder ring.

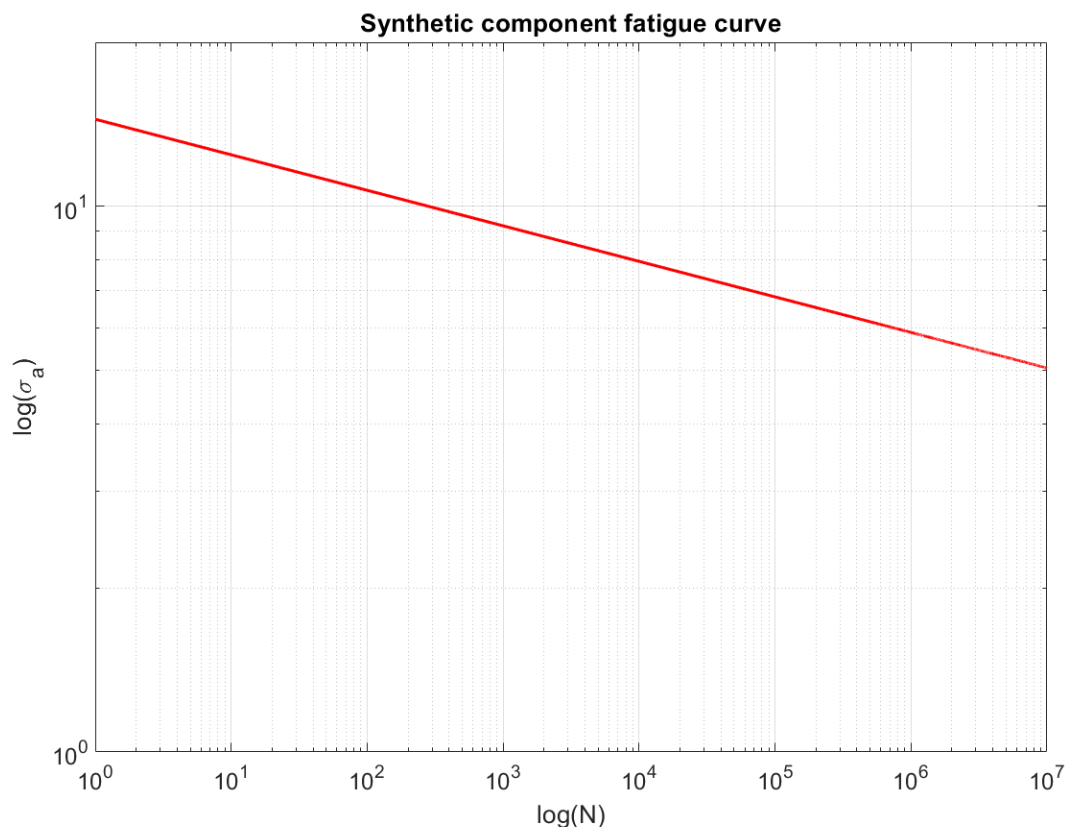


Figure 4.27: Synthetically generated component fatigue curve in the most critical area

In Table 4.2, the most important data for generating the synthetic fatigue curves and the results are summarised:

Table 4.2: Input parameters and results for generation of synthetic fatigue curves

Meaning	Formula symbol	value
Tensile yield strength	R_{p1}	6.0MPa
Yield point ratio	m	2.0
Ratio of the alternating strengths	σ_{bw}/σ_{zw}	1.115
Width of a tensile test rod	b	10mm
Fatigue exponent	K_D	0.3
Pressure yield strength	R_{d1}	12.0MPa
Alternating strength	σ_w	2.45MPa
Stress sensitivity	M	0.35
Corresponding factor for stress sensitivity	K_M	1.538
Referred stress gradient	χ	40.50 1/m
fatigue strength	σ_A	5 MPa

Figure 4.28 shows the influence of the local stress gradient on the component fatigue curve. It is clearly visible that a high stress gradient leads to a significant increase in the fatigue strength of the considered area in the component. Structural detail 1 is located directly in the most highly stressed area. While structural detail 2 is sufficiently far away from it. In the simulation results shown, red means high stresses while blue means low stresses. The gradation from red to dark blue indicates decreasing stresses.

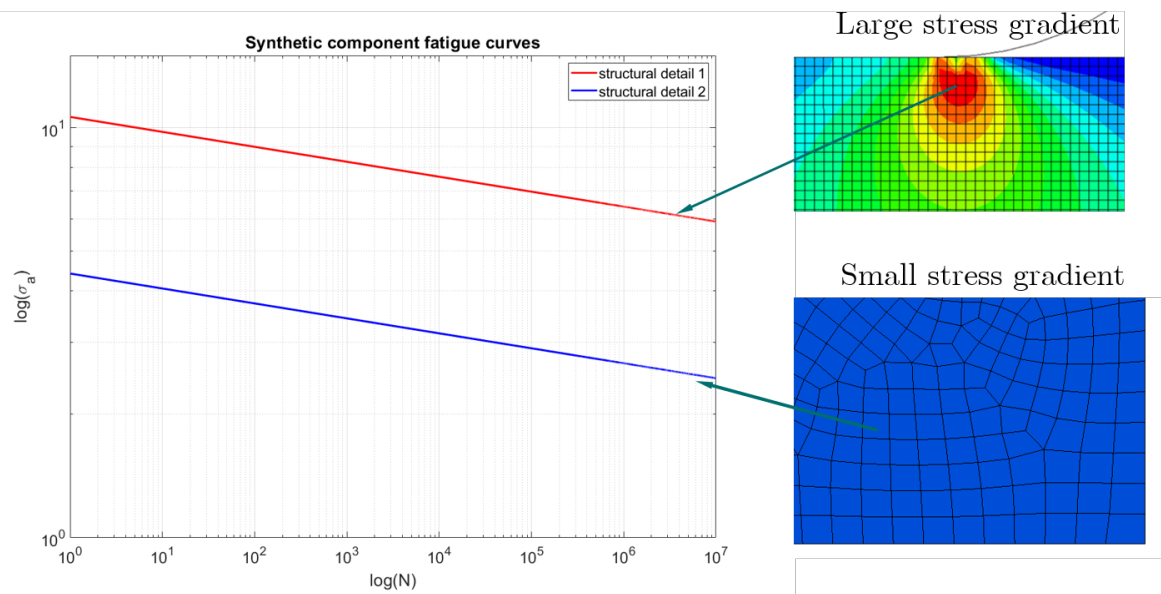


Figure 4.28: Influence of the local stress gradient on component fatigue curve

Figure 4.29 illustrates the stress gradient at the highest loaded point of the cylinder ring. In contrast to the parameter study, here the maximum stress always occurs in a different element, as the element numbering changes when the protrusion becomes larger and the submodel moves with it. The stress gradient corresponds to the instantaneous slope of the stress curve in axial direction. For the stress gradient concept, the stress gradient at the most critical point is evaluated.

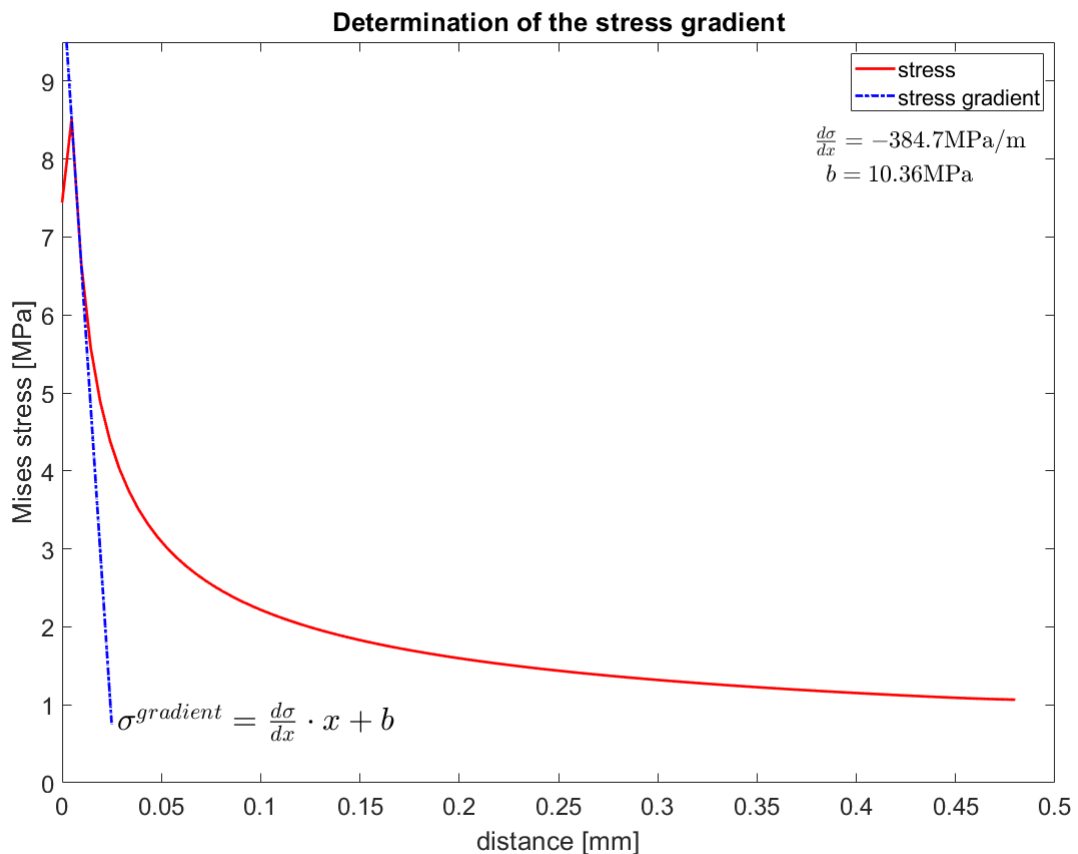


Figure 4.29: Determination of the stress gradient

For numerically determining the stress gradient, the differential quotient is replaced by the difference quotient.

$$\frac{d\sigma}{dx} \approx \frac{\Delta\sigma}{\Delta x} \quad (4.13)$$

Thus the relative stress gradient becomes

$$\chi \approx \frac{1}{\sigma_{max}} \frac{\Delta\sigma}{\Delta x} \quad (4.14)$$

4.5.5 Degree of utilisation

The degree of utilisation helps to evaluate the maximum possible clearance between the cylinder wall and the piston. The degree of utilisation is a dimensionless quantity which expresses to what extent the material's strength reserves are exploited. The degree of utilisation corresponds to the ratio of the stress that occurs to the maximum permissible stress. In the case of cyclic loading, proof must be provided for both the static and the dynamic degree of utilisation. The static degree of utilisation $a^{(stat)}$ is defined as the ratio of the maximum occurring equivalent stress $\sigma_V^{(max)}$ to the permissible stress σ_{zul} .

$$a^{(stat)} = \frac{\sigma_V^{(max)}}{\sigma_{zul}} \quad (4.15)$$

The cyclic degree of utilisation $a^{(dyn)}$ is defined as the ratio of the stress amplitude $\sigma_V^{(a)}$ to the fatigue strength σ_A

$$a^{(dyn)} = \frac{\sigma_V^{(a)}}{\sigma_A} \quad (4.16)$$

The Mises stress is used as a flow criterion for the static load factor. The use of the Mises stress for plastics corresponds to a conservative approach. There are modified versions of the Mises stress criterion in order to take into account different yield limits for tensile and compressive stress. However, they are not implemented in Abaqus. These modified criteria include the influence of the yield point ratio m_Y . Figure 4.30 shows the conical failure criterion and the Mises criterion in dimensionless stress space. Under compressive loads, the flow of the material occurs at significantly higher stresses. More detailed information about these criterion can be found in [6] (p248-253).

$$\sigma_V = \frac{1}{2m_Y} \left[(m_Y - 1)(\sigma_1 + \sigma_2 + \sigma_3) - \frac{1 + m_Y}{\sqrt{2}} \sqrt{(\sigma_1 - \sigma_2)^2 + (\sigma_2 - \sigma_3)^2 + (\sigma_3 - \sigma_1)^2} \right] \quad (4.17)$$

where σ_1 is the maximum principal stress, σ_2 is the middle principal stress and σ_3 is the minimum principal stress.

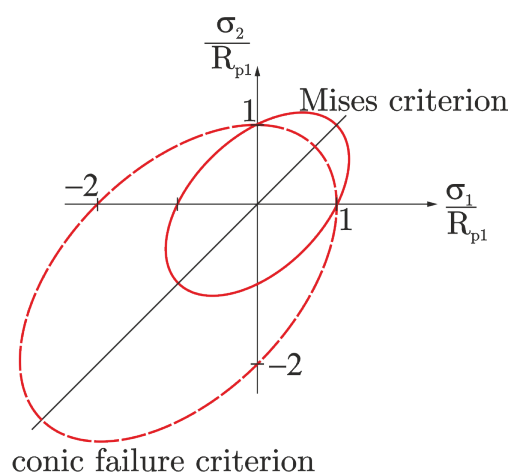


Figure 4.30: Mises criterion compared to the conic failure criterion in the stress space

4.6 Simulation results

As indicated in Figure 4.28, the failure line is shifted towards the compressive yield zone. Since all main principal stresses are negative, the Mises equivalent stress criterion provides values that are too conservative in the design. Nevertheless, the Mises equivalent stress criterion is used. However, the pressure yield point is to be used to determine the permissible stress. In that sense, a shift of the failure curve into the pressure range is taken into account. This makes the simulation results more adequate as explained in more detail in chapter 4.7.7.

Figure 4.31 shows the Mises equivalent stress in the critical area of the cylinder ring affected by the highest amount of stress. As expected, the maximum equivalent stresses occur in a range slightly below the surface.

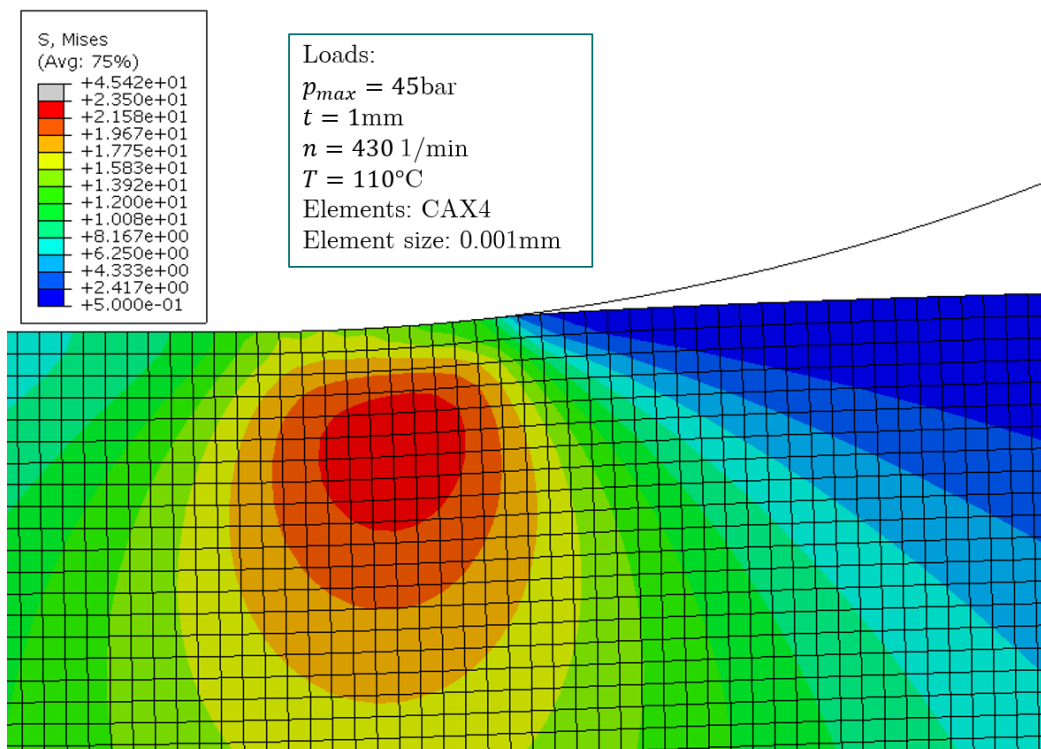


Figure 4.31: Stress field at the critical area of the cylinder ring

The results show that the compressive yield strength is already reached. As a result the cylinder ring material plastically deforms in a small area. Therefore, the degree of utilisation = 1.

To determine the degree of utilisation, it is crucial to determine the stress evolution, as well as the maximum occurring stress. Figure 4.32 shows the evolution of the Mises stress in the critical area. It demonstrates that due to the bending of the cylinder ring around the contact point of the piston a considerable stress concentration occurs. If the cylinder ring is then loaded more heavily from the other side, the stress drops to a low value (time range 0.06 – 0.08s). Towards the end (0.08 – 0.1s) of the cycle, both the pressure in the head end and the pressure in the crank end are at the lower pressure level. This results in a further drop of the Mises stress.

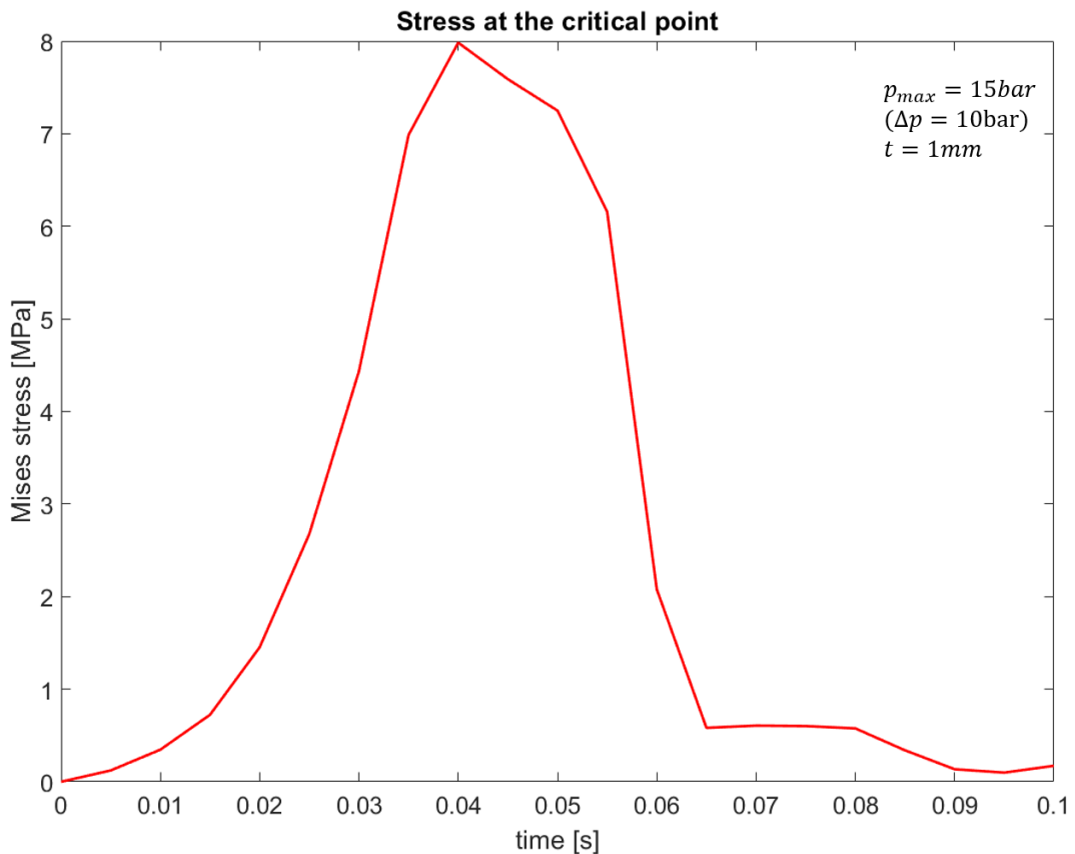


Figure 4.32: Temporal course of the Mises stress

The stress level after the peak remains fairly constant. This range corresponds to the lower level of the stress reached during a load cycle. Consequently, the stress peak is used to determine the average stress and the stress amplitude.

The mean stress corresponds to the average value of the maximum stress and the minimum stress occurring during a load cycle. Strictly speaking, this relationship only applies to a sinusoidal or cosinusoidal evolution of the mechanical stress.

$$\sigma_m = \frac{\sigma_{max} + \sigma_{min}}{2} \quad (4.18)$$

The arithmetic mean value of the stress in the stress amplitude range is used to evaluate the average stress. The stress amplitude is then calculated as follows.

$$\sigma_a = \sigma_{max} - \sigma_m \quad (4.19)$$

Figure 4.33 shows the stress distribution along the component, in axial direction, through the critical point at the time when the highest stress values occur. The sharp stress gradient, is clearly visible. Furthermore, it can be seen that the maximum stress values occur just below the surface, as already shown in Figure 4.29. Furthermore, Figure 4.30 shows that the stress peaks decay very quickly and merge with the undisturbed stress field.

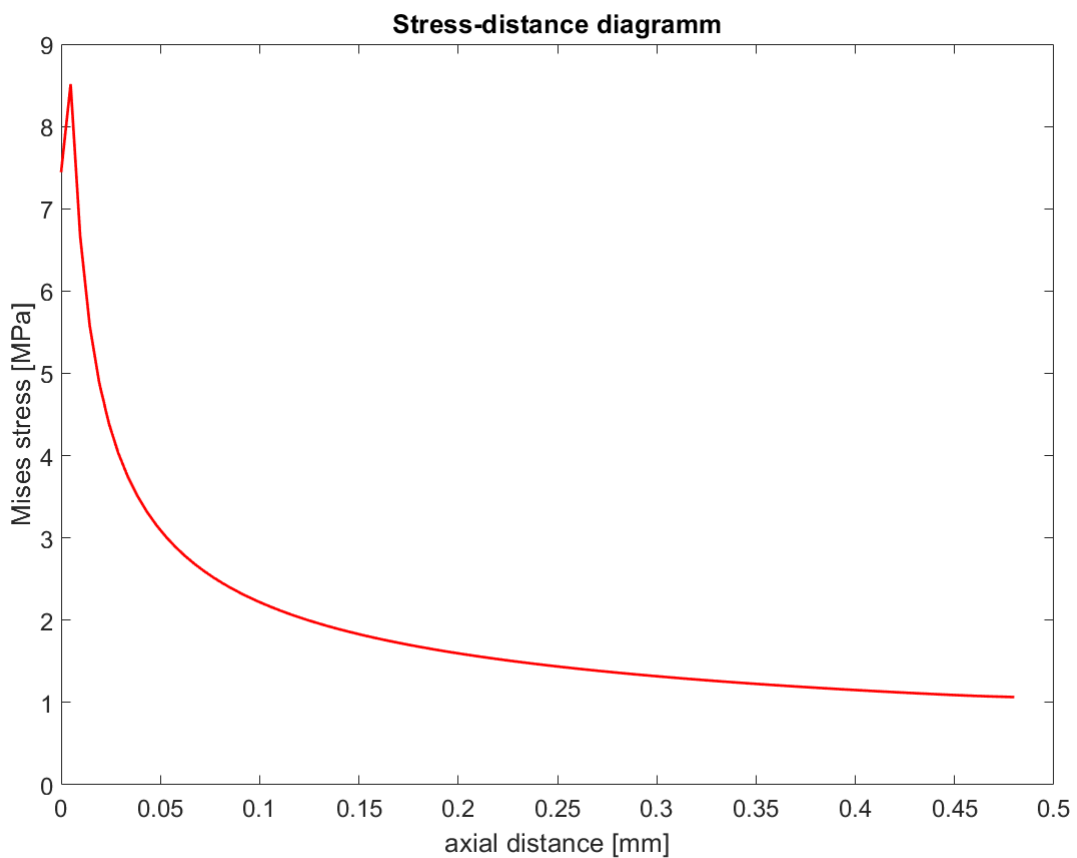


Figure 4.33: Stress versus axial distance according to linear elastic analysis

The shape of the Mises stress versus axial thickness curve is in principle the same for all pressure differences as long as the yield strength is not exceeded. When the yield strength is exceeded the stress curves no longer correspond to the stress curve shown in Figure 4.32 (stress versus time) and Figure 4.33. As a result of the local plastification of the material, stress redistribution occurs.

Table 4.3 shows the influence of the different element types on the maximum stresses occurring during a load cycle.

Table 4.3: Influence of element type to the maximum stresses occur

Element type	Short designation	$\sigma_V^{(max)}$ [MPa]
4-node axisymmetric quadrilateral	CAX4	8.96
4-node axisymmetric quadrilateral, reduced integration	CAX4R	7.98
4-node axisymmetric quadrilateral, incompatible modes	CAX4I	8.95
8-node axisymmetric quadrilateral	CAX8	8.91
8-node axisymmetric quadrilateral, reduced integration	CAX8R	8.89

Elements with quadratic interpolation functions (CAX8, CAX8R) are not recommended for contact problems. The 4-noded bilinear quadrilateral element (CAX4) is used to calculate the utilisation levels. They guarantee a higher safety compared to elements with reduced integration (CAX4R) and a reduction in computational time compared with elements using incompatible modes (CAX4I). For the linear elements with linear interpolation functions and reduced integration (CAX4R), hourglassing occurs. The results are therefore worthless. The following table 4.4 shows the degrees of utilisations for different clearances and pressures between the piston and the cylinder wall.

Table 4.4: Degrees of utilisation for different load levels

clearance [mm]	load level [bar]	$a^{(stat)}$ [-]	$a^{(dyn)}$ [-]
1.0	15.0	0.746	1.000
1.6	12.5	0.764	0.986
2.2	10	0.734	0.983
4.0	7.5	0.765	0.992
5.2	6	0.753	1.000
8.0	4	0.739	0.988

As this table shows, the maximum stresses and the stress amplitudes are almost equal for all cylinder ring protrusions, when the dynamic degree of utilisation is reached.

4.6.1 Utilisation curve

Figure 4.34 illustrates the graphical representation of the results summarized in Table 4.4. It depicts the pressure and the maximum possible clearance at a specific pressure difference. As expected, larger cylinder ring protrusions can be realised at lower pressure levels without putting excessive stress on the material. Protrusions below the red limit curve are permissible (Figure 4.34), whereas they are critical above the red line.

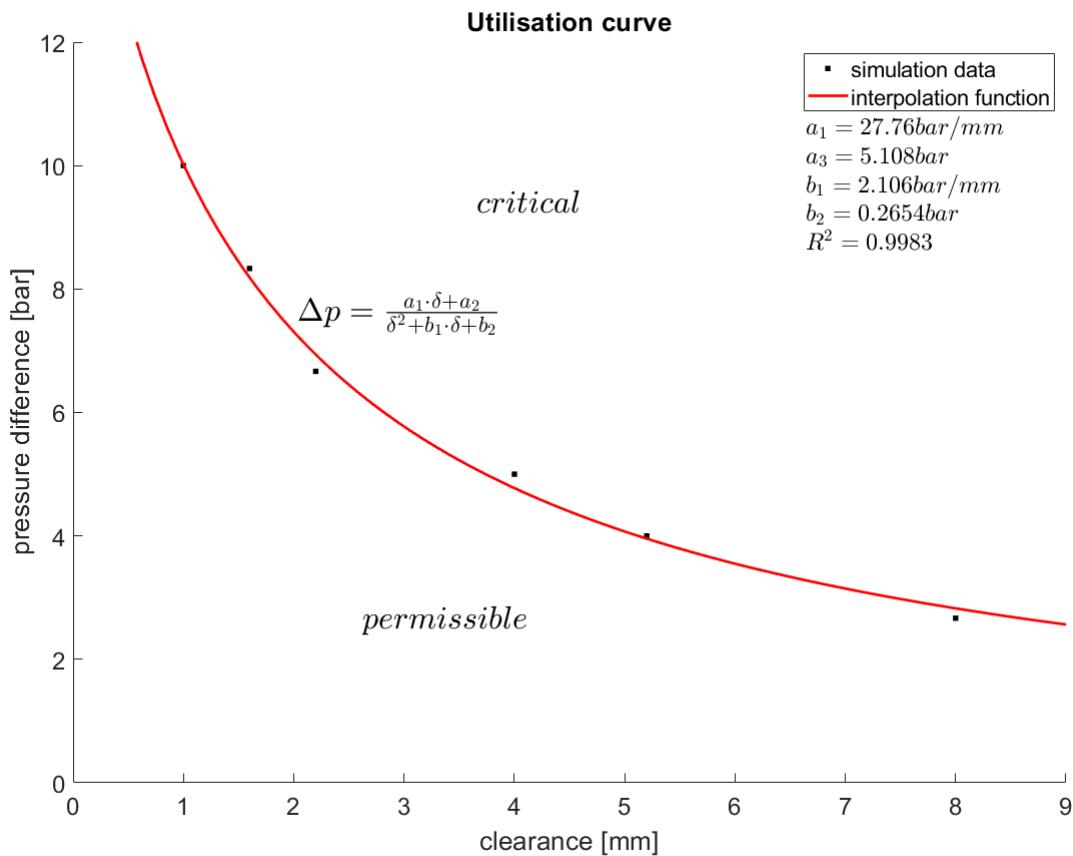


Figure 4.34: Permissible pressure difference as a function of the clearance

The relationship between the pressure and the permissible clearance between the piston and the cylinder wall is non-linear. This is described in detail in chapter 4.7.2. When the clearance between the cylinder wall and the piston increases by a certain amount, the radial thickness of the cylinder ring is increased by the same value. Figure 4.34 shows the simulation results interpolated by a rational function. The simulation results are well approximated by this function (coefficient of correlation $R^2 = 0.9994$). The interpolation approach uses a polynomial numerator of order 1 and a polynomial denominator of order 2. The clearance δ between the cylinder wall and the piston represents the independent variable

$$\Delta p(\delta) = \frac{a_1 \delta + a_2}{\delta^2 + b_1 \delta + b_2} \quad (4.20)$$

where a_1 , a_2 , b_1 and b_2 are the coefficients of the rational function.

By swapping the axes, the clearance between cylinder wall and piston is expressed as a function of the pressure difference. A suitable interpolation function follows from the data points of the utilisation curve. The interpolation curve is determined with the curve fitting tool from Matlab R2020b.

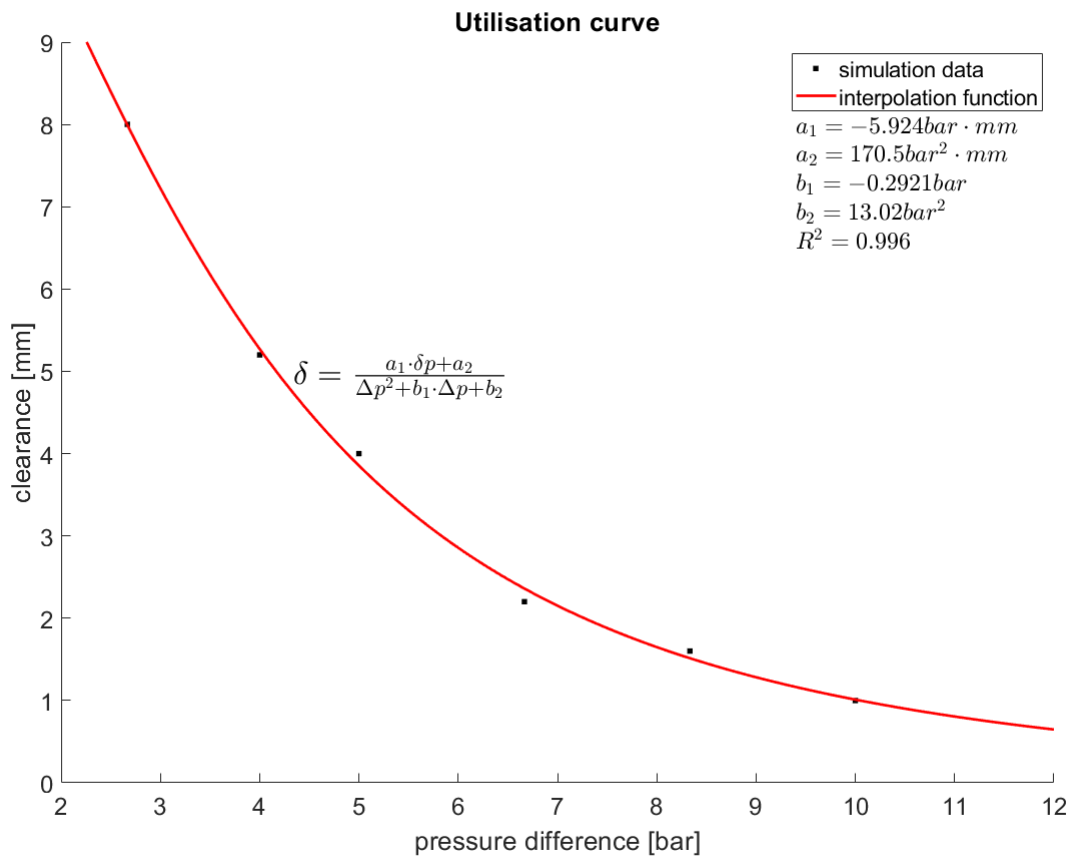


Figure 4.35: Permissible clearance as a function of the pressure difference

Figure 4.35 shows the simulation results interpolated with a rational function. The interpolation approach uses a polynomial numerator of order 1 and a polynomial denominator of order 2. The pressure difference Δp represents the independent variable.

$$\delta(\Delta p) = \frac{a_1 \Delta p + a_2}{\Delta p^2 + b_1 \Delta p + b_2} \quad (4.21)$$

where a_1 , a_2 , b_1 and b_2 are the coefficients of the rational function. As shown in figures 4.34 and 4.35, the clearance between the cylinder wall and the piston increases safely, especially with smaller pressure differences.

4.6.2 Consideration of plasticity for the highest load level

As mentioned in chapter 4.6, plastic deformation occurs in the cylinder ring above a certain load level. Due to the local plastification of the material and hardening effects, a stress redistribution occurs, which reduces the occurring stresses.

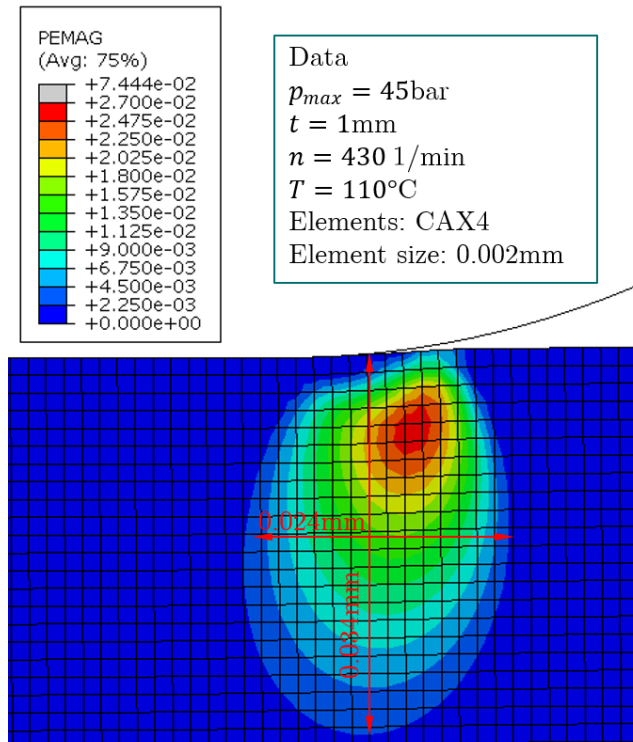


Figure 4.36: Size of the plastic zone at the highest load level after one load cycle

Figure 4.36 displays the plastic zone inside the cylinder ring. The plastic zone is supported by the surrounding elastic material (supporting effect). With a cylinder ring protrusion of 1mm, plastic deformation occurs for maximum pressure peaks of 21bar (14bar pressure difference), when the compressive yield strength of the material used is reached at a cylinder ring temperature of 110°C .

A detailed investigation of the influence of the plastic zone with regard to the damage evaluation would go beyond the scope of this Master thesis.

It should be checked if plasticity has a damaging effect on the material. This can be done using an approximation frequently used in linear-elastic fracture mechanics.

4.6.3 Fracture mechanics

Fracture mechanics deals with the question of whether or not a crack is able to grow, and for which crack lengths the crack growth becomes unstable. In fracture mechanics, the loading of structural components is not described with the mechanical stress, but with the stress intensity. In linear elastic fracture mechanics it is assumed that the stress at the crack tip goes towards infinity, and thus, the comparison with an allowable stress does not make sense. The allowable limit described by the fracture toughness K_{IC} , marks for which value of the stress intensity the crack becomes unstable. Whether the crack has the potential for growth or not, follows from a comparison of the stress intensity ΔK and the threshold value of the stress intensity ΔK_{th} . If the cyclic stress intensity is less than the threshold value, no macro crack growth occurs. The cyclic stress intensity ΔK is therefore

$$\Delta K = Y \Delta \sigma \sqrt{\pi a} \leq \Delta K_{th} \tag{4.22}$$

where Y is a geometry correction factor, $\Delta \sigma$ is 2x the amplitude of the nominal stress and a is the length of the crack, whereas ΔK_{th} is the threshold value of the cyclic stress intensity. Since no material parameters are available for the fracture toughness of the used material, the corresponding values result from a literature research. The fact that the material is filled with additives makes the search for usable and accurate values more difficult.

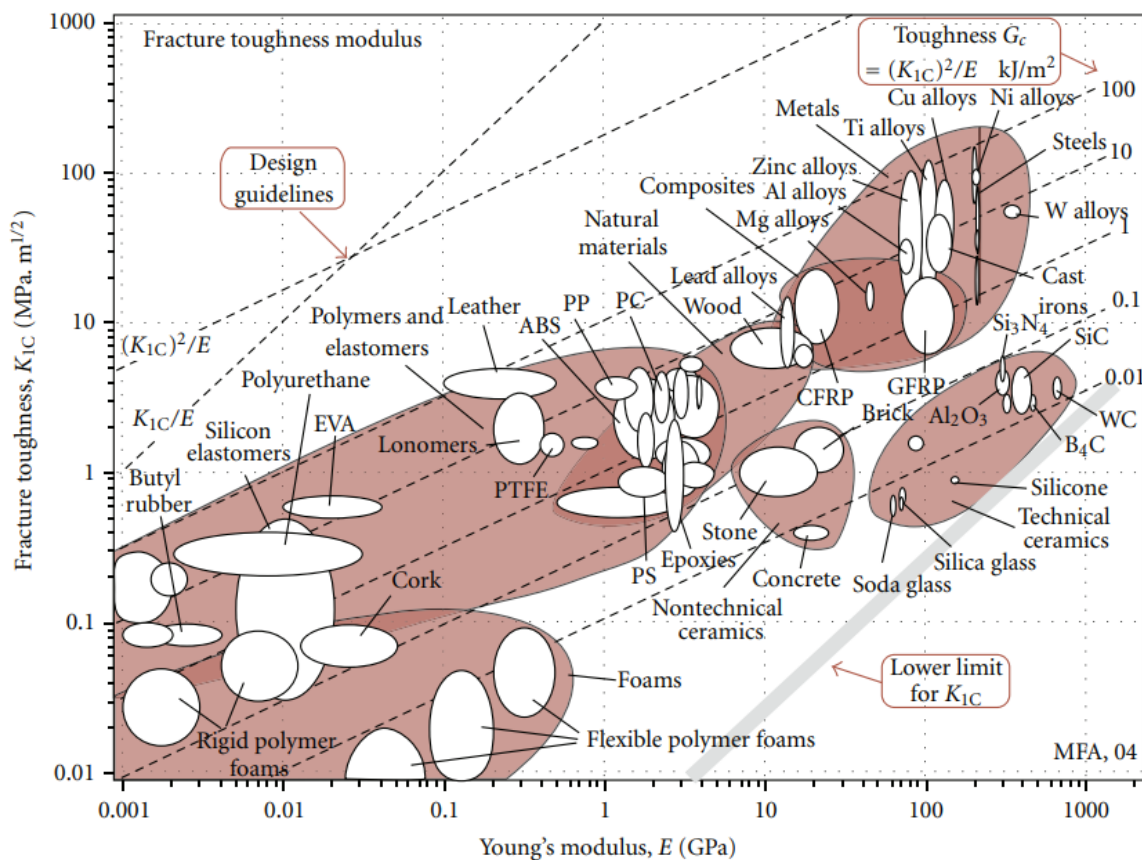


Figure 4.37: Ashby diagramm-fracture toughness versus Young's modulus [8]

According to Figure 4.37, the used cylinder ring material shows a fracture toughness of approximately $1.3 \text{ MPa}\sqrt{\text{m}}$. The cyclic stress intensity threshold is estimated using a polymer with similar fracture toughness. The amorphous polymer PMMA for example shows a fracture toughness of $1.15 \text{ MPa}\sqrt{\text{m}}$. The threshold value of the stress intensity for this material is $0.2 \text{ MPa}\sqrt{\text{m}}$ [15]. To consider the influence of the additive content and the influence of the temperature and to allow for the minimum safety, the threshold value for the material used is estimated to be $0.05 \text{ MPa}\sqrt{\text{m}}$. From the definition (4.22) of the cyclic stress intensity, the critical crack length follows as.

$$a_{crit} \leq \frac{1}{\pi} \left(\frac{\Delta K_{th}}{Y \Delta \sigma} \right)^2 \quad (4.23)$$

For the calculation of the critical crack length at which macro cracks start to grow, the amplitude of the nominal stress is required. For an oscillation width of the nominal stress of approx. 1.50 MPa , a critical crack length of 0.2721 mm results. This already corresponds to a relatively long crack in relation to the width of the cylinder ring. Due to the dependence of the geometry factor on the width of the cylinder ring, the critical crack length requires iterative determination.

In the first iteration step, the geometry factor is initially set to $Y = 1$. Equation (4.22) is then used to calculate the critical crack length. In the second iteration step, the critical crack length is set in relation to the axial thickness of the ring. Depending on this ratio, the geometry factor is determined which depends on the crack location and the aspect ratio and can be obtained from a tabulated list. Then equation (4.24) is used to calculate the crack length again. This iteration process is performed until the crack length no longer changes.

Cylinder rings are engineered not to fail during operation. Thus, any (micro) cracks remain below the threshold of (macro) crack growth. However, microcracks are induced in the material. Investigating the behaviour of these microcracks in the material exceeds the scope of this Master thesis. Therefore, the initiation and behaviour of microcracks is not discussed here.

4.7 Discussion

4.7.1 Cylinder ring protrusion

Figure 4.35 shows the possibility to increase the clearance between the cylinder wall and the piston for smaller pressure differences. A possible increase in cylinder ring protrusion has to remain within reasonable limits. It is important to note that a possible cylinder ring protrusion of more than a certain limit is not useful, even if it is possible, because then other problems may occur. Piston machines, such as piston compressors, are systems that cause vibrations. In addition to imbalance forces due to the rotating components (crankshaft), mass forces also occur due to the components moving in translation (piston). In addition, gas forces occur that change depending on the piston position. All these forces acting on the piston lead to a vibration excitation of individual components of the reciprocating engine or of the entire system. Excessive cylinder ring protrusions may increase this vibration excitation. For a valid statement about the maximum possible cylinder ring protrusion, dynamic considerations have to be taken into account. However, this is not dealt with in this Master thesis. At the maximum pressure level, the load factor is already reached and plastic deformations occur in the cylinder ring. The size of the plastically deformed area is small. Thus, increasing the protrusion is not advisable.

4.7.2 Plausibility of the interpolation function

The evolution of the simulation data for the maximum possible cylinder ring protrusion (Figure 4.34 and 4.35) is well described by a rational function. Analytical considerations are used to test the plausibility of this progression. Assuming linear-elastic material behaviour and a given cylinder ring protrusion, the stress increases linearly with an increase of the pressure level. At given pressure by contrast, the stress increases quadratically with the cylinder ring protrusion. In analogy to the analytical solutions for a cantilever beam loaded by a constant line load or a circular plate loaded by a constant area load. In addition to the bending stresses of the cylinder ring, compressive stresses also appear. If they are superimposed to the bending stress, a rational function follows.

4.7.3 Single acting compressors

The FEM model is also applicable to single-acting compressors. For this, the pressure on the crankshaft side must be set to atmospheric pressure. In contrast to the double-acting compressor, slightly different stress values occur with the single-acting compressor. For the same pressure difference, the maximum stresses are larger, but the stress amplitudes are smaller. Simulations show that it is not the dynamic utilisation level that is reached first, but the static utilisation level. Since there is no counter-pressure, the influence of the cylinder ring protrusion is significantly greater. The results are therefore not transferable. However, the procedure for determining the maximum possible cylinder ring protrusion with the degree of utilisation and local fatigue curves can be applied in the same way. A separate simulation study is therefore necessary to determine the maximum possible protrusion of the ring. Nevertheless, all principal stresses are still negative.

4.7.4 Consideration of the temperature distribution

For even more reliable predictions of the behaviour of the maximum possible cylinder ring protrusion, knowledge of the temperature field inside the cylinder ring would be necessary. To this end knowledge of the heat convection coefficients between the cylinder ring and the working medium is essential. The temperatures of the working medium, as well as the heat convection coefficient, which is strongly influenced by the strongly turbulent flow, require determination with the help of suitable flow simulations. The friction between the cylinder wall and the cylinder ring as well as the heat transfer via the cooled cylinder wall or the piston also need to be taken into account because the temperature has a significant influence on the yield strength of the material. As the temperature increases the yield strength of the material decreases. An inhomogeneous temperature field in the material thus leads to additional stresses. These additional stresses add to the stresses due to the external loads. The maximum temperatures will occur in the most critical area of the cylinder ring. According to equation (2.71), the internal heat source is equal to the scalar product of the stress tensor and the strain rate tensor. Due to the higher temperatures in the critical area, the material tries to expand but is constrained by the surrounding colder material. This induces additional stresses and may cause premature yielding and damage being induced in the material.

4.7.5 Fracture mechanics approach for synthetic fatigue curves

In this master thesis the fatigue strength curves are determined using conservative approximations. The practical determination of fatigue strength curves proves to be time-consuming and expensive, as many tests have to be carried out. According to the corresponding guideline, at least three tests are required for each stress amplitude level at constant mean stress. In addition, the tests need to be carried out at several stress amplitudes, and the mean stress is not to be changed during a series of tests. To determine the mean stress sensitivity, the tests have to be repeated at different mean stresses. Further tests are necessary to determine other influencing factors such as the influence of fillers or other additives. Determining the fatigue strength curves is much more efficient with the help of a fracture mechanics concept.

The fracture mechanics concept allows determining synthetic fatigue strength curves based on results of fracture mechanics tests (see Figure 4.38). In addition to a significant reduction of the testing time (factor 10 to 20) and a reduction of the number of test specimens, this leads to a lower scatter of the results [15]. The fracture mechanics concept essentially only requires the threshold value of the cyclic stress intensity ΔK_{th} and the material-specific parameters A and m_P to describe the range of stable crack growth (Paris law).

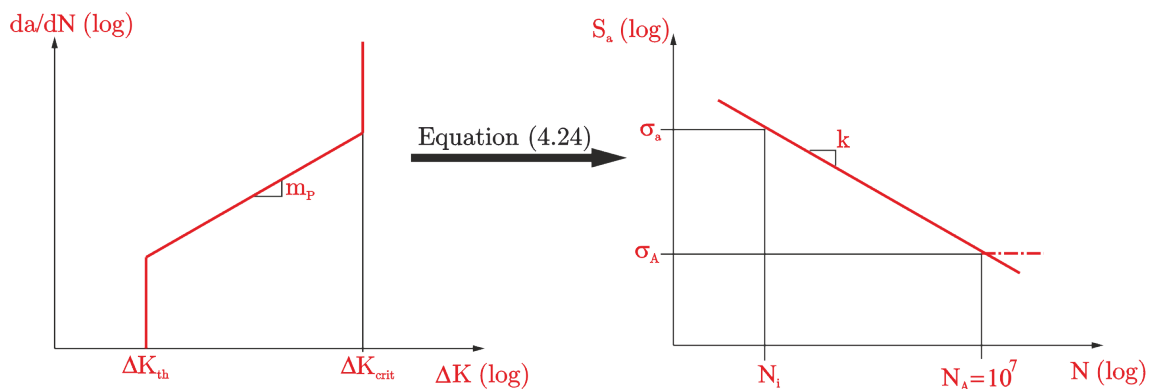


Figure 4.38: Fracture mechanics approach for synthetic fatigue curves using equation (4.26)

According to the fracture mechanics concept, the fatigue strength is proportional to the threshold value of the cyclic stress intensity and the initial length of a defect [15].

$$\sigma_A \propto \frac{\Delta K_{th}}{\sqrt{a}} \quad (4.24)$$

The finite life fatigue strength is proportional to the cyclic stress intensity and the initial length of a defect [15].

$$\sigma_a \propto \frac{\Delta K}{\sqrt{a}} \quad (4.25)$$

If the corresponding material data is available, it is recommended to use the fracture mechanics concept for fatigue life modelling. The fracture mechanics concept also allows the calculation of the service life taking into account the crack initiation phase. For this purpose, two additional material parameters have to be determined.

4.7.6 Mises criterion for polymers

Strictly speaking, the equivalent stress criterion according to Mises is applicable only to materials with the same tensile and compressive strengths. Mises' yield hypothesis, like Tresca's hypothesis assumes isotropy of the material at the onset of yielding and equal yield limits for uniaxial tension as well as compression [13]. Thus, this criterion is strictly speaking not applicable to polymer materials. Nevertheless, it is frequently used in practice for simulations in the field of polymer technology. For materials with different tensile and compressive strengths, failure criteria based on two material properties are recommended. Typical failure criteria based on two material parameters are for example the conical failure criterion and the paraboloid failure criterion.

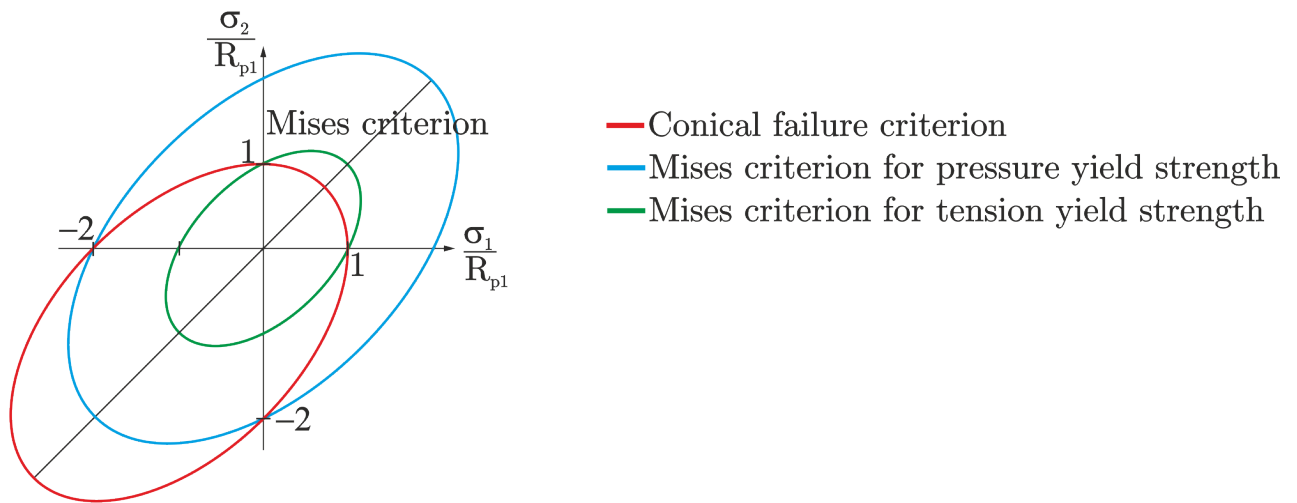


Figure 4.39: Comparison between the conic failure criterion and the Mises criterion

Figure 4.39 shows the conical failure criterion as well as the Mises criterion for the tensile yield strength (green ellipse) and the compressive yield limit (blue ellipse) in dimensionless stress space. Using the compressive yield strength as the material limit gives less conservative results than using the tensile yield strength for negative principal stresses. However, the results are still more conservative than the results of the conical failure criterion. This is advantageous in application because it provides sufficient reserves against the onset of plastic deformation. It illustrates the modified version of the Mises flow criterion used in this master thesis. This criterion is more conservative than the conical failure criterion in quadrants 2-4. Only in the first quadrant the conical failure criterion is more conservative. If one or more principal stresses are positive the criterion for failure is:

$$\sigma_V = \sqrt{\frac{1}{2} [(\sigma_1 - \sigma_2)^2 + (\sigma_2 - \sigma_3)^2 + (\sigma_3 - \sigma_1)^2]} \leq R_{p,tensile} \quad (4.26)$$

If all principal stresses are negative the criterion for failure is:

$$\sigma_V = \sqrt{\frac{1}{2} [(\sigma_1 - \sigma_2)^2 + (\sigma_2 - \sigma_3)^2 + (\sigma_3 - \sigma_1)^2]} \leq R_{p,compression} \quad (4.27)$$

Chapter 5

Conclusion and Outlook

5.1 Conclusion

The central intention of this master thesis is to determine the maximum possible cylinder ring protrusion for double-acting piston compressors. Furthermore, the influence of the material as well as the geometry on the deformation behavior of the cylinder ring shall be investigated.

Within the scope of this master thesis, it was first investigated how well the simulation results of different 3D geometries agree with the results of an axisymmetric model. The shape and the stresses occurring at the critical point were used as criteria. Using material data, the material parameters of a viscoelastic material model were fitted. Furthermore, a parameter study is performed to determine which effects the geometry, the loading as well as the material itself have on the creep behavior of the cylinder ring material. The final part of this master thesis deals with the operationally stable design of the cylinder ring protrusions.

The results of the parameter study are in line with expectations, but have now been quantified. An increase in the cylinder ring protrusion leads to a strong increase in the creep strain in the critical region as a result of the higher stresses. Higher pressures lead to higher stresses and consequently to higher strains. Temperature also has a significant influence on the creep behaviour of the cylinder ring material. This is due to the strong dependence of the material parameters on temperature. The geometry of the cylinder rings, i.e. the inner and outer diameter as well as the axial thickness established at HOERBIGER Wien GmbH ensure almost equal maximum stresses for all sizes of cylinder rings.

The results of the parameter study not only show the influence of the various parameters on the creep behaviour of the material. To investigate what leads to the failure of the cylinder ring, the creep strains were examined as part of the parameter study. The results show that the creep strains that occur are not critical. Thus, the fatigue due to the cyclic loading of the material is relevant for the failure. Consequently, the viscoelastic material model is not necessary and a linear elastic material model is sufficient for further simulations.

The most important result of this Master thesis is the operationally stable limit of cylinder rings protrusions for the double-acting piston compressors. In principle, this dimensioning strategy presented here is also suitable for the dimensioning of cylinder rings of other piston machines, such as single-acting compressors.

The results show that the cylinder ring protrusion can be increased as long as the pressure differences are not too large. For pressure differences in the range of 5 bar, the cylinder ring protrusion can be significantly increased without reaching the limit of the static or dynamic degree of utilisation. It should be noted, however, that an increase in the cylinder ring protrusion must remain within reasonable limits. In the range of highest pressure differences (30bar), plastic deformation occurs locally. However, the plastically deformed areas are very small. Here it is not recommended to use an operational strength criterion. If local plastic deformations occur, microcrack growth should be investigated using a fracture mechanics criterion.

Even for higher pressure differences, failure of the cylinder rings only occurs in exceptional cases. In principle, it is therefore possible to increase the cylinder ring protrusion even at higher pressure differences. Exact quantification requires fatigue strength data from material

tests. The fatigue strength is estimated in this work with conservative approximation formulas. A comparison with Table 4.4 shows that the maximum static degree of utilisation is far from being reached, whereas the dynamic utilisation level is fully exploited.

5.2 Outlook

A fracture mechanics consideration concerning the formation of micro cracks in the plastically deformed zone (for higher pressure differences) can be conducted. In this way, it will be clarified to what extent the plastic zones are critical.

In a further scientific work, the formation of the plastic zones at higher load levels will be investigated in more detail. This can be done on the basis of the calibrated viscoelastic-viscoplastic material model attached in the appendix of this Master thesis. The attached model is a three-network (TNF) model. This is the most advanced material model for describing the behaviour of polymers over the entire deformation range up to fracture. With the help of this model, the formation and possible growth or stabilisation behaviour of the plastically deformed zone can be investigated as a result of further research work.

List of Figures

1.1	Piston compressor [10]	5
2.1	Free-body-diagram of an infinite mass element	8
2.2	Kinematics of a mass element in cylindrical coordinates	10
2.3	Kinematics in cylindrical coordinates for shear deformation	11
2.4	Linear elastic material behaviour	13
2.5	Viscous material behaviour	14
2.6	Ideal plastic material behaviour	15
2.7	Ideal viscoelastic material behaviour	16
2.8	Principle of the relaxation test	17
2.9	Effects of periodic loads to stress and strain for viscoelastic materials	22
2.10	Complex Young's modulus in gaussian plane	22
2.11	Hysteresis curve in the stress-strain diagram	23
2.12	Heat Flux through through the surface of a solid	24
2.13	Principle of calibrating the Prony series parameters	27
2.14	Principle of calibrating temperature shifting parameters	29
2.15	Three network model	30
3.1	Sketch of the cylinder ring model	33
3.2	Parametrisation of the FE-model used in the Python script	33
3.3	FE-model in Abaqus CAE	34
3.4	Submodel in Abaqus CAE	35
3.5	Load signal for crank end, Calculated data and Fourier approximation	37
3.6	Load signal for head end, Calculated data and Fourier approximation	38
3.7	Heat flux balance for the cylinder ring	39
4.1	Cylinder rings from HOERBIGER Wien GmbH. [10]	42
4.2	Stress field in the cylinder ring	43
4.3	Stress field in the cylinder ring of the critical area	44
4.4	Stress field in the uncut 3D cylinder ring	45
4.5	Stress field in the cut 3D cylinder ring at the gap	46
4.6	Stress field in the cut 3D cylinder ring at the marked cross section	46
4.7	Results of the convergence study	48
4.8	Application of Saint Venant's principle	49
4.9	Results of material parameter calibration	50
4.10	Evaluation of the viscoelastic material model for uniaxial load. a) Evolution of the normalised relaxation modulus, b) Evolution of the normalised creep compliance	52

4.11	Location of element 684	53
4.12	Normal components of the creep strain	53
4.13	Influence of the ring protrusion t on the creep behaviour	55
4.14	Influence of the temperature on creep behaviour	56
4.15	Influence of the load rate on the creep behaviour	57
4.16	Adiabatic heating through hysteresis losses	58
4.17	Influence of the applied load on the creep behaviour	59
4.18	Influence of the dimensions of the cylinder rings on the creep behaviour	60
4.19	Influence of the dimensions with actual cylinder ring protrusions	61
4.20	Influence of the selected material model	62
4.21	Simulation of an uniaxial cyclic creep test	63
4.22	Influence of the form of the pressure signal to fluctuation of the base curve	64
4.23	Fatigue strength curve for a polymer material	67
4.24	Influence of the mean stress to permissible stress amplitude	68
4.25	Synthetically generated material fatigue curve for three stress ratios	69
4.26	Determination of the component fatigue curve by using local concepts	70
4.27	Synthetically generated component fatigue curve at the most critical area	71
4.28	Influence of the local stress gradient on component fatigue curve	72
4.29	Determination of the stress gradient	73
4.30	Influence of the yield ration to failure criterion	74
4.31	Stress field at the critical area of the cylinder ring	75
4.32	Temporal course of the Mises stress	76
4.33	Stress versus distance according to linear elastic analysis	77
4.34	Pressure difference as a function of the clearance	79
4.35	Clearance as a function of the pressure difference	80
4.36	Size of the plastic zone at the highest load level after one load cycle	81
4.37	Ashby diagramm [8]	82
4.38	Fracture mechancis approach	86
4.39	Comparison between the conic failure criterion and the Mises criterion	87

Bibliography

- [1] ABAQUS/Standard User's Manual
- [2] Altenbach H., Tushtev K., A NEW STATIC FAILURE CRITERION FOR ISOTROPIC POLYMERS, Mechanics of Materials, 2001
- [3] Altenbach H., Kontinuumsmechanik, Springer Vieweg.
- [4] Bergstroem J., Mechanics of solid polymers, 2015, Elsevier Inc.
- [5] Chinh N.T., Hoang T., LIFE-TIME PREDICTION FOR POLYMER MATERIALS, Vietnam Journal of Science and Technology, 2021
- [6] Ehrenstein G.W., Polymer Werkstoffe Struktur-Eigenschaften, Anwendung, 2011, Hanser,
- [7] Eichseder W. Fatigue analysis by local stress concept based on finite element results. Computers & Structures, 2002
- [8] Findik F., A Case Study on the Selection of Materials for Eye Lenses, 2011
- [9] Guedes R. M., Analysis of a delayed fracture criterion for lifetime prediction of viscoelastic polymer materials, Mech Time-Depend Mater, 2012
- [10] Kaufmann A., Wear of dry-running piston rod sealing rings: modelling and experiments, Leoben 2019
- [11] Kunz J., Ein Plädoyer für die dehnungsbezogene Auslegung, 2011
- [12] Li S., The Maximum Stress Failure, Criterion and the Maximum Strain Failure Criterion: Their Unification and Rationalization, Journal of Composites Science, 2020
- [13] Mang H. A., Hofstetter G., Festigkeitslehre, 5. Auflage, Springer Verlag
- [14] Mascarenhas W.N., Design criteria and safety factors for plastic components design, Materials and Design, 2003

Bibliography

- [15] Pinter G., Bruchmechanik der Kunst- und Verbundwerkstoffe, Leoben 2021
- [16] Song M.S., Hu G.X., Hu L.J., Prediction of Long-Term Mechanical behaviour and Lifetime of Polymeric Materials, Polymer Testing, 1998
- [17] Spathis G., Kontou E., Creep failure time prediction of polymers and polymer composites, Composites Science and Technology, 2012
- [18] Taylor D. Wang G, the validation of some methods of notched fatigue analysis, Fatigue Fract Engng Mater Struct, 2000
- [19] Stommel M., Stojek M. , Korte W., FEM zur Berechnung von Kunststoff- und Elastomerbauteilen, 2018, Hanser
- [20] Zhang W., Comparison of Relaxation Modulus converted from Frequency- and Time -Dependent Viscoelastic functions through Numerical methods, 2018

Appendix

Python- and Matlab scripts

The Python script with which the finite element model is built is given in the appendix. The documentation of the individual steps is in German. Furthermore, additional Matlab scripts are listed in the appendix. A Matlab script contains, for example, the calculation of the coefficients of the Fourier series for the mathematical description of the temporal course of the pressure. Furthermore, the Matlab script for generating the synthetic fatigue curve is listed.

In the appendix a calibrated visco-plastic material model is given, which was explained at the beginning of the theoretical part. However, this material model was not used in the simulations because the implementation of the coefficients in Abaqus CAE proved to be extremely difficult, as the (PRF model) is a combination of viscoelastic behaviour and plasticity is not valid in Abaqus.

Python script for FEA model

```
#-----  
# Masterarbeit–Ruetz  
# (c) Marcel Ruetz BSc.  
#-----  
  
from abaqus import *  
from abaqusConstants import *  
import regionToolset  
import section  
import regionToolset  
import displayGroupMdbToolset as dgm  
import displayGroupOdbToolset as dgo  
  
#-----  
# Importieren der Messdatensaetze  
#-----  
  
# Importieren von Pythonmodul numpy  
import numpy as np  
  
# Einlesen der txt Datei der Daten des Crank Ends sowie des Head Ends  
dataCE = np.loadtxt('dataCE.txt', skiprows = 2)  
dataHE = np.loadtxt('dataHE.txt', skiprows = 2)  
  
# Auslesen des maximalen Druckes aus der txt Tabelle  
p_maxCE = np.max(dataCE[:,1])  
p_maxHE = np.max(dataHE[:,1])  
  
# Auswaehlen der Zeit aus der txt Tabelle  
t_CE = dataCE[:,0]  
t_HE = dataHE[:,0]  
  
# Auslesen der Druেকে aus der txt Tabelle  
p_CE = dataCE[:,1]/p_maxCE  
p_HE = dataHE[:,1]/p_maxHE  
  
# Umrechnung der Druেকে von bar in MPa  
p_maxCE = p_maxCE/10.0  
#p_maxCE = 1.5  
p_maxHE = p_maxHE/10.0  
#p_maxHE = 1.5  
  
#-----
```

```
# Berechnung der Koeffizienten der Fourier Reihe
#-----

# Importierung der mit MATLAB berechneten Fourier Koeffizienten
data = np.loadtxt('fourierCoefficients.txt', skiprows = 1)
c = data[:,]
a0, a1, a2, a3, a4, a5, a6, a7, a8 = c[0], c[1], c[3], c[5], c[7], c[9],
c[11], c[13], c[15]
b1, b2, b3, b4, b5, b6, b7, b8 = c[2], c[4], c[6], c[8], c[10], c[12],
c[14], c[16]
omega = c[17]

data = np.loadtxt('fourierCoefficients_HE.txt', skiprows = 1)
c = data[:,]
a02, a12, a22, a32, a42, a52, a62, a72, a82 = c[0], c[1], c[3], c[5],
c[7], c[9], c[11], c[13], c[15]
b12, b22, b32, b42, b52, b62, b72, b82 = c[2], c[4], c[6], c[8], c[10],
c[12], c[14], c[16]
omega2 = c[17]

#-----
# Erstellen des Modells
#-----

sealModel = mdb.models['Model-1']

#-----
# Erstellen der Komponenten
#-----

# Importieren des Zeichenmoduls und des Stueckmoduls
import sketch
import part

#-----
#Parameterisierung der Abmessungen und Vernetzungen des Modells
#-----

# Hier ist die Parameterisierung des FEM-Modells zu finden
ra = 200. #mm
b = 14. #mm
b0 = 0. #mm
spiel = 1.0#mm
ri = 200.-18.-spiel+1.0 #mm
meshsize_grob = 0.5 #mm
meshsize_fein = 0.05 #mm
meshsize_sub = 0.001 #mm
```

```

# Definition der Elementtypen
elementtype1 = CAX4
elementtype2 = CAX3
# Parameterisierung des feiner vernetzen Bereichs
b_finer_mesh = 7.0-spiel+1.0 #mm
# Parameterisierung der Abmessungen des Submodells
r_sub = ra-spiel
# Bem. Die axiale Dicke des Submodells sollte nicht veraendert werden,
# da diese so dick zu waehlen ist, das die auftretende Spannungs-
# konzentration keinen Einfluss auf das Ergebnis hat (Saint-Venant)

#-----
# Erstellen der Dichtung
#-----

# Erstellen der Skizzenumgebung
s = sealModel.ConstrainedSketch(name='__profile__',
    sheetSize=200.0)
# Estellen der Geometrie
g, v, d, c = s.geometry, s.vertices, s.dimensions, s.constraints
# Einstellung des Skizzenstyles
s.sketchOptions.setValues(viewStyle=AXISYM)
# Darstellen des Modells
s.setPrimaryObject(option=STANDALONE)
s.ConstructionLine(point1=(0.0, -100.0), point2=(0.0, 100.0))
s.FixedConstraint(entity=g[2])
# Darstellen des Dichtungsringes
s.rectangle(point1=(ra, b), point2=(ri, b0))
# Estellen des Dichtungsringes als Part
sealPart = sealModel.Part(name='Dichtung',
    dimensionality=AXISYMMETRIC, type=DEFORMABLE_BODY)
sealPart = sealModel.parts['Dichtung']
# Darstellung
sealPart.BaseShell(sketch=s)
s.unsetPrimaryObject()
del sealModel.sketches['__profile__']

# Partitionierung des Dichtungsringes
rDatum = ra-spiel
rPart = ra-spiel -0.099 #mm
partParam = (rPart-ri)/(ra-ri) #-

# Erzeugung des Datumpunktes
sealPart.DatumPointByCoordinate(coords=(rDatum, b, 0.0))
f, e, d1 = sealPart.faces, sealPart.edges, sealPart.datums
t = sealPart.MakeSketchTransform(sketchPlane=f[0],
    sketchPlaneSide=SIDE1, origin=(

```

```

        rPart, rPart, 0.0))
s1 = sealModel.ConstrainedSketch(name='__profile__',
    sheetSize=84.85, gridSpacing=2.12, transform=t)
g, v, d, c = s1.geometry, s1.vertices, s1.dimensions, s1.constraints
s1.setPrimaryObject(option=SUPERIMPOSE)
sealPart.projectReferencesOntoSketch(sketch=s1, filter=COPLANAR_EDGES)
s1.unsetPrimaryObject()
del sealModel.sketches['__profile__']
# Auswaehlen der Flaechе (Linie)
e = sealPart.edges
pickedEdges = e.getSequenceFromMask(mask=('[#1_]', ), )
# Partitionierung der Flaechе
sealPart.PartitionEdgeByParam(edges=pickedEdges, parameter=partParam)
# Erzeugung des Datumpunktes auf der zweiten Seite
sealPart.DatumPointByCoordinate(coords=(rDatum, b0, 0.0))
f, e, d1 = sealPart.faces, sealPart.edges, sealPart.datums
t = sealPart.MakeSketchTransform(sketchPlane=f[0], sketchPlaneSide=SIDE1,
    origin=(rPart, rPart, 0.0))
s1 = mdb.models['Model-1'].ConstrainedSketch(name='__profile__',
    sheetSize=84.85, gridSpacing=2.12, transform=t)
g, v, d, c = s1.geometry, s1.vertices, s1.dimensions, s1.constraints
s1.setPrimaryObject(option=SUPERIMPOSE)
sealPart.projectReferencesOntoSketch(sketch=s1, filter=COPLANAR_EDGES)
s1.unsetPrimaryObject()
del sealModel.sketches['__profile__']
# Auswaehlen der Flaechе (Linie)
p = mdb.models['Model-1'].parts['Dichtung']
pickedEdges = e.getSequenceFromMask(mask=('[#4_]', ), )
p.PartitionEdgeByParam(edges=pickedEdges, parameter=1.0-partParam)
# Partitionierung der Flaechе zur Definition eines Bereichs zum
#feineren Vernetzen
p = sealModel.parts['Dichtung']
f = p.faces
pickedRegions = f.getSequenceFromMask(mask=('[#1_]', ), )
f, e, d = p.faces, p.edges, p.datums
t = p.MakeSketchTransform(sketchPlane=f[0], sketchPlaneSide=SIDE1,
    origin=(191.0, 7.0, 0.0))
s = sealModel.ConstrainedSketch(name='__profile__',
    sheetSize=400.97, gridSpacing=10.02, transform=t)
g, v, d1, c = s.geometry, s.vertices, s.dimensions, s.constraints
s.setPrimaryObject(option=SUPERIMPOSE)
p.projectReferencesOntoSketch(sketch=s, filter=COPLANAR_EDGES)
s.rectangle(point1=(9.0, 7.0), point2=(b_finer_mesh, 5.0))
pickedFaces = f.getSequenceFromMask(mask=('[#1_]', ), )
e1, d2 = p.edges, p.datums
p.PartitionFaceBySketch(faces=pickedFaces, sketch=s)
s.unsetPrimaryObject()

```

```

#
# Darstellung des Kolbens
#

# Schleife fuer Standout Abmessungen
standout = 2.0
# Abmessungen des Kolbens
r1 = ra-spiel #mm
r2 = ri-standout #mm
l1 = b+standout #mm
l2 = b #mm
l3 = -spiel#mm
l4 = -standout#mm
r = 0.1 #mm

# Erstellen der Skizze fuer den Kolben
s1 = sealModel.ConstrainedSketch(name='__profile__',
    sheetSize=200.0)
g, v, d, c = s1.geometry, s1.vertices, s1.dimensions, s1.constraints
# Definition des Skizzentyps fuer die Skizze
s1.sketchOptions.setValues(viewStyle=AXISYM)
s1.setPrimaryObject(option=STANDALONE)
s1.ConstructionLine(point1=(0.0, -100.0), point2=(0.0, 100.0))
s1.FixedConstraint(entity=g[2])

# Definition der Geometrie des Kolbens (Linienzug)
s1.Line(point1=(r1, l1), point2=(r1, l2))
s1.VerticalConstraint(entity=g[3], addUndoState=False)
s1.Line(point1=(r1, l2), point2=(r2, l2))
s1.HorizontalConstraint(entity=g[4], addUndoState=False)
s1.PerpendicularConstraint(entity1=g[3], entity2=g[4], addUndoState=False)
# Implementierung der Radien am Kolben
s1.FilletByRadius(radius=r, curve1=g[4], nearPoint1=(r-spiel,
    b), curve2=g[3], nearPoint2=(r,
    b+spiel))
# Erstellen des Kolbens als axialsymmetrisches, starres Model
p = sealModel.Part(name='Kolben', dimensionality=AXISYMMETRIC,
    type=DISCRETE_RIGID_SURFACE)
piston = sealModel.parts['Kolben']
p.BaseWire(sketch=s1)
s1.unsetPrimaryObject()
del mdb.models['Model-1'].sketches['__profile__']

# Definition des Referenzpunktes fuer den starren Koerper
p = sealModel.parts['Kolben']
v, e, d, n = piston.vertices, piston.edges, piston.datums, piston.nodes
piston.ReferencePoint(point=v[0])

```

```

# Definition der Master – und Slave Surface fuer das Model
p = sealModel.parts['Dichtung']
s = p.edges
side1Edges = s.getSequenceFromMask(mask=('[#38_]', ), )
p.Surface(side1Edges=side1Edges, name='Slave_Model')
p = sealModel.parts['Kolben']
p = sealModel.parts['Kolben']
s = p.edges
side1Edges = s.getSequenceFromMask(mask=('[#4_]', ), )
side2Edges = s.getSequenceFromMask(mask=('[#2_]', ), )
p.Surface(side1Edges=side1Edges, side2Edges=side2Edges,
name='Master_Model')

```

```

#
# Definition der Materialparameter fuer linear elastisches
# Materialverhalten
#
# Bem. S\"amtliche Informationen bez\"uglich Materialdaten und Parameter si
#
# Implementierung der Section des Modells
#

```

```

# Importieren des Section Moduls
import section
# Erstellen einer Section to assign zur Dichtung
sealModel.HomogeneousSolidSection(name='Dichtung_Section',
material='PTFE', thickness=None)
# Assign the seal to the section
p = sealModel.parts['Dichtung']
f = p.faces
faces = f.getSequenceFromMask(mask=('[#3_]', ), )
region = p.Set(faces=faces, name='Set-2')
p.SectionAssignment(region=region, sectionName='Dichtung_Section',
offset=0.0,
offsetType=MIDDLE_SURFACE, offsetField='',
thicknessAssignment=FROM_SECTION)

```

```

#
# Implementierung des Assemblies des Dichtringes
#

```

```

# Importierung des assembly Moduls
import assembly
# Erstellen des Assemblys der Dichtung
sealInstance = sealModel.rootAssembly
sealInstance.DatumCsysByThreePoints(coordSysType=CYLINDRICAL, origin=(0.0,

```



```

0.0, 0.0),
    point1=(1.0, 0.0, 0.0), point2=(0.0, 0.0, -1.0))
sealInstance.Instance(name='Dichtung-1', part=sealPart, dependent=ON)
# Erstellen des Assemblys des Kolbens
pistonInstance = sealModel.rootAssembly
pistonInstance.Instance(name='Kolben-1', part=piston, dependent=ON)

#-----
# Erstellen der Steps
#-----

# Importieren des Step Moduls
import step
# Erstellen eines Steps (static general fuer die erste Lastaufbringung)
sealModel.ViscoStep(name='Step', previous='Initial',
    timePeriod=60.0, maxNumInc=100000000, initialInc=0.005,
    minInc=0.00015, maxInc=0.005, nlgeom=ON, cetol=1.0)

#-----
# Implementierung und Definition der Field Output requests
#-----

# Umbenennen des Field Outputs
sealModel.fieldOutputRequests.changeKey(fromName='F-Output-1',
    toName='Ausgegebene_Feldgroessen')
# Definition der auszugebenen Feldgroessen
sealModel.fieldOutputRequests['Ausgegebene_Feldgroessen'].setValues(
    variables=('S', 'E', 'U', 'RF'))
# Definition der auszugebenden Feldgroessen in Step 2
sealModel.fieldOutputRequests['Ausgegebene_Feldgroessen'].setValuesInStep(
    stepName='Step', variables=('S', 'E', 'CE', 'CEMAG', 'U', 'RF'))

#-----
# Erstellen der History Output
#-----

sealModel.fieldOutputRequests['Ausgegebene_Feldgroessen'].setValuesInStep(
    stepName='Step', frequency=1)

#-----
# Erstellen der Interaktionsbeziehungen
#-----

# Import des Connector Modul
import connectorbehaviour

# Erstellen der Kontaktbedingung
sealModel.ContactProperty('Kontakt')

```

```

# Normalkontakt zwischen zwei trockenen Oberflaechen
sealModel.interactionProperties['Kontakt'].Normalbehaviour(
    pressureOverclosure=HARD, allowSeparation=ON,
    constraintEnforcementMethod=DEFAULT)

a = sealModel.rootAssembly
# Auswaehlen der Master Surface
region1=a.instances['Kolben-1'].surfaces['Master_Model']
# Auswaehlen der Slave Surface
region2=a.instances['Dichtung-1'].surfaces['Slave_Model']
# Definition des Oberflaechen-Oberflaechen-Kontakts
sealModel.SurfaceToSurfaceContactStd(name='Model_Interaction',
    createStepName='Initial', master=region1, slave=region2,
    sliding=FINITE, thickness=ON, interactionProperty='Kontakt',
    adjustMethod=NONE, initialClearance=OMIT, datumAxis=None,
    clearanceRegion=None)

#-----
# Aufbringen der Lasten sowie der Randbedingungen
#-----

# Importieren des Lastmoduls
import load
# Importieren des Amplitudenmoduls

# Benennung des Laststeps
session.viewports['Viewport:1'].assemblyDisplay.setValues(
    step='Step')
sealLoad = sealModel.rootAssembly

# Definition des zeitlichen Verlaufes der Last (CE)
sealModel.PeriodicAmplitude(name='pt_dataCE', timeSpan=TOTAL,
    frequency=omega, start=0.0, a_0=a0, data=((a1, b1), (a2,
    b2), (a3, b3), (a4, b4), (a5, b5), (
    a6, b6), (a7, b7), (a8, b8)))

# Definition des zeitlichen Verlaufes der Last (HE)
sealModel.PeriodicAmplitude(name='pt_dataHE', timeSpan=TOTAL,
    frequency=omega2, start=0.0, a_0=a02, data=((a12, b12), (a22,
    b22), (a32, b32), (a42, b42), (a52, b52), (
    a62, b62), (a72, b72), (a82, b82)))

# Definition des Druckes auf die Crank End Seite
a = sealModel.rootAssembly
s1 = a.instances['Dichtung-1'].edges
side1Edges1 = s1.getSequenceFromMask(mask=('[#180]', ), )

```

```

region = a.Surface(side1Edges=side1Edges1, name='Surf-8')
sealModel.Pressure(name='Load_CE', createStepName='Step',
    region=region, distributionType=UNIFORM, field='',
    magnitude=p_maxCE,
    amplitude='pt_dataCE')

# Definition des Druckes auf den Innenradius
a = sealModel.rootAssembly
s1 = a.instances['Dichtung-1'].edges
side1Edges1 = s1.getSequenceFromMask(mask=('[#40_]', ), )
region = a.Surface(side1Edges=side1Edges1, name='Surf-9')
sealModel.Pressure(name='Druck_Boden', createStepName='Step',
    region=region, distributionType=UNIFORM, field='',
    magnitude=p_maxCE,
    amplitude='pt_dataCE')

# Definition des Druckes auf die Head End Seite
a = sealModel.rootAssembly
s1 = a.instances['Dichtung-1'].edges
side1Edges1 = s1.getSequenceFromMask(mask=('[#8_]', ), )
region = a.Surface(side1Edges=side1Edges1, name='Surf-10')
sealModel.Pressure(name='Load_HE', createStepName='Step',
    region=region, distributionType=UNIFORM, field='',
    magnitude=p_maxHE,
    amplitude='pt_dataHE')

# Definition der Zylinderwand
a = mdb.models['Model-1'].rootAssembly
e1 = a.instances['Dichtung-1'].edges
edges1 = e1.getSequenceFromMask(mask=('[#204_]', ), )
region = a.Set(edges=edges1, name='Set-3')
sealModel.XsymmBC(name='Zylinderwand', createStepName='Initial',
    region=region, localCsys=None)

# Definition der Lagerung des Kolbens
a = mdb.models['Model-1'].rootAssembly
r1 = a.instances['Kolben-1'].referencePoints
refPoints1=(r1[2], )
region = a.Set(referencePoints=refPoints1, name='Set-2')
sealModel.EncastreBC(name='Lagerung_Kolben', createStepName='Initial',
    region=region, localCsys=None)

#
# Einstellen der Vernetzungsparameter

```

#

*# Importierung des Vernetzungsmoduls***import** mesh*# Definition der Groesse der Vernetzung*sealPart.seedPart(size=meshsize_grob, deviationFactor=0.1,
minSizeFactor=0.1)*# Definition der Elementtypen*

elemType1 = mesh.ElemType(elemCode=elementtype1, elemLibrary=STANDARD)

elemType2 = mesh.ElemType(elemCode=elementtype2, elemLibrary=STANDARD)

Definieren der zu vernetzenden Flaechen

sealFace = sealPart.faces

faces = sealFace.getSequenceFromMask(mask=['[#1□]',],)

Waehlen der Flaechen

pickedRegions =(faces,)

*# Definition der gewaehlten Region*sealPart.setElementType(regions=pickedRegions, elemTypes=(elemType1,
elemType2))*# Erzeugung des Netzes*

sealPart.generateMesh()

Definiton des Bereichs des feineren Mesh

p = sealModel.parts['Dichtung']

f = p.faces

pickedRegions = f.getSequenceFromMask(mask=['[#3□]',],)

p.deleteMesh(regions=pickedRegions)

e = p.edges

pickedEdges = e.getSequenceFromMask(mask=['[#1f□]',],)

p.seedEdgeBySize(edges=pickedEdges, size=meshsize_fein,

deviationFactor=0.1,

minSizeFactor=0.1, constraint=FINER)

p.generateMesh()

*# Vernetzung des Kolbens**# Definition der Groesse der Vernetzung*

piston.seedPart(size=0.002, deviationFactor=0.1, minSizeFactor=0.1)

Erzeugung des Netzes

piston.generateMesh()

Feinere Vernetzung der Radien

e = piston.edges

pickedRegions = e.getSequenceFromMask(mask=['[#2□]',],)

piston.deleteMesh(regions=pickedRegions)

pickedEdges = e.getSequenceFromMask(mask=['[#2□]',],)

piston.seedEdgeBySize(edges=pickedEdges, size=0.002, deviationFactor=0.1,

```

        minSizeFactor=0.1, constraint=FINER)
# Erzeugung des Netzes
piston.generateMesh()

#-----
# Durchfuehrung der Simulationen
#-----

# Importierung des Job Moduls
import job

# Simulation der mech. Problemstellung
a = sealModel.rootAssembly
a.regenerate()
mdb.Job(name='analysis', model='Model-1',
        description='Berechnung', type=ANALYSIS, atTime=None,
        waitMinutes=0, waitHours=0, queue=None, memory=90,
        memoryUnits=PERCENTAGE, getMemoryFromAnalysis=True,
        explicitPrecision=SINGLE, nodalOutputPrecision=SINGLE,
        echoPrint=OFF, modelPrint=OFF, contactPrint=OFF,
        historyPrint=OFF, userSubroutine='', scratch='',
        resultsFormat=ODB, multiprocessingMode=DEFAULT,
        numCpus=1, numGPUs=0)

#-----
# Erstellen des Submodels
#-----

# Kopieren des urspruenglichen Models
mdb.Model(name='Submodel', objectToCopy=sealModel)
# Umbenennen des Models
sealSubmodel = mdb.models['Submodel']
# Definition des Dichtungsringes
sealSubmodel.parts['Dichtung']
# Zugreifen auf die Ergebnisse der globalen Simulation
sealSubmodel.setValues(globalJob='analysis')
# Definition von Flaechen
p = sealSubmodel.parts['Dichtung']
f = p.faces
# Definition des Gebietes des Submodels
f1, e1, d2 = p.faces, p.edges, p.datums
t = p.MakeSketchTransform(sketchPlane=f1[0], sketchPlaneSide=SIDE1,
        origin=(r_sub, 13.0, 0.0))
s = sealSubmodel.ConstrainedSketch(name='__profile__', sheetSize=22.8,
        gridSpacing=0.57, transform=t)
g, v, d, c = s.geometry, s.vertices, s.dimensions, s.constraints
s.setPrimaryObject(option=SUPERIMPOSE)

```

```

p.projectReferencesOntoSketch(sketch=s, filter=COPLANAR_EDGES)
s.rectangle(point1=(-0.01, 0.5), point2=(0.1, 0.01))
s.CoincidentConstraint(entity1=v[11], entity2=g[6], addUndoState=False)
s.EqualDistanceConstraint(entity1=v[4], entity2=v[0], midpoint=v[11],
    addUndoState=False)
pickedFaces = f.getSequenceFromMask(mask=('[#1_]', ), )
e, d1 = p.edges, p.datums
p.PartitionFaceBySketch(faces=pickedFaces, sketch=s)
s.unsetPrimaryObject()
# Loeschen des 2 Datum Punktes
del p.features['Datum_2pt-2']
# Loeschen der Bereiche ohne besonderes Interesse
p.RemoveFaces(faceList = f[0:1]+f[2:3], deleteCells=False)
a = sealSubmodel.rootAssembly
e1 = a.instances['Dichtung-1'].edges
edges1 = e1.getSequenceFromMask(mask=('[#3_]', ), )
region = a.Set(edges=edges1, name='Set-3')

#-----
# Neudefinition der Interactions
#-----

# Loeschen der nicht benoetigten Interaction
del sealSubmodel.interactions['Model_Interaction']

# Auswaehlen des Models
a = sealSubmodel.rootAssembly
# Auswaehlen des Kolbens
s1 = a.instances['Kolben-1'].edges
# Waehlen der Kanten fuer Interaction am Submodel
side1Edges1 = s1.getSequenceFromMask(mask=('[#4_]', ), )
side2Edges1 = s1.getSequenceFromMask(mask=('[#2_]', ), )
# Definition der Mastersurface
a.Surface(side1Edges=side1Edges1, side2Edges=side2Edges1,
    name='MasterSurf_Sub')
# Auswahlen des Kolbens
s1 = a.instances['Dichtung-1'].edges
# Definition der Kanten fuer die Slave Surface
side1Edges1 = s1.getSequenceFromMask(mask=('[#6_]', ), )
# Definition der Slace Surface
a.Surface(side1Edges=side1Edges1, name='SlaveSurf_Sub')
# Auswaehlen der Master Surface
region1=a-surfaces['MasterSurf_Sub']
# Auswaehlen der Slave Surface
region2=a-surfaces['SlaveSurf_Sub']
# Definition des Oberflaechen-Oberflaechen-Kontakts

```

```

sealSubmodel.SurfaceToSurfaceContactStd(name='Interaction_Submodel',
    createStepName='Initial', master=region1, slave=region2,
    sliding=FINITE, thickness=ON, interactionProperty='Kontakt',
    adjustMethod=NONE, initialClearance=OMIT, datumAxis=None,
    clearanceRegion=None)

#-----
# Neudefinition der Boundary Conditions
#-----

# Loeschen von Lasten des Globalmodels
del sealSubmodel.loads['Druck_Boden']
del sealSubmodel.loads['Load_CE']
del sealSubmodel.loads['Load_HE']
# Loeschen von Randbedingungen des Globalmodels
del sealSubmodel.boundaryConditions['Zylinderwand']
# Definition der Last fuer das Submodel
a = sealSubmodel.rootAssembly
s1 = a.instances['Dichtung-1'].edges
side1Edges1 = s1.getSequenceFromMask(mask=('[#2_]', ), )
region = a.Surface(side1Edges=side1Edges1, name='Surf-6')
sealSubmodel.Pressure(name='Load_HE', createStepName='Step',
    region=region, distributionType=UNIFORM, field='',
    magnitude=p_maxHE,
    amplitude='pt_dataHE')
# Definition des Bereichs fuer die Randbedingungen
a = sealSubmodel.rootAssembly
e1 = a.instances['Dichtung-1'].edges
edges1 = e1.getSequenceFromMask(mask=('[#19_]', ), )
region = a.Set(edges=edges1, name='Set-4')
# Definition der Randbedingungen fuer das Submodel
sealSubmodel.SubmodelBC(name='RB', createStepName='Step',
    region=region, globalStep='1', globalIncrement=0, timeScale=OFF,
    dof=(1, 2), globalDrivingRegion='',
    absoluteExteriorTolerance=None, exteriorTolerance=0.05)

#-----
# Vernetzen des Submodels
#-----

p = sealSubmodel.parts['Dichtung']
f = p.faces
pickedRegions = f.getSequenceFromMask(mask=('[#1_]', ), )
p.deleteMesh(regions=pickedRegions)
e = p.edges
pickedEdges = e.getSequenceFromMask(mask=('[#6_]', ), )
p.deleteSeeds(regions=pickedEdges)

```

```
# Definition des Netzes fuer das Submodel
p.seedPart(size=meshsize_sub, deviationFactor=0.1, minSizeFactor=0.1)
# Generieren des Netzes fuer das Submodel
p.generateMesh()

p = sealSubmodel.parts['Kolben']
e = p.edges
pickedRegions = e.getSequenceFromMask(mask=['#2_'], )
p.deleteMesh(regions=pickedRegions)
pickedEdges = e.getSequenceFromMask(mask=['#2_'], )
p.seedEdgeBySize(edges=pickedEdges, size=0.002, deviationFactor=0.1,
                minSizeFactor=0.1, constraint=FINER)
p.generateMesh()

#-----
# Job fuer Submodel
#-----

# Erstellen des Jobs fuer das Submodel
a = sealModel.rootAssembly
a.regenerate()
mdb.Job(name='Submodel-analysis', model='Submodel',
        description='Berechnung', type=ANALYSIS, atTime=None,
        waitMinutes=0, waitHours=0, queue=None, memory=90,
        memoryUnits=PERCENTAGE, getMemoryFromAnalysis=True,
        explicitPrecision=SINGLE, nodalOutputPrecision=SINGLE,
        echoPrint=OFF,
        modelPrint=OFF, contactPrint=OFF, historyPrint=OFF,
        userSubroutine='',
        scratch='', resultsFormat=ODB, multiprocessingMode=DEFAULT,
        numCpus=1, numGPUs=0)
```


Ploten des t–p–Profils und der Fourier Approximation

```
%%%%%%%%%%%%%%%%%%%%%%%%%%%%%%%%%%%%%%%%%%%%%%%%%%%%%%%%%%%%%%%%%%%%%%%%%
```

```
figure;  
plot(time, pressure, 'r')  
grid minor;  
hold on;  
plot(f, time, pressure)  
xlabel('time [s]');  
ylabel('pressure [%]');  
title('normalised time–pressure–dependence');  
legend('Fourier series n=8', 'Measurement data');
```

```
%%%%%%%%%%%%%%%%%%%%%%%%%%%%%%%%%%%%%%%%%%%%%%%%%%%%%%%%%%%%%%%%%%%%%%%%%
```

Abspeichern der berechneten Fourier Koeffizienten als txt.file

```
%%%%%%%%%%%%%%%%%%%%%%%%%%%%%%%%%%%%%%%%%%%%%%%%%%%%%%%%%%%%%%%%%%%%%%%%%
```

```
fileID = fopen('fourierCoefficients.txt', 'w');  
fprintf(fileID, '%12s\r\n', 'fourierCoefficients60');  
fprintf(fileID, '%12.8f\r\n', coeffVal);  
fclose(fileID);
```


Synthetische Woehlerkurve

```
%%%%%%%%%%%%%%%%%%%%%%%%%%%%%%%%%%%%%%%%%%%%%%%%%%%%%%%%%%%%%%%%%%%%%%%%%
```

```
figure;
```

```
N = linspace(100, 107, 10000);
```

```
N_A = 107; %dW
```

```
k = log(N_A)/log(Rpz/SW)
```

```
S_a = S_G*(N_A./N).(1/k);
```

```
S_aw = S_W*(N_A./N).(1/k);
```

```
S_az = S_gz*(N_A./N).(1/k);
```

```
loglog(N, S_aw, 'b', N, S_a, 'r', N, S_az, 'k')
```

```
xlabel('log(N)')
```

```
ylabel('log(\sigma_a)')
```

```
grid on
```

```
title('Synthetic material fatigue curve')
```

```
ylim([1, 10])
```

```
legend('R=-1', 'R=-\infty', 'R=0')
```

```
%%%%%%%%%%%%%%%%%%%%%%%%%%%%%%%%%%%%%%%%%%%%%%%%%%%%%%%%%%%%%%%%%%%%%%%%%
```

Bauteilwoehlerlinie

```
%%%%%%%%%%%%%%%%%%%%%%%%%%%%%%%%%%%%%%%%%%%%%%%%%%%%%%%%%%%%%%%%%%%%%%%%%
```

```
figure;
```

```
s_A = S_G*(1+(1.10-1)*(40.50/(2/16))0.3)
```

```
S_a = s_A.*(N_A./N).(1/k);
```

```
loglog(N, S_a, 'r')
```

```
xlabel('log(N)')
```

```
ylabel('log(\sigma_a)')
```

```
grid on
```

```
title('Synthetic component fatigue curve')
```

```
ylim([1, 15])
```

```
xlim([1, 107])
```



```
% Ploten des Spannungsverlauf und des Gradienten
%%%%%%%%%%%%%%%%%%%%%%%%%%%%%%%%%%%%%%%%%%%%%%%%%%%%%%%%%%%%%%%%%%%%%%%%%

figure;
plot(t, S_Mises, 'r', x, stress, 'b');
xlabel('distance [mm]');
ylabel('Mises stress [MPa]')
title('Determination of the stress gradient')
legend('stress', 'stress gradient')
%%%%%%%%%%%%%%%%%%%%%%%%%%%%%%%%%%%%%%%%%%%%%%%%%%%%%%%%%%%%%%%%%%%%%%%%%
% Berechnung des Bezogenen Spannungsgradient nach Siebel
%%%%%%%%%%%%%%%%%%%%%%%%%%%%%%%%%%%%%%%%%%%%%%%%%%%%%%%%%%%%%%%%%%%%%%%%%

chi = 1/sigma_max*abs(p(1))
```